広島大学学位請求論文

# Monte Carlo Simulation of Atomic Distribution of Guest Atoms Intercalated into Layered $TiS_2$ Crystals

(層状結晶 $TiS_2$ にインターカレーションしたゲスト原子の原子分布のモンテカルロ・シミュレーション)

根岸　彩子

# 目　次

(5) Impurity Scattering by Guest 3d Metals and Their Impurity Band Formation in $M_xTiS_2$ (M= 3d Metals)
H. Negishi, S. Kakita, H. Yamada, S. Negishi, M. Sasaki and M. Inoue
Solid State Communications **112** (1999) 275-279.

(6) A New Type of Bulk Quantum Hall Effect in $Bi_{2-x}Sn_xTe_3$ Crystals
M. Inoue, N. Miyajima, M. Sasaki, H. Negishi, S. Negishi, H. Kadomatsu, and V. A. Kulbachinskii
Physica B: Condensed Matter **284-288** (2000) 1718-1719.

(7) EXAFS and XANES Studies on 3d Transition Metal Intercalation Compounds $M_xTiS_2$
H. Negishi, S. Negishi, M. Sasaki, M. Inoue, and S. Ohara
Molecular Crystals and Liquid Crystals **341** (2000) 63-68.

(8) Possibility of Charge Density Wave Transition in Tellurium Molybdenum Oxide $TeMo_5O_{16}$
H. Negishi, S. Negishi, M. Sasaki, M. Inoue, K. Takase, Y. Kubota, Y. Takano, and K. Sekizawa
Japanese Journal of Applied Physics **39** (2000) (in press).

# 主論文

# Monte Carlo Simulation of Atomic Distribution of Guest Atoms Intercalated into Layered $TiS_2$ Crystals

Saiko Negishi

# Abstract

Monte Carlo simulations of atomic distribution of intercalated guest atoms in the layered 1T-$TiS_2$ have been performed by taking into account attractive or repulsive *pair-interactions* between the neighboring guest atoms in the $a$-axis plane ($V_{a1}$ and $V_{a2}$) and along the $c$-axis of the crystal lattice ($V_{c1}$ and $V_{2c}$); lattice size for computation: $18 \times 18 \times 6$. X-ray diffraction patterns for $Fe_xTiS_2$ are calculated from the atomic distributions obtained using these four pair-interactions, in qualitative agreement with the experimental data of the $2a \times 2a \times 2c$ short-range ordered structure for $x = 0.15$, $2\sqrt{3}a \times 2a \times 2c$ superlattice for $x = 0.25$, and $\sqrt{3}a \times \sqrt{3}a \times 2c$ superlattice for $x = 0.333$ with fractional site occupancy. From the calculated atomic distributions, we have evaluated the number of neighboring guest atoms, the formation of clusters, and percolation cluster, as well as its dimension, all of which are responsible for the dynamical relaxation behaviors of the thermoremanent magnetization observed in the spin- and cluster-glass phases of $Fe_xTiS_2$. In particular, one- and two-dimensional percolation clusters are formed by the third nearest neighbors in the $a$-axis plane for $x = 0.15$ and 0.25, respectively, and a two-dimensional one by the second nearest neighbors for $x = 0.333$, which corresponds to the magnetic phase diagram [spin-glass ($x = 0.15$) and cluster-glass ($x = 0.25$ and 0.333)]. Using the present results and EXAFS data, we have further discussed on the change in the local structures near the host sulfur atoms by intercalation of the guest atoms in $Fe_xTiS_2$ and $Co_xTiS_2$.

Similar calculations have been made for another type of intercalation compound of stage-2 $Ag_xTiS_2$ ($x = 0.15$) that shows a phase transition from the ordered $\sqrt{3}a \times \sqrt{3}a \times 2c$ to disordered structure around 250-300 K. The formation of stage-2 structure can be reasonably simulated by additional incorporation of *repulsive* pair-interaction, $V_{c2}$, along the $c$-axis direction, and by taking into account the considerably weak pair-interaction strengths, compared to those of $Fe_xTiS_2$, in satisfactory accord with the observed X-ray patterns. Furthermore, the order-disorder phase transition can be understood by considering the temperature dependence of atomic distributions, the thermal displacements of Ti, S, and Ag atoms, and entropy change due to the phase transition. The essential difference between stage-1 $Fe_xTiS_2$ and stage-2 $Ag_{0.15}TiS_2$ is discussed based on a local lattice deformation produced by intercalation. The size of the guest atom plays a crucial role to the formation of stage-1 or -2 compound; guest atoms with crystal radius larger than 1.0 Å are found to produce preferentially the stage-2 structure in the host $TiS_2$. Such a large deformation may be the origin to exert *repulsive* pair-interaction on the second nearest neighboring sites in the next layers.

# Contents

# Chapter 1

# Introduction

Layered materials have been extensively studied from the scientific and technical interests due to their low dimensional natures in crystal structures and electronic properties, and wide possibility to form new and exotic materials by the insertion of the various guest atoms and/or molecules into their van der Waals gaps between the constituent layers, so-called "*intercalation*", leading to a variety of applications such as a secondary battery, electrochromism, and catalyses. As a host material there are known many layered materials such as graphite, transition metal dichalcogenide $TX_2$, molybdenum oxides, and clays [1-5]. Their physical and chemical properties are modified strongly upon intercalation of guest species. Schematic structures of the intercalation compounds are shown in Fig. 1.1, where the guest atoms are inserted into van der Waals gaps per $n$ host layers along the stacking direction. According to the periodicity of $n$, they are referred to as stage-$n$ intercalation compounds; namely, *stage-1*, *stage-2*, and *stage-3* structures. Such staging phenomena are often observed in various intercalation compounds, suggesting the existence of rather long-range interactions along the stacking direction.

Among others, 1T-$TiS_2$ is a typical example of host material with a simple 1T-$CdI_2$ type layered structure, where Ti atom is surrounded by six S atoms, forming constituent layers in the $a$-axis plane stacked along the $c$-axis by weak van der Waals force with the intralayer lattice spacing $a$ = 3.41 Å and the interlayer spacing $c$ = 5.70 Å [Fig. 1.2(a)], and thus various guest species $G$ can be inserted into the van der Waals layers, forming intercalation compounds $G_xTiS_2$ [Fig. 1.2(b)], where $G$ is typically Ag, alkaline metal $A$ (= Li, Na, K, ...), 3d transition-metal $M$, and organic molecules [2-10]. In particular, extensive studies of $M_xTiS_2$ (= Ti, V, Cr, Mn, Fe, Co, Ni, and Cu) have been performed, whose salient features are summarized as follows: (1) Upon intercalation, the 3d metals $M$ occupy the octahedral sites in the van der Waals layers to form stage-1 intercalation compound, and the intralayer lattice spacing $a$ does not change substantially, while the interlayer spacing $c$ depends strongly on the guest $M$ and its concentration $x$ (large expansion for Mn guests and remarkable contraction for Co and Ni ones) [8,9]. Extended X-ray absorption fine structure (EXAFS) measurements of K-edges of $M$ and Ti atoms [11,12] have confirmed that the interatomic distance between the guest $M$ and S atoms in $M_xTiS_2$, $R$($M$-S), depends strongly on the kind of $M$ but less depends on the concentration $x$, while that between the host Ti and S atoms, $R$(Ti-S), is increased with $x$, meaning the small expansion of the host layers upon intercalation of the guest atoms. (2) Intercalation induces a charge transfer from the guest atom $M$ to the host Ti 3d conduction band, leading to the change in the Fermi energy $E_F$ and the density of states at $E_F$, as found by specific heat measurements [13,14], photoemission spectroscopic studies [15-23], and transport measurements [24-28]. (3) Various magnetic phases are found in these compounds $M_xTiS_2$ ($M$ = V, Cr, Mn, Fe, Co, and Ni), such as paramagnetic (P), ferromagnetic (F), weak ferromagnetic (WF), and antiferromagnetic (AF) phases [29-37]. Among them, the Fe intercalate $Fe_xTiS_2$ shows spin-glass (SG, $0.01 \leq x \leq 0.20$), cluster-glass (CG, $0.20 <$

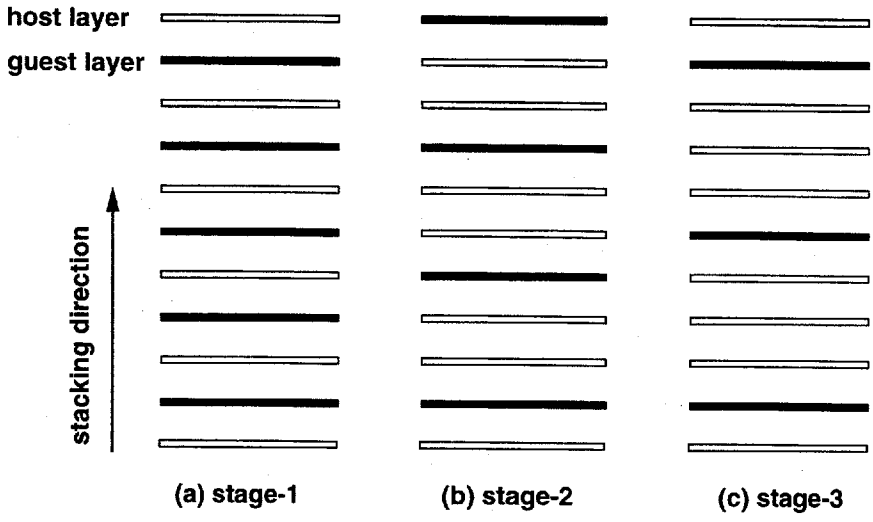


Fig. 1.1 Schematic structures of intercalation compounds with (a) stage-1, (b) stage-2, and (c) stage-3.

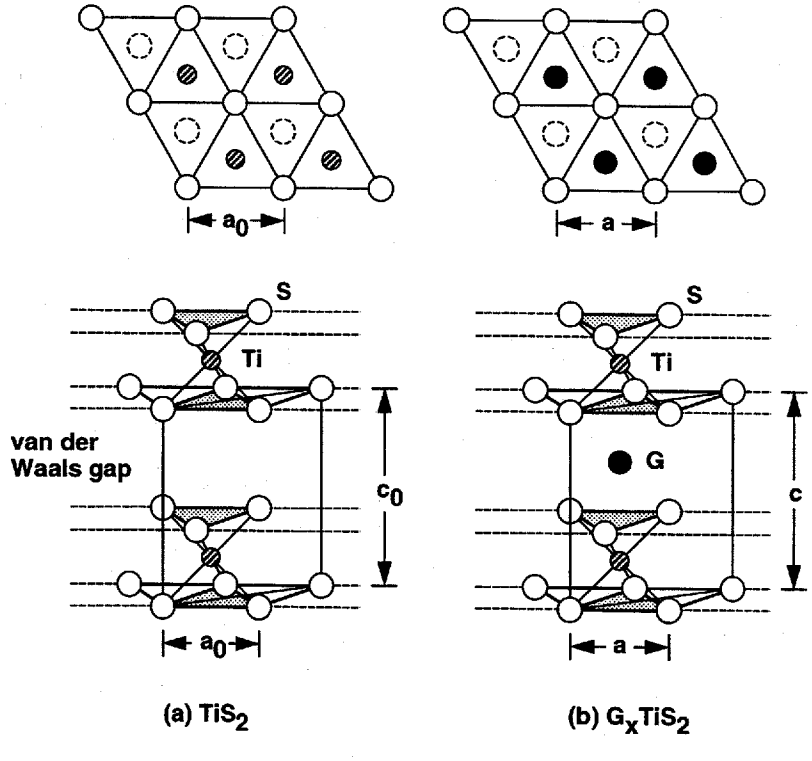


Fig. 1.2 Perspective and top views of the crystal structure of (a) $TiS_2$ and (b) $G_xTiS_2$; the octahedral sites for the guest atoms $G$ are arranged to form 2-dimensional triangular lattice in the $a$-axis plane.

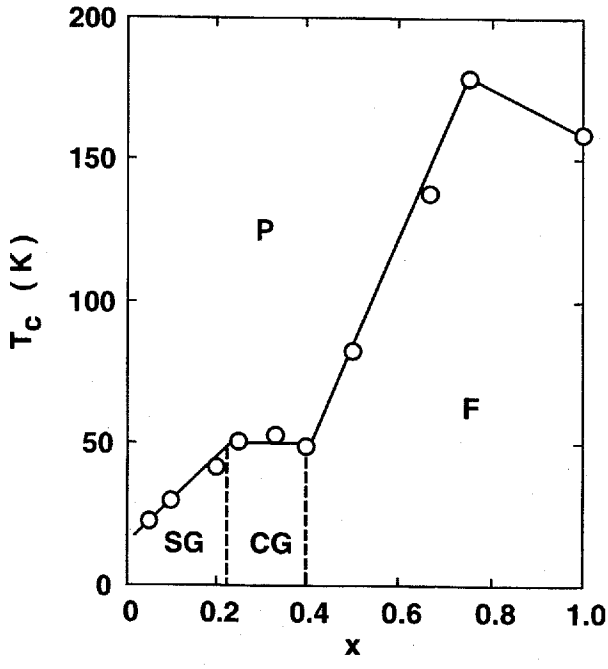


Fig. 1.3 Magnetic phase diagram of $Fe_xTiS_2$; paramagnetic (P), spin glass (SG), cluster glass (CG), and ferromagnetism (F) [33].

$x \leq 0.40$), and ferromagnetic phases (F, $x > 0.40$), as shown in Fig. 1.3 [33-37]. In the SG and CG phases the temperature dependence of ac magnetic susceptibility shows a cusp or peak, which shifts to the lower temperature side when some static magnetic field is superposed, meaning that the observed cusp or peak are characteristic of the freezing effect due to the frustration between spins or clusters, since the superposition of static field suppresses the fluctuation effects between spins. (4) These electronic and magnetic properties of $M_xTiS_2$ are understood primarily in terms of an 'itinerant electron' picture rather than a 'localized' one, as predicted by band calculations using self-consistent APW methods [38-42], and photoemission studies [15-23], which have revealed a strong 'hybridization' among the guest $M$ 3d orbitals and the host Ti 3d and S 3p orbitals. (5) In SG and CG phases of $Fe_xTiS_2$, long-time relaxation phenomena of the thermoremanent magnetization $M_r$ have been measured using an anomalous Hall effect to analyze the observed time decay curves of $M_r$ based on a domain theory [43-46]. As a result, we have found that these materials have very broad equilibrium relaxation spectra, suggesting an important role of the distribution of the guest Fe atoms, or the formation of their clusters.

Furthermore, the structural studies [47] by X-ray diffraction for single crystals of $Fe_xTiS_2$ have shown the short-range order of $2a \times 2a \times 2c$ for $x = 0.15$, the superlattices of $2\sqrt{3}a \times 2a \times 2c$ for $x = 1/4$, and $\sqrt{3}a \times \sqrt{3}a \times 2c$ for $x = 1/3$ (Fig. 1.4). According to neutron powder diffraction patterns [48,49], the analysis by the Rietveld profile-fitting method has revealed that the site occupancy at each Fe site is not unity but some fractional, as shown by fan-shaped black area in Fig. 1.4. In the left side are shown schematic stacking layers of Ti, S, and Fe atoms along the $c$-axis for (a) $x = 0.15$, (b) $x = 1/4$, and (c) $x = 1/3$, where the guest Fe atom layers at the position $z$ are indicated by bold solid and broken lines. The site occupancies for $x = 0.15$ [Fig. 1.4(a)] are determined to be 0.0 and 0.2 at the sites 1a and 3c in the layer $z = 1/4$, and 0.3 and 0.1 at the sites

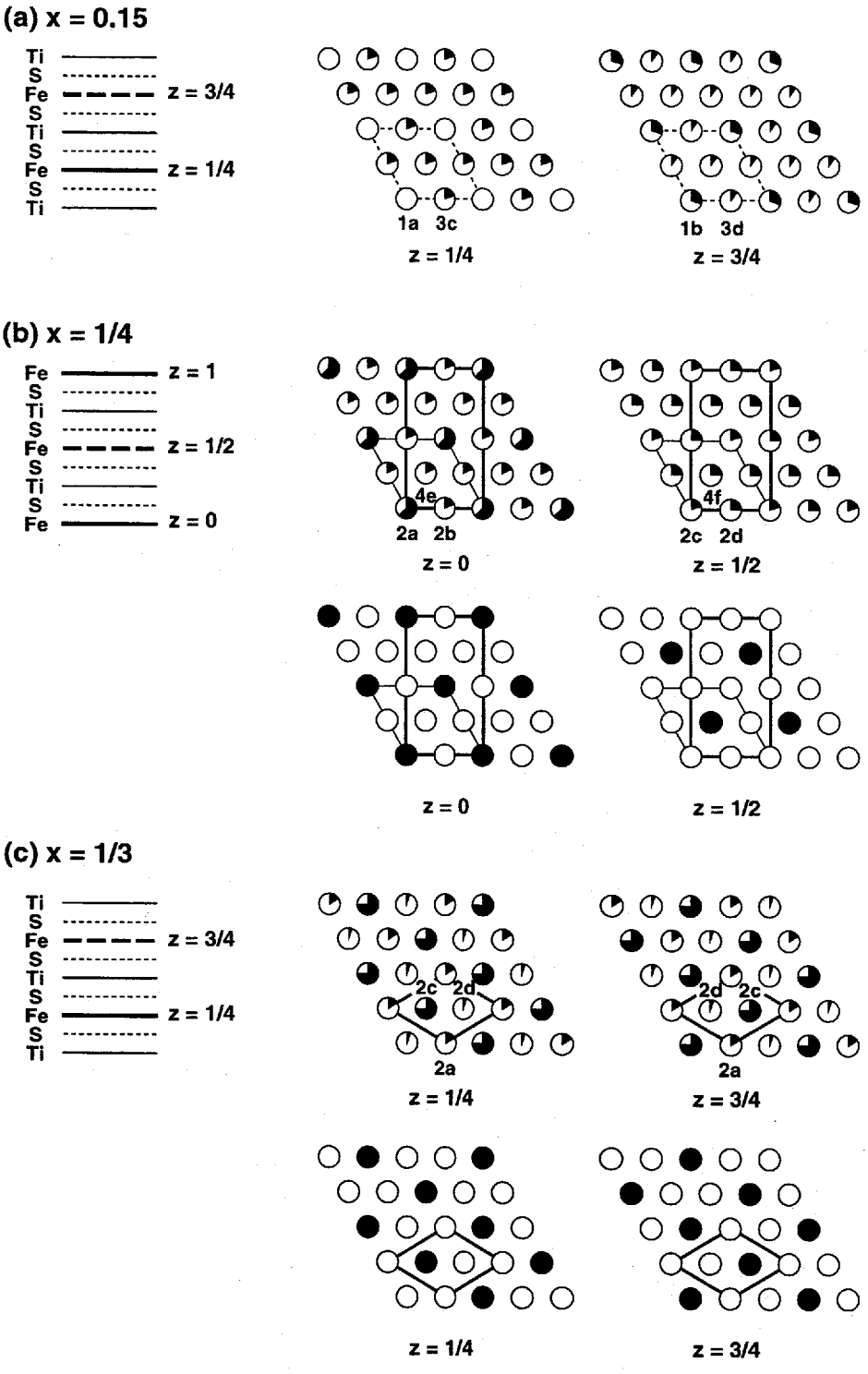


Fig. 1.4 (a) Short-range ordered structure $2a \times 2a \times 2c$ for $x = 0.15$, (b) $2\sqrt{3}a \times 2a \times 2c$ superlattice for $x = 1/4$, and (c) $\sqrt{3}a \times \sqrt{3}a \times 2c$ superlattice for $x = 1/3$, determined from the neutron diffraction for $Fe_xTiS_2$ [48]. In the left side are shown schematic stacking layers of Ti, S, and Fe atoms along the $c$-axis, where the guest Fe atom layers at the position $z$ are indicated by bold solid and broken lines. In the right side are shown the intralayer structures of Fe atoms at different positions. Broken lines mark the unit cell for $x = 0.15$, solid lines for $x = 1/4$ and $1/3$, and thin solid lines for the psuedo-hexagonal $2a \times 2a \times 2c$ superlattice with $x = 1/4$. Fan-shaped black area indicates the fractional site occupancy at each Fe site determined experimentally. Solid and open circles indicate the full site occupancy and vacancy, respectively, in the ideal superlattices for $x = 1/4$ at $z = 0$ and $1/2$, and for $x = 1/3$ at $z = 1/4$ and $3/4$.

1b and 3d in $z = 3/4$ of the short-range ordered lattice, respectively. Those for $x = 1/4$ [Fig. 1.4(b)] are determined to be 0.63, 0.19, and 0.18 at the sites 2a, 2b, and 4e in $z = 0$, and 0.20, 0.25, and 0.25 at the sites 2c, 2d, and 4f in $z = 1/2$ of the $2\sqrt{3}a \times 2a \times 2c$ superlattice, respectively. Since the occupancies of the 2b and 2c sites are nearly equal to those of the 4e and 4f sites, respectively, the Fe lattice is regarded to be in pseudo-hexagonal symmetry, forming approximately the $2a \times 2a \times 2c$ superlattice, as indicated by thin solid lines in Fig. 1.4(b). For $x = 1/3$ [Fig. 1.4(c)], the site occupancies are 0.16, 0.75, and 0.05 at the sites 2a, 2c, and 2d in both $z = 1/4$ and $z = 3/4$ of the $\sqrt{3}a \times \sqrt{3}a \times 2c$ superlattice, respectively. These results suggest that in the real crystal of $Fe_xTiS_2$, the guest Fe atoms may have very complicated distributions in the van der Waals gaps.

Structural studies of $Ag_xTiS_2$ have been extensively done [50-57]. Ag guest atoms are inserted into the octahedral sites of the van der Waals gaps in the host $TiS_2$ to produce the stage-2 $Ag_xTiS_2$ for the intermediate guest concentration range, $0.13 \leq x \leq 0.19$ [54] or $0.17 \leq x \leq 0.22$ [56], below and above which the stage-1' and stage-1 $Ag_xTiS_2$ are formed [54,56]. As shown in Fig. 1.5(a), the interlayer spacing $c/n$, which is given by lattice parameter $c$ divided by stage number $n$, increases with $x$ up to $x = 0.12$ for the stage-1' and above $x = 0.30$ for the stage-1, while it is almost constant for the stage-2 between $0.15 \leq x \leq 0.33$; we can see a clear jump between stage-2 and stage-1. The $c$-axis structure in the stage-2 $Ag_xTiS_2$ with $x = 0.18$-$0.19$ determined by X-ray diffraction [51] is illustrated in Fig. 1.5(b). Ag atom intercalation expands van der Waals gap remarkably from 2.85 Å to 3.56 Å and shifts the Ti layers to off-centered position between the S layers. The X-ray diffraction and heat capacity measurements revealed that an in-plane order-disorder phase transition of the guest atoms in $Ag_xTiS_2$ occurs around 250-300 K [56,57], and another transition from stage-2 to stage-1 structure does around 1200 K [54]. Furthermore, Kuroiwa *et al.* [58] measured the precise X-ray diffraction patterns of stage-2 $Ag_{0.15}TiS_2$, as well as stage-1 $Ag_{0.25}TiS_2$. They found that $Ag_{0.15}TiS_2$ shows the abrupt change of $c$-axis parameter around 250 K, rodlike diffuse scattering parallel to the $c^*$-axis at (1/3 1/3 0), (2/3 2/3 0) and their equivalent positions, and the two-dimensional disordered state above 250 K. Using the 2-dimensional short-range order parameters for $Ag_{0.15}TiS_2$ obtained experimentally from the diffuse scatterings, the in-plane local arrangements of Ag atoms have been calculated by the Monte Carlo (MC) technique to show the variation with temperature from the ordered states of $\sqrt{3}a \times \sqrt{3}a$ to the disordered states [58]. However, there is no report, to our knowledge, that calculate the equilibrium atomic distributions of this material taking account of some guest-guest interactions or interlayer interactions, as done for GIC [59,60]. Different type MC calculations [61] are made for Li distribution in $Li_xTiSe_2$ to compare with the experimental results of $^{77}Se$ and $^{7}Li$ NMR studies, where a Boltzmann type thermal relaxation is introduced to allow a lithium atom to jump to an available empty site.

In the present work, computer simulations for the equilibrium atomic distribution of intercalated guest atoms in 1T-$TiS_2$ using the MC method have been performed. Here we have taken into account *pair-interactions* between neighboring guest atoms in the triangular lattices stacked with six layers (lattice size for computation: $18 \times 18 \times 6$) with the periodic boundary condition along the $a$- and $c$-axis directions; the details of the calculations are presented in Chapter 2. I shall show the effect of various types of pair-interactions (between nearest neighbors and/or next-nearest neighboring guest atoms) on their atomic distributions in $G_xTiS_2$. In particular, Fe atomic distributions in $Fe_xTiS_2$ ($x = 0.15$, 1/4, and 1/3) have been calculated successfully to

reproduce the observed short-range order or superlattice with fractional Fe occupancy, and those in $Ag_{0.15}TiS_2$ to obtain the stage-2 structure showing X-ray diffuse rods. These calculated results are collected in Chapter 3. In Chapter 4, based on the calculated Fe atomic distributions, we shall discuss on the formation of guest atom clusters, percolation cluster, its dimensionality, magnetic properties of $Fe_xTiS_2$, and the change in the local structures near the host sulfur atoms by intercalation in $M_xTiS_2$. The order-disorder phase transition in the $a$-axis plane for $Ag_{0.15}TiS_2$ will be discussed from the temperature variations in the calculated Ag atomic distributions. Furthermore, the pair-interaction strengths employed to obtain the atomic distributions for $Fe_xTiS_2$ and in $Ag_{0.15}TiS_2$ are discussed. The main results obtained in the present study are summarized in Chapter 5.

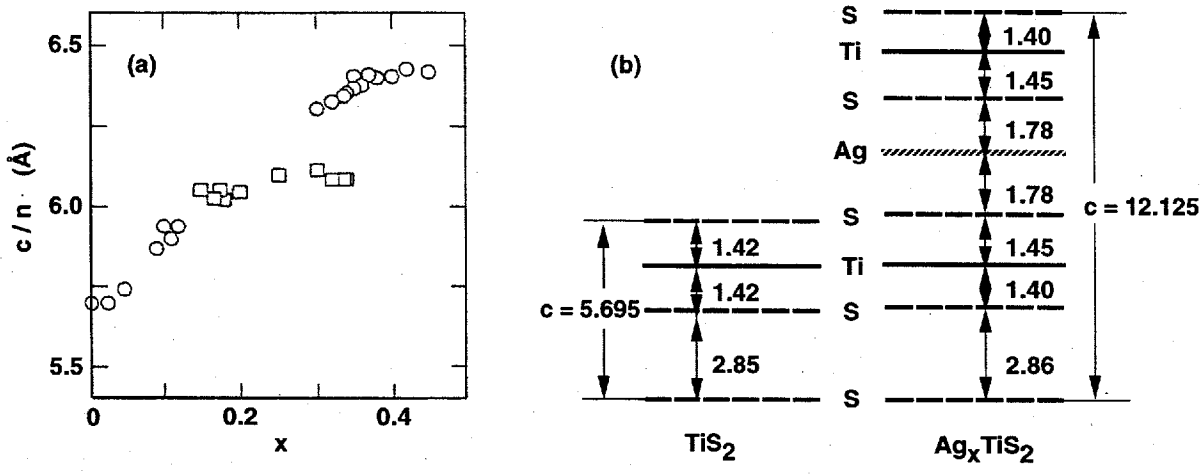


Fig. 1.5 (a) Lattice parameter $c$ normalized by the stage number $n$, $c/n$, for $Ag_xTiS_2$ plotted against the guest concentration $x$ [56]; circle and square symbols correspond to the stage-1 ($n = 1$) and stage-2 ($n = 2$), respectively. (b) The $c$-axis structures in $TiS_2$ and stage-2 $Ag_xTiS_2$ with $x = 0.18$-$0.19$; the interlayer distances are given in units of Å [51].

# Chapter 2

# Calculations

## §2.1 Model Hamiltonian

In the intercalation compound $G_xTiS_2$, the stable atomic distribution of the guest atoms minimizes the total energy including many-body interactions among all guest and host atoms within the system. In the present calculations, we have simply taken into account the *pair-interactions* between the neighboring guest atoms $G$, which lie at the octahedral sites arranged in two-dimensional triangular lattices in the $a$-axis planes stacked along the $c$-axis, and performed the MC simulations for their atomic distributions.

We use the following Hamiltonian for the system,

$$H = -\sum_{<i,j>}\sum_{k} V_k n_i n_j^k , \tag{1}$$

where $n_i$ (= 1 or 0) is an occupancy of the $i$-th site, $n_j^k$ an occupancy of the $j$-th site located at the $k$-th neighboring position, and $V_k$ a pair-interaction strength between the guest atoms in the $k$-th neighbor. Here $k$ = a1, a2, a3, ... stand for the intralayer sites of the first nearest neighbors (1st NNs), the second (2nd NNs), the third (3rd NNs), ..., in the $a$-axis layer [Fig. 2.1(a)], $k$ = c1, c2, ..., for the interlayer sites of the 1st NNs, 2nd NNs, ... in the nearest layers separated by the lattice constant $c$, and $k$ = 2c for the 1st NNs in the next nearest layers separated by $2c$ along the $c$-axis [Fig. 2.1(b)]. In the above Hamiltonian we consider here at most five terms of $k$ = a1, a2, c1, c2, and 2c, as,

$$H = -\sum_{<i,j>} n_i \left( V_{a1} n_j^{a1} + V_{a2} n_j^{a2} + V_{c1} n_j^{c1} + V_{c2} n_j^{c2} + V_{2c} n_j^{2c} \right). \tag{2}$$

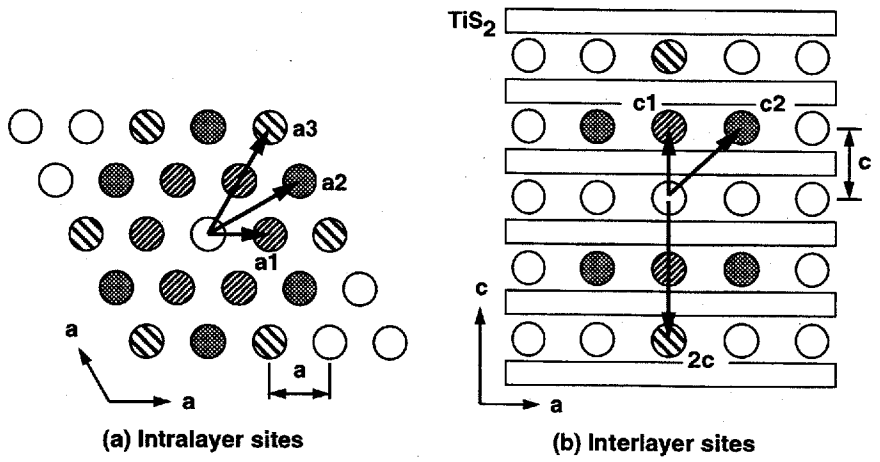


Fig.2.1 Definition of lattice sites used for the MC simulations. (a) Intralayer sites around a guest atom $G$ in the $a$-axis layer for $G_xTiS_2$, where a1, a2, and a3 stand for the 1st, 2nd, and 3rd NN sites, respectively. (b) Interlayer sites along the $c$-axis, where c1 and c2 stand for the 1st and 2nd NN sites in the nearest layers, respectively, and 2c the site in the next nearest layers.

## §2.2 Atomic distributions

For the triangular lattice stacked with six layers (lattice size: $N = 18 \times 18 \times 6$) with the periodic boundary condition along the $a$- and $c$-axis directions of $G_xTiS_2$, we have carried through the numerical calculations using Metropolis method, one of MC methods for canonical ensemble [62-65].

In the initial state, $Nx$ guest atoms are arranged following the relation,

$$n_i = 1 \quad (1 \le i \le Nx), \qquad n_i = 0 \quad (Nx < i \le N). \tag{3}$$

The example of the initial atomic distribution in the six consecutive layers ($m$ = 1-6) of $G_xTiS_2$ with $x = 0.25$ are shown in Fig. 2.2. Next, we select a vacant $s$-th site to transit from an occupied $i$-th site using random numbers, and estimate an energy change $\Delta H$ caused by this atomic transition; $\Delta H = H(n_i = 0, n_s = 1) - H(n_i = 1, n_s = 0)$. Then the transition probability $W$ from $i$-th site to $s$-th site is given by,

$$\begin{aligned} W &= \exp(-\Delta H/T) \quad \text{for} \quad \Delta H > 0 \\ &= \quad 1 \qquad\quad \text{for} \quad \Delta H \le 0. \end{aligned} \tag{4}$$

For a negative value of $\Delta H$, atomic transition from $i$-th site to $s$-th site occurs ($W = 1$), while for a positive value of $\Delta H$ it occurs with probability $W = \exp(-\Delta H/T)$, which is performed to allow the atomic transition only when the random number produced newly is less than $W$. In one Monte Carlo step (MCS), such an process is made successively for the $Nx$ guest atoms, yielding one atomic distribution pattern for MCS = 1. Thus we can obtain an equilibrium atomic distribution for $G_xTiS_2$ at given temperature $T$ with pair-interaction strengths, $V_k$, as parameters after appropriate MCSs; $V_k$ in units of K is used through this work.

In Fig. 2.2 are shown typical atomic distributions of $G_xTiS_2$ ($x = 0.25$) calculated with a repulsive pair-interaction strength $V_{a1}$ (= -10,000 K) at MCS = 0, 1, and 100, where the temperature is taken to be $T$ = 870 °C = 1,143 K, the growth temperature of $Fe_xTiS_2$ crystal by a chemical vapor technique [8]. With increasing MCS number, the guest atoms are scattered to be a nearly uniform atomic distribution. In order to make MCS effect more clear, the values of $E/Nx$ are plotted against MCS number for three cases calculated with fixed pair-interaction strength $V_{a1}$ (= 1,000 K, -1,000 K, and -10,000 K) in Fig. 2.3, from which it can be seen that the total energy $E$ of the system becomes almost constant beyond 60 MCS within calculational errors for all cases. In the present study, therefore, calculations up to 100 MCS were performed to obtain an equilibrium atomic distribution.

Furthermore, to characterize the obtained atomic distributions, we have evaluated the averaged number of the $k$-th neighboring atom, $z_k$ ($k$ = a1, a2, a3, c1, and 2c), defined by

$$z_k = \frac{1}{Nx} \sum_i \sum_j n_i n_j k. \tag{5}$$

The value of $z_k$ for one pattern is obtained as the averaged value over MCS = 61-100, and then the most probable value and the deviation of $z_k$ are obtained from 10 patterns produced from different random seeds.

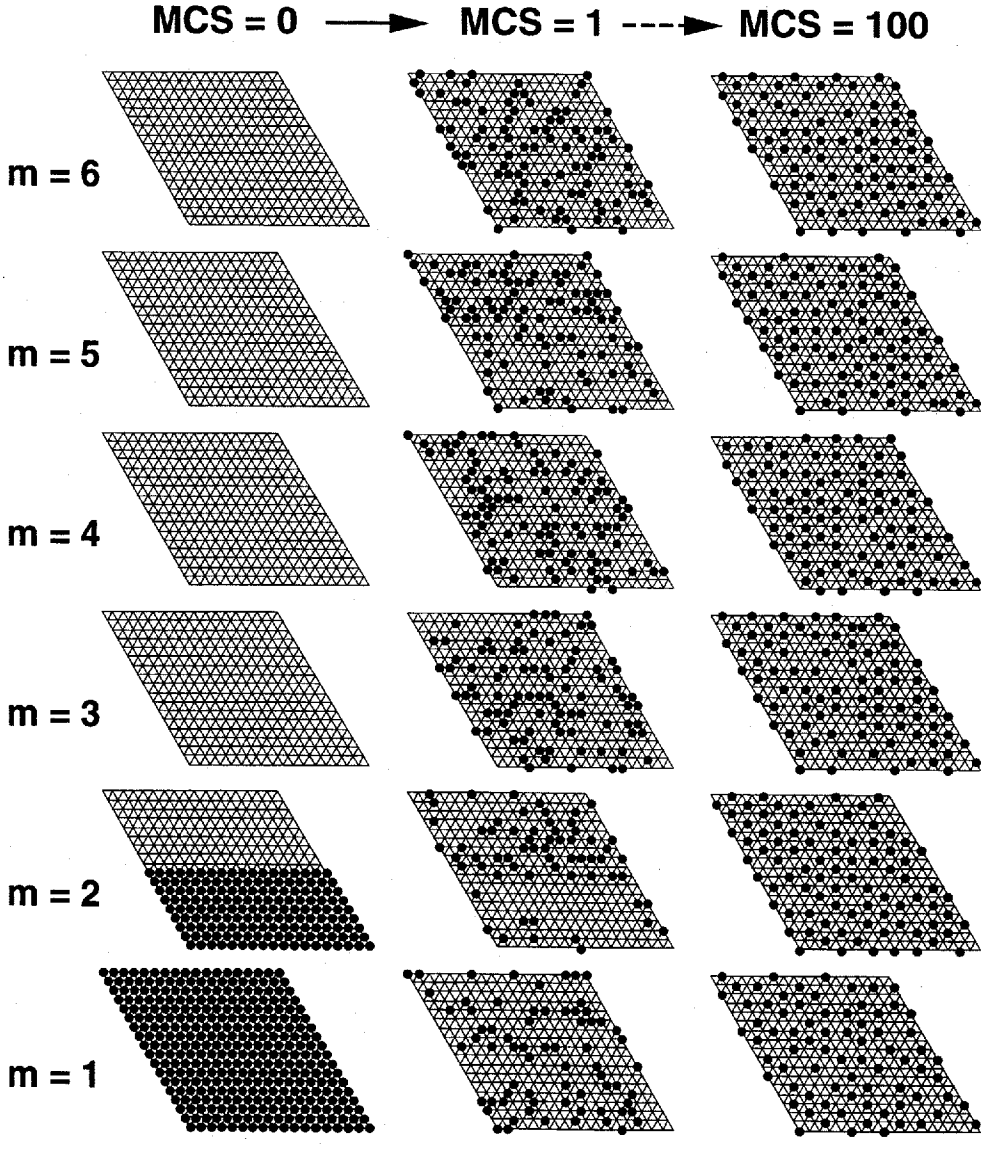


Fig.2.2 Typical examples of the variation in guest atomic distributions with Monte Carlo step (MCS) from the initial state (MCS = 0) for $G_xTiS_2$ ($x = 0.25$) with interaction strengths $V_{a1}$ = -10,000 K.

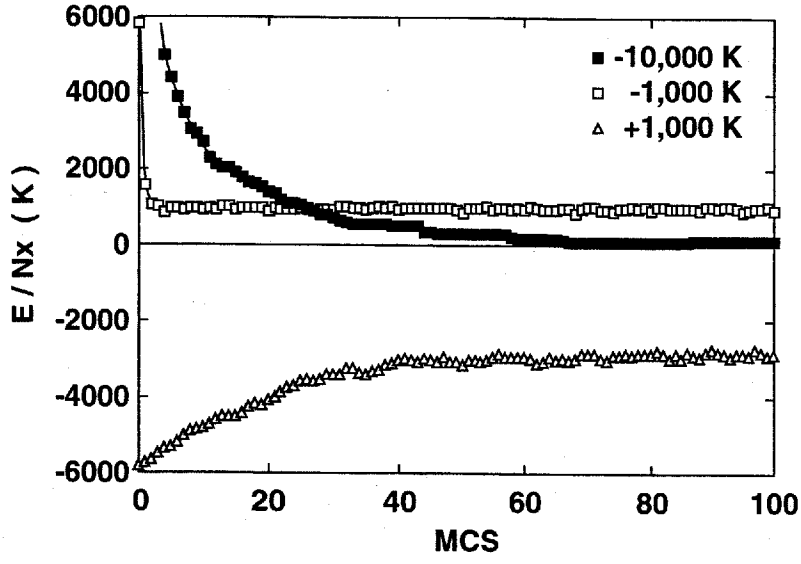


Fig.2.3 Typical examples of the variation in the total energy $E$ with MCS. The values of $E$ divided by the number of the guest atoms $Nx$, $E/Nx$, are plotted against the MCS number for $G_xTiS_2$ ($x = 0.25$) with three different interaction strengths $V_{al}$ = -10,000 K (solid squares), -1,000 K (open squares), and +1,000 K (open triangles).

## §2.3 X-ray diffraction intensities

Using the atomic distributions obtained by MC simulations, we have calculated the X-ray diffraction intensities. The X-ray intensity at a reciprocal lattice point ($\xi\ \eta\ \zeta$) in the unit cell of $TiS_2$ is expressed by

$$I(\xi\ \eta\ \zeta) = \frac{1}{v^2}\frac{1+\cos^2 2\theta}{2}\left|F(\xi\ \eta\ \zeta)\right|^2, \tag{6}$$

where $v$ is a volume of the lattice corresponding to a normalized factor, $(1+\cos^2 2\theta)/2$ is the polarization factor, and the structure factor $F(\xi\ \eta\ \zeta)$ is given by the summation of the product of the atomic scattering factor $f_A(2\theta)$ and the geometrical factor $F_A(\xi\ \eta\ \zeta)$ for the constituent elements $A$ = Ti, S, and guest element $G$ as, $F(\xi\ \eta\ \zeta) = \Sigma f_A(2\theta)\ F_A(\xi\ \eta\ \zeta)$. For the atomic distribution obtained with the site occupancy of the $i$-th site $n_i$ and its position $(x_i\ y_i\ z_i)$, $F_G(\xi\ \eta\ \zeta)$ is written as,

$$F_G(\xi\ \eta\ \zeta) = \Sigma\, n_i \exp[2\pi\, \mathrm{i}\, (\xi x_i + \eta y_i + \zeta z_i)], \tag{7}$$

from which the intensity of any reciprocal lattice point ($\xi\ \eta\ \zeta$) can be evaluated.

We should note here that the calculated X-ray intensities from a single pattern of the atomic distribution in the $18 \times 18 \times 6$ lattice depend strongly on the 'random seeds' used, but the averaged number of the NN atoms, $z_k$, is almost independent of the 'random seeds'. This means that the lattice size $18 \times 18 \times 6$ we employed may be too small to reproduce the structural details in the real system. Therefore, we have taken the averaged intensities of ten patterns simulated using different random seeds to obtain reasonable intensity profiles, which are insensitive to the random seeds used.

# Chapter 3

# Calculated Results

## §3.1 Effect of pair-interaction $V_{a1}$ on atomic distribution

At first, we have calculated the atomic distribution by considering only the pair-interaction $V_{a1}$ between the 1st NN guest atoms in $G_xTiS_2$ over the whole concentration $x$ = 0-1, where the temperature is taken to be $T$ = 870 °C = 1,143 K, the growth temperature of $M_xTiS_2$ crystal by a chemical vapor technique [8]. The interaction strength $V_{a1}$ is taken to be from -10,000 K to 10,000 K by a step of 1,000 K; the ratio of $V_{a1}$ to $T$ (= 1,143 K), $V_{a1}/T$, is nearly from -9 to 9. As typical results, the calculated equilibrium distributions in the six consecutive layers ($m$ = 1-6 from bottom to top; see Fig. 2.2) of $G_xTiS_2$ with guest concentration $x$ = 0.15, 0.25, 0.333, and 0.50 are shown in Figs. 3.1-3.4, respectively, for five cases of attractive interaction ($V_{a1}$ = 10,000 K, 1,000 K), no interaction ($V_{a1}$ = 0 K), and repulsive interaction ($V_{a1}$ = -1,000 K, -10,000 K). In the case of $V_{a1}$ = 0 K, the atoms are distributed randomly [Figs. 3.1(c)-3.4(c)]. For the strong attractive interaction of $V_{a1}$ = 10,000 K, they remain in the same pattern as the initial condition [Figs. 3.1(a)-3.4(a)], because the transition probability is vanishingly small [$\exp(-\Delta H/T) = \exp(-60{,}000\ \text{K}/1{,}143\ \text{K}) \sim 10^{-22}$]. For the attractive force of $V_{a1}$ = 1,000 K comparable to $T$, they stand to gather to form some 'clusters' in each layer [Figs. 3.1(b)-3.4(b)]. While those for the repulsive interactions of $V_{a1}$ are scattered a little for $V_{a1}$ = -1,000 K [Figs. 3.1(d)-3.4(d)], and homogeneously over the lattice sites for the strong repulsion of $V_{a1}$ = -10,000 K [Figs. 3.1(e)-3.4(e)]. Thus we see that the calculated distribution patterns are strongly dependent on the pair-interaction strength $V_{a1}$. Moreover, we can see some ordering atomic arrangements in the $a$-axis planes in the patterns calculated with the repulsive pair-interaction $V_{a1}$, which are nearly to the superstructures $2a \times 2a$ for $x$ = 0.25 [Fig. 3.2(e), $V_{a1}$ = -10,000 K] and $\sqrt{3}a \times \sqrt{3}a$ for $x$ = 0.333 [Fig. 3.3(e), $V_{a1}$ = -10,000 K], and labyrinth-like patterns for $x$ = 0.50 [Fig. 3.4(d), $V_{a1}$ = -1,000 K; Fig 3.4(e), $V_{a1}$ = -10,000 K].

The averaged number of the neighboring atoms $z_k$ [Eq. (5)] ($k$ = a1, a2, a3, c1, and 2c ) is plotted against $V_{a1}$ for different guest concentrations $x$ = 0.15, 0.25, 0.333, and 0.50 in Fig. 3.5. The values of each $z_k$ are not changed for the attractive interaction $V_{a1}$ larger than the system temperature $T$ (= 1,143 K), $V_{a1} \geq$ 2,000 K, where the calculated atomic distributions are the same as the initial patterns because of the vanishingly small transition probability ($< 3 \times 10^{-5}$), as described above for $V_{a1}$ = 10,000 K [Figs. 3.1(a)-3.4(a)]. For $V_{a1} \leq$ 1,000 K, on the other hand, $z_k$ depends remarkably on $V_{a1}$ along the $a$-axis direction, while it is constant along the $c$-axis direction. With decreasing $V_{a1}$, $z_{a1}$ decreases, $z_{a2}$ shows a minimum at $V_{a1}$ = 0 K, and $z_{a3}$ shows a plateau between -2,000 K and 1,000 K. The value of $z_k$ for $k$ = c1 and 2c is proportional to $x$, as the results of the random distributions along the $c$-axis direction.

In Fig. 3.6 are depicted the guest concentration dependence of the averaged number of the neighboring atoms $z_k$ calculated with different pair-interaction strengths $V_{a1}$. For $V_{a1}$ = 0 K (solid circles), $z_k$ is proportional to $x$ ($z_k = 6x$ for $k$ = a1, a2, and a3, and $z_k = 2x$ for $k$ = c1 and 2c). This

result means that the atomic distributions are random both in the $a$-axis plane and along the $c$-axis. However, the concentration dependence of the averaged numbers $z_{a1}$, $z_{a2}$, and $z_{a3}$ in the $a$-axis plane is quite different for attractive and repulsive pair-interactions. For $V_{a1}$ = 1,000 K and 10,000 K, the values of $z_{a1}$, $z_{a2}$, and $z_{a3}$ increase profoundly with $x$ compared with those for $V_{a1}$ = 0 K. For a repulsive pair-interaction, $z_{a1}$ is decreased by varying from $V_{a1}$ = -1,000 K to -10,000 K. In particular, for $V_{a1}$ = -10,000 K, we get $z_{a1} \sim 0$ up to $x = 0.333$, while the curves for $z_{a2}$ shows two humps at $x = 0.333$ and 0.666, where that of $z_{a3}$ has two dips. These two characteristic concentrations are corresponding to the structural ordering $\sqrt{3}a \times \sqrt{3}a$ in the $a$-axis plane observed experimentally. On the other hand, the values of $z_{c1}$ and $z_{2c}$ along the $c$-axis are almost independent of $V_{a1}$. These results indicate that the pair-interaction between the 1st NNs in the $a$-axis plane also affects the distribution of the 2nd and 3rd NNs in the planes. According to the EXAFS spectra for $M_xTiS_2$ ($M$ = Mn, Fe, Co, and Ni, $0 \le x \le 0.33$) [11,12], $z_{a1} \sim 0$ in the real system, which suggests that there exists a very strong repulsive interaction, in accordance with our calculations ($V_{a1}$ = - 10,000 K).

### §3.2 Effect of $V_{a2}$ and $V_{c1}$ on atomic distributions

Furthermore, we have investigated the effect of pair-interactions of the 2nd NNs in the $a$-axis plane, $V_{a2}$, and of the 1st NNs in the nearest layers along the $c$-axis, $V_{c1}$, on the atomic distributions. For simplicity, in the Hamiltonian we consider only two terms of $k$ = a1 and a2 in the $a$-axis plane, and $k$ = a1 and c1 along the $c$-axis, respectively, as

$$H = -\sum_{<i,j>} n_i \left( V_{a1} n_j^{a1} + V_{a2} n_j^{a2} \right), \text{ and } H = -\sum_{<i,j>} n_i \left( V_{a1} n_j^{a1} + V_{c1} n_j^{c1} \right). \quad (8)$$

With the strong repulsive pair-interaction ($V_{a1}$ = -10,000 K) obtained above, we have calculated the atomic distribution and averaged number $z_k$ for $G_xTiS_2$ ($x$ = 0.15, 0.25, 0.333, and 0.50), with $V_{a2}$ and $V_{c1}$ as parameters.

The averaged numbers $z_k$ for $k$ = a1, a2, a3, c1, and 2c are plotted against $V_{a2}$ and $V_{c1}$ in the left and right sides of Fig. 3. 7, respectively. As can be seen, with increasing $V_{a2}$, the values of $z_{a2}$ show a sharp increase around $V_{a2} \sim 0$, and those of $z_{a3}$ a sharp decrease, but the values of $z_{a1}$, $z_{c1}$, and $z_{2c}$ are almost unchanged. With increasing $V_{c1}$, on the other hand, both $z_{c1}$ and $z_{2c}$ show an appreciable change near $V_{c1} \sim 0$, but $z_{a1}$, $z_{a2}$, and $z_{a3}$ remain unchanged. For any set of these two pair-interaction strengths $V_{a1}$ and $V_{a2}$ or $V_{a1}$ and $V_{c1}$, however, the atomic distribution having the $2c$-periodicity along the $c$-axis for $Fe_xTiS_2$ observed experimentally cannot be reproduced, suggesting a need for further additional pair-interaction between the guest atoms separated by $2c$, $V_{2c}$.

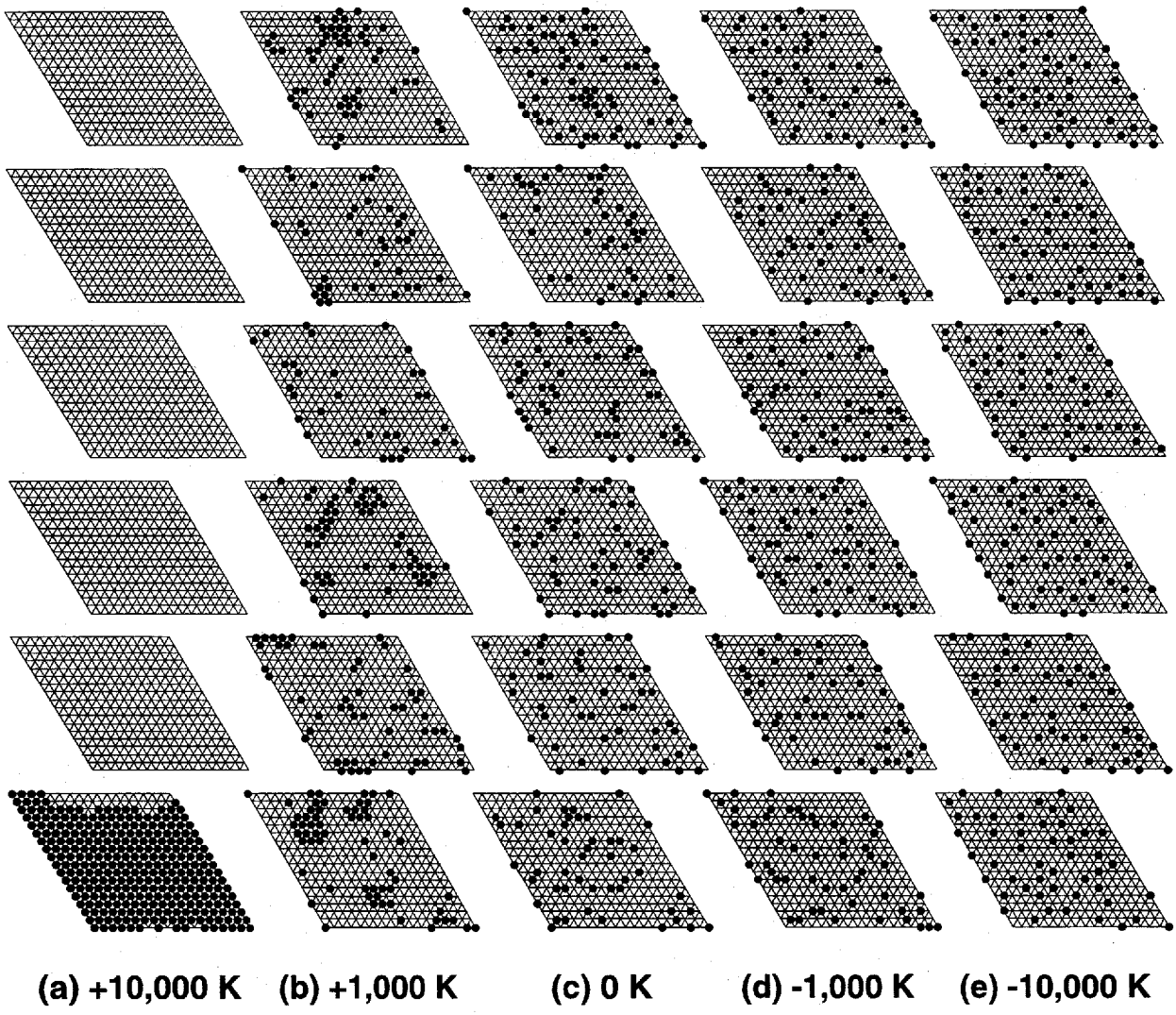


Fig. 3.1 Atomic distributions of guest atoms $G$ in the six consecutive $a$-axis layers ($m$ = 1-6 from bottom to top) for $G_xTiS_2$ ($x = 0.15$), calculated with (a) attractive interaction $V_{a1}$ = +10,000 K, (b) $V_{a1}$ = +1,000 K, (c) no interaction $V_{a1}$ = 0 K, (d) repulsive interaction $V_{a1}$ = -1,000 K, and (e) $V_{a1}$ = -10,000 K.

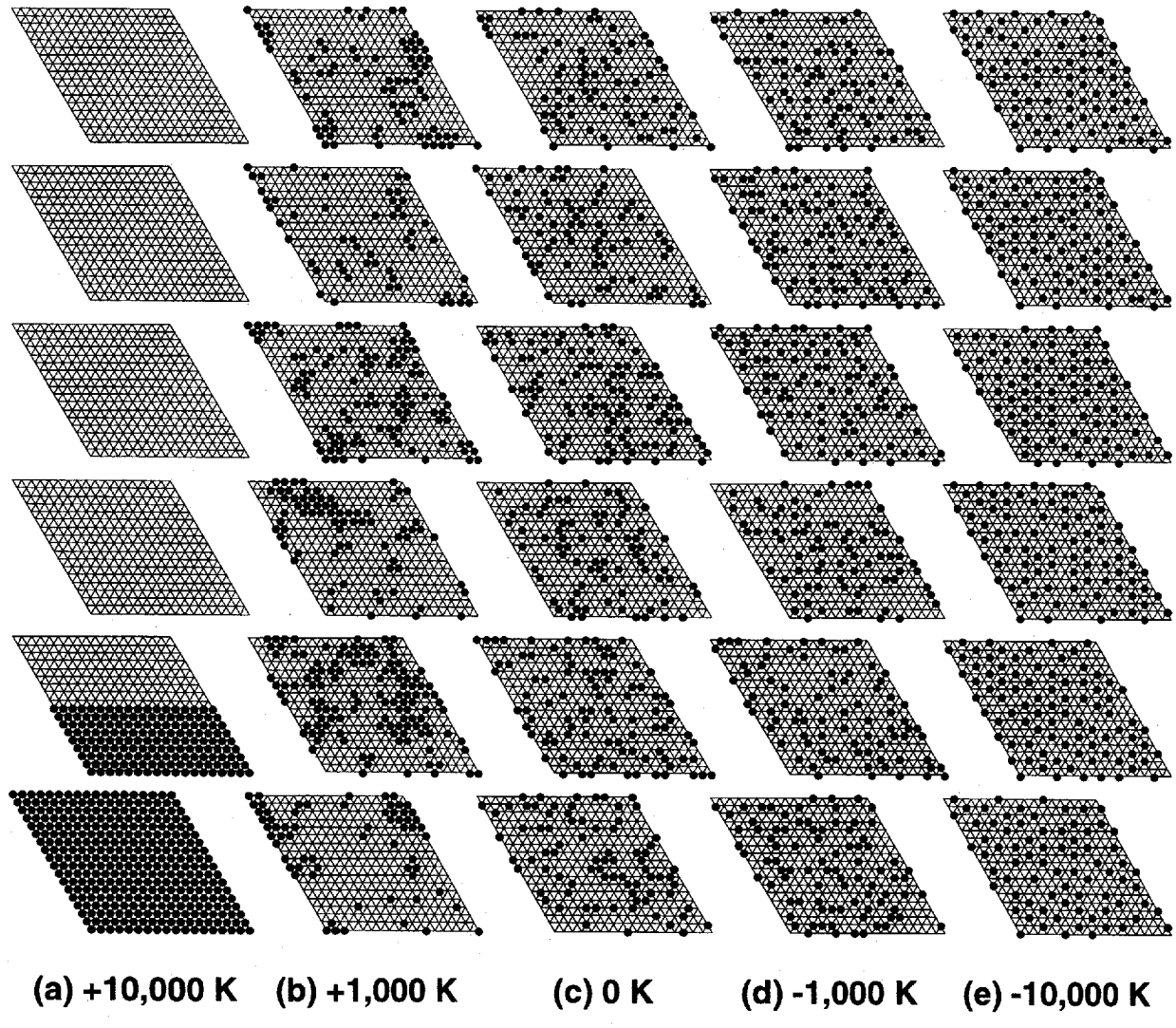


Fig. 3.2 Atomic distributions for $G_xTiS_2$ ($x = 0.25$), calculated with (a) $V_{al}$ = +10,000 K, (b) $V_{al}$ = +1,000 K, (c) $V_{al}$ = 0 K, (d) $V_{al}$ = -1,000 K, and (e) $V_{al}$ = -10,000 K.

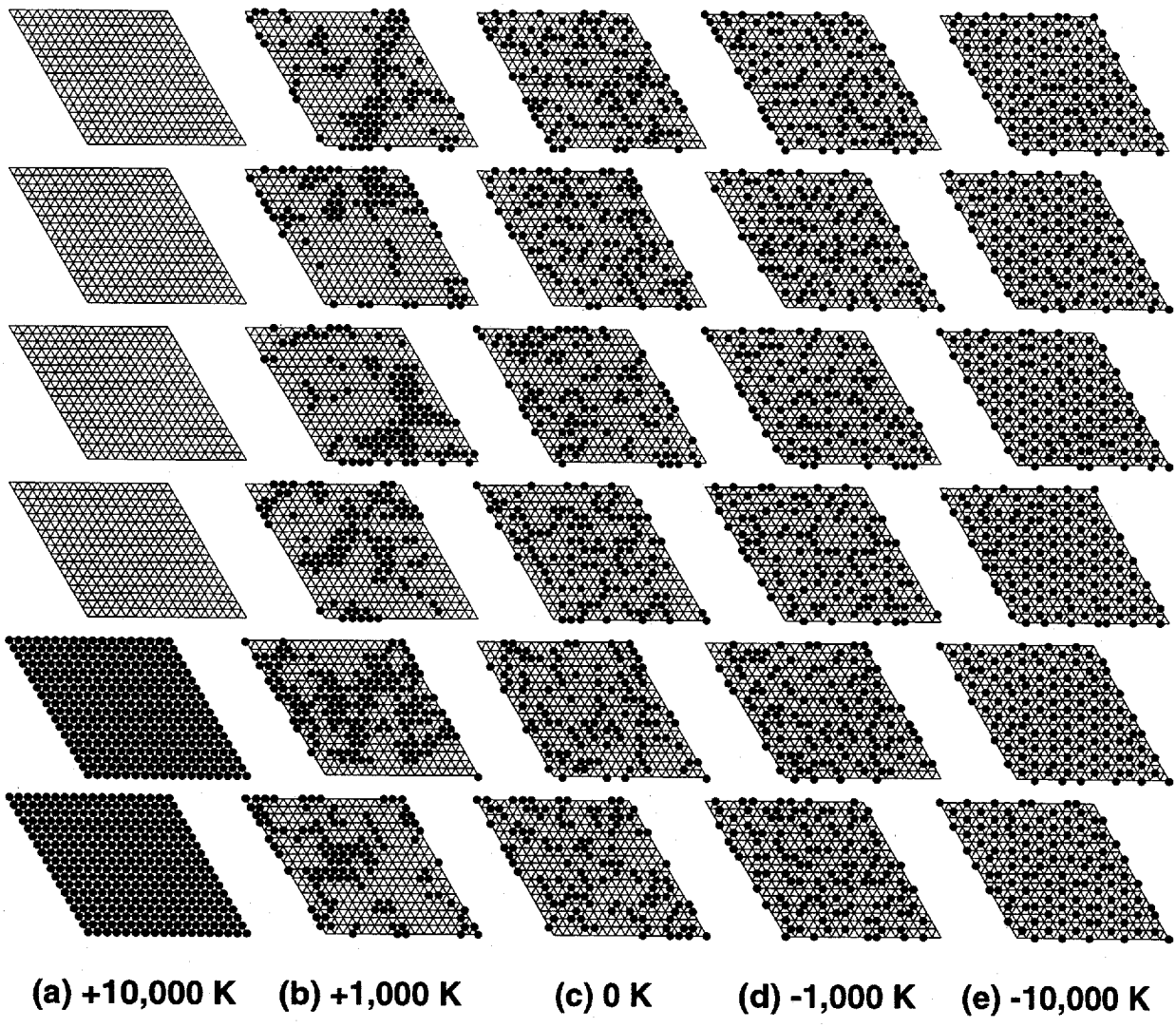


Fig. 3.3 Atomic distributions for $G_xTiS_2$ ($x = 0.333$), calculated with (a) $V_{al} = +10{,}000$ K, (b) $V_{al} = +1{,}000$ K, (c) $V_{al} = 0$ K, (d) $V_{al} = -1{,}000$ K, and (e) $V_{al} = -10{,}000$ K.

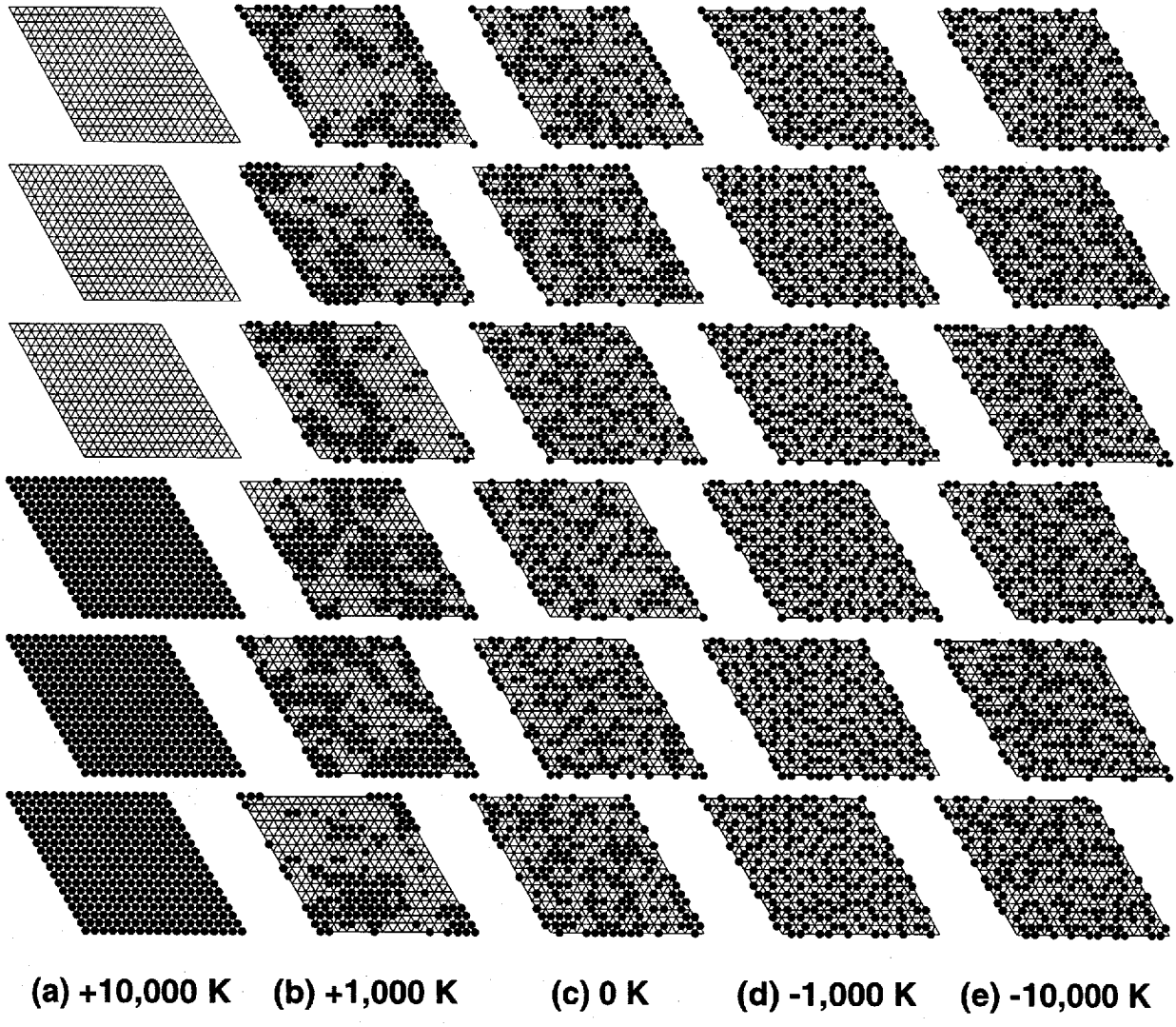


Fig. 3.4 Atomic distributions for $G_xTiS_2$ ($x = 0.50$), calculated with (a) $V_{al} = +10{,}000$ K, (b) $V_{al} = +1{,}000$ K, (c) $V_{al} = 0$ K, (d) $V_{al} = -1{,}000$ K, and (e) $V_{al} = -10{,}000$ K.

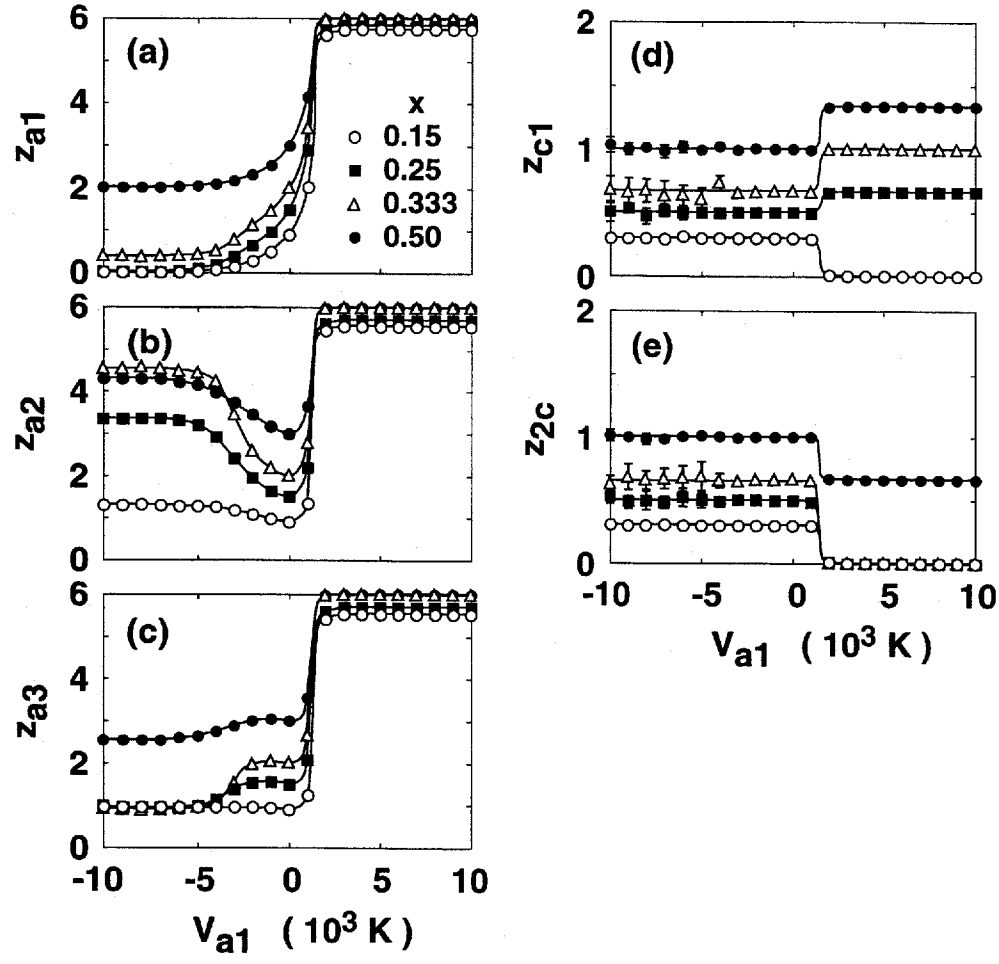


Fig. 3.5 Averaged number of neighboring guest atoms in the atomic distributions for $G_xTiS_2$ with $x$ = 0.15, 0.25, 0.333, and 0.50, $z_k$ ($k$ = a1, a2, a3, c1, and 2c), plotted against pair-interaction strength $V_{a1}$.

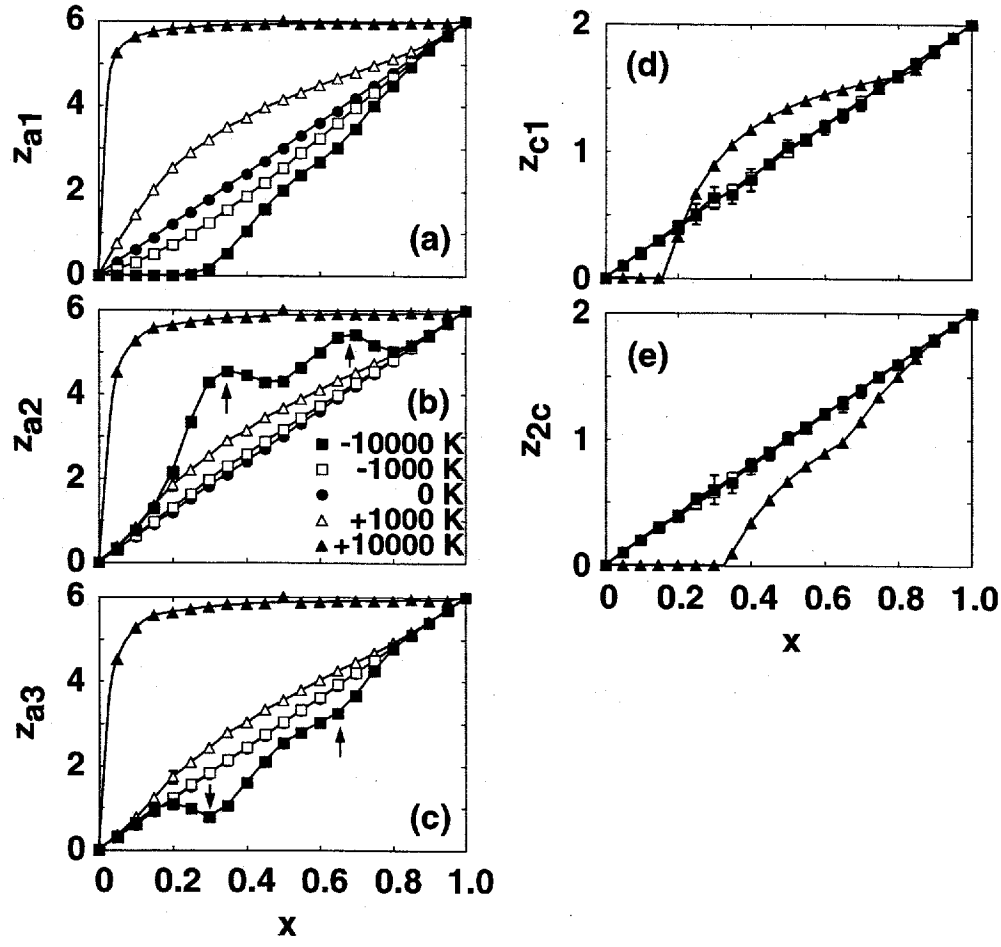


Fig. 3.6 Concentration dependence of $z_k$ for $G_x TiS_2$, calculated with the different fixed pair-interaction strength $V_{a1}$ (= -10,000 K, -1,000 K, 0 K, +1,000 K, and +10,000 K).

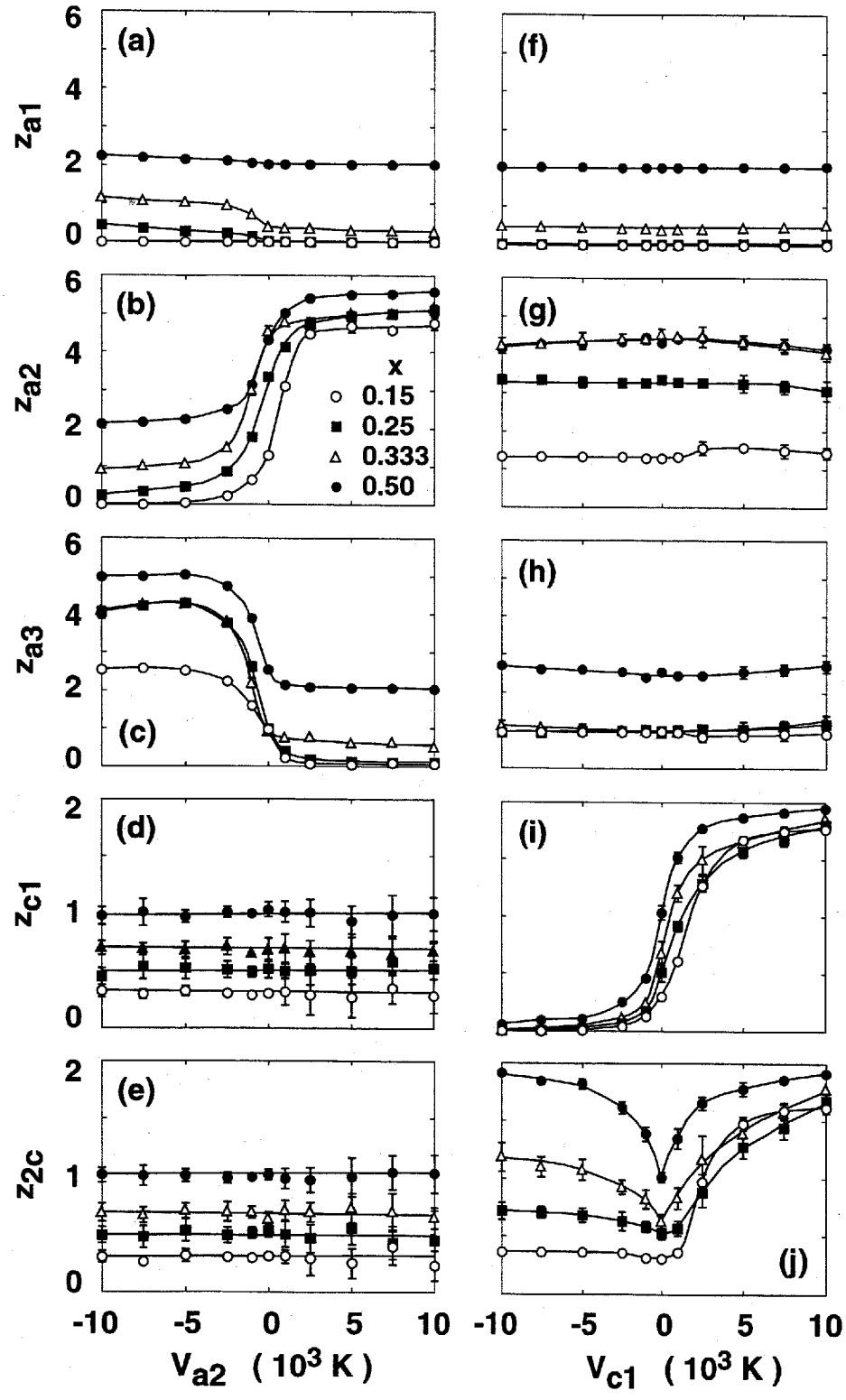


Fig. 3.7 Dependence of $z_k$ on $V_{a2}$ (left side) and on $V_{c1}$ (right side) for $G_xTiS_2$ ($x$ = 0.15, 0.25, 0.333, and 0.50), calculated with the fixed pair-interaction strength $V_{a1}$ (= -10,000 K).

## §3.3 Atomic distribution in $Fe_xTiS_2$

In order to reproduce the observed short-range $2c$-periodicity along the $c$-axis for $x = 0.15$ and the long-range one for $x = 1/4$ and $1/3$ [47], we have taken four pair-interactions $V_{a1}$, $V_{a2}$, $V_{c1}$, and $V_{2c}$, as

$$H = -\sum_{<i,j>} n_i \left( V_{a1} n_j^{a1} + V_{a2} n_j^{a2} + V_{c1} n_j^{c1} + V_{2c} n_j^{2c} \right). \tag{9}$$

Hereafter we call it *multiple pair-interaction model*. Using a set of parameters $V_k$ ($k$ = a1, a2, c1, and 2c) ranging from -10,000K to 10,000 K by a step of 1,000 K, we have calculated the atomic distributions and X-ray patterns for $Fe_xTiS_2$ with $x = 0.15$, 0.25, and 0.333. And from the comparison of these results with the X-ray patterns observed experimentally [47] and those calculated with the form factors using the fractional occupancies determined from the neutron powder diffractions [48], we have obtained the best-fit values of $V_k$, as listed in Table I (see later in details). In Figs. 3.8(a)-3.8(c) are depicted the atomic distributions calculated with the best-fit values $V_k$ for $Fe_xTiS_2$ with $x = 0.15$, 0.25, and 0.333, respectively, in the six consecutive layers.

Reflecting the strong repulsive interactions ($V_{a1}$ = -10,000 K) in the $a$-axis and along the $c$-axis ($V_{c1}$ = -5,000 K), the Fe atoms are scattered with no nearest neighboring guest atoms in each layer and along the $c$-axis for all samples. In the case of $x = 0.15$ [Fig. 3.8(a)], many Fe atoms are arranged to have the 3rd NN atoms separated by the distance $2a$ each other in the $a$-axis plane, showing the short-range ordered structure of $2a \times 2a$. For $x = 0.25$ [Fig. 3.8(b)], almost all of the Fe atoms are arranged to have the 3rd NNs in the $a$-axis plane, and the arrangements in the 2nd NN layers ($k$ = 2c) along the $c$-axis are in good agreement with the observed superlattice $2\sqrt{3}a \times 2a \times 2c$ or $2a \times 2a \times 2c$. Furthermore, in the case of $x = 0.333$ [Fig. 3.8(c)], the Fe atoms have the 2nd NNs in the $a$-axis plane and $2c$-periodicity along the $c$-axis, forming the $\sqrt{3}a \times \sqrt{3}a \times 2c$ superlattice. From Table I, it is noted that the attractive interaction ($V_{2c}$ = +5,000 K) is necessary to produce the nearly regular patterns with the long-ranged $2c$-periodicity along the $c$-axis. In addition, we see that $V_{a2}$ is negative (repulsive interaction) for $x = 0.25$, while it is positive (attractive one) for $x = 0.333$, and thus the sign of $V_{a2}$ determines which sites (2nd NN or 3rd NN sites) are more stable and preferable in the $a$-axis plane of $Fe_xTiS_2$. Such variations of $V_{a2}$ and $V_{2c}$ with guest concentration $x$ might be ascribed to the simple approximation of the many-body interactions in $Fe_xTiS_2$ by the multiple two-body interactions between the guest atoms.

Based on the foregoing atomic distributions of the guest Fe atoms, we have evaluated the averaged number $z_k$ for the $k$-th neighboring atoms ($k$ = a1, a2, and a3 in the $a$-axis plane and $k$ = c1 and 2c along the $c$-axis). The results for $Fe_xTiS_2$ with $x = 0.15$, 0.25, and 0.333 are shown in the left, center, and right columns of Fig. 3.9, respectively, where the values of $z_k$ (indicated by rectangles) are plotted against $k$ (hereafter referred to as *number spectrum*) for four different distribution patterns, from the top to the fourth rows, calculated with the attractive interaction $V_{a1}$ (= +1,000 K) [Figs. 3.1(b)-3.3(b)], no interaction ($V_{a1}$ = 0 K) [Figs. 3.1(c)-3.3(c)], the repulsive one $V_{a1}$(= -10,000 K) [Figs. 3.1(e)-3.3(e)], and multiple pair-interaction [Figs. 3.8(a)-3.8(c), Table I].

In the case of $V_{a1}$ = 0 K, the value of $z_k$ is nearly equal to $z_k = 6x$ for $k$ = a1, a2, and a3, and

Table I Best-fit values of the multiple pair-interaction strengths (in units of K), $V_{a1}$, $V_{a2}$, $V_{c1}$, and $V_{2c}$, used for calculation of atomic distribution of the guest Fe atoms in $Fe_xTiS_2$ ($x = 0.15$, 0.25, and 0.333).

| $V_k$ | $x = 0.15$ | $x = 0.25$ | $x = 0.333$ |
|---|---|---|---|
| $V_{a1}$ | -10,000 | -10,000 | -10,000 |
| $V_{a2}$ | -5,000 | -5,000 | +5,000 |
| $V_{c1}$ | -5,000 | -5,000 | -5,000 |
| $V_{2c}$ | 0 | +5,000 | +5,000 |

$z_k = 2x$ for $k$ = c1 and 2c, as described earlier. For the attractive interaction, the number $z_k$ is reduced in the order, $z_{a1} > z_{a2} > z_{a3}$, which suggests the formation of some *clusters* of the 1st NNs, as described later. For the repulsive one, $z_{a1}$ becomes nearly zero but $z_{a2}$ has the largest value in the $a$-axis plane, and $z_{c1}$ and $z_{2c}$ have the same values as those for $V_{a1} = 0$ and + 1,000 K. Meanwhile, the case of the multiple pair-interaction model shows a different behavior. For $x$ = 0.15, $z_{a1}$ and $z_{a2}$ vanish but only $z_{a3}$ has a large value, which indicates that the guest Fe atoms of the 1st and 2nd NNs are scattered, but the 3rd NNs form the short-range order of the form $2a \times 2a$ in the $a$-axis plane. For $x$ = 0.25 and 0.333, $z_{a3}$ and $z_{a2}$ have the values as large as 4 and 5, respectively, while $z_{c1}$ is zero and $z_{2c} \sim 2$, indicating that their structures are similar to the $2a \times 2a$ and $\sqrt{3}a \times \sqrt{3}a$ superstructures, respectively, in the $a$-axis plane with the $2c$-periodicity along the $c$-axis.

Similarly, we have evaluated $z_k$ for the short-range ordered structure and the superlattices with fractional occupancies for $x$ = 0.15, 0.25, and 0.333 (Fig. 1.4), and the ideal superlattices for $x$ = 0.25 and 0.333 having site occupancy of unity (solid circles) or zero (open circles) [Figs. 1.4(b) and (c), respectively], as shown in the lower two rows of Fig. 3.9. For the lattices with fractional occupancies of $x$ = 0.15 and 0.25, $z_k$ = 1-2 for $k$ = a1, a2, and a3, whose spectra resemble to those for the random distributions ($V_{a1} = 0$ K). This similarity may be due to the small difference in the fractional occupancies at the guest atom sites. For $x$ = 0.333, the value of the 2nd NNs in the $a$-axis plane is largest among others ($z_{a2} = 3.7 >> z_{a1}, z_{a3}$), showing the large difference in the Fe occupancies. For the ideal superlattices, on the other hand, the guest atoms are arranged regularly to have $z_{a3} = 6$ and $z_{2c} = 2$ for $x$ = 0.25, and $z_{a2} = 6$ and $z_{2c} = 2$ for $x$ = 0.333.

## §3.4 X-ray diffraction patterns for $Fe_xTiS_2$

Experimental results of X-ray diffraction of $Fe_xTiS_2$ crystals with $x$ = 0.15, 1/4, and 1/3 [47] are illustrated in Fig. 3.10, where the diffuse scattering and superlattice reflection points are marked in the reciprocal lattice of $TiS_2$ in the left side, and their profiles parallel to the $c^*$-axis along (3/2 0 $\zeta$) for $x$ = 0.15, (0 1/2 $\zeta$) for $x$ = 1/4, and (1/3 1/3 $\zeta$) for $x$ = 1/3 are depicted in the right side. It is noted that the profile for $x$ = 0.15 is very broad centered on $\zeta$ = 0.5, while those for $x$ = 1/4 and 1/3 have sharp peaks at $\zeta$ = 0, 0.5, and 1.0.

In order to compare with these experimental results of $Fe_xTiS_2$, we have selected the reciprocal lattice points along ($\xi$ 1/2 1/2) and (3/2 0 $\zeta$) for $x = 0.15$, ($\xi$ 1/2 1/2) and (0 1/2 $\zeta$) for $x = 0.25$, and ($\xi$ 1/3 1/2) and (1/3 1/3 $\zeta$) for $x = 0.333$, and calculated the X-ray diffraction profiles from the obtained atomic distributions above using Eqs. (6) and (7). For the superlattices, we have employed the values of the fractional Fe occupancy $n_i$ determined experimentally [48,49] to calculate $F_{Fe}(\xi\ \eta\ \zeta)$ in Eq. (7).

The results are shown in Figs. 3.11-3.13 for $x = 0.15$, 0.25, and 0.333, respectively, where the intensity profiles parallel to the $a^*$-axis and to the $c^*$-axis are arranged in the left and right columns, respectively. Here are shown three or four X-ray patterns, from the top row to the bottom, for the distributions calculated with $V_{a1} = -10{,}000$ K [Figs. 3.1(e)-3.3(e)], multiple pair-interaction model (Fig. 3.8 and Table I), the superlattice with fractional occupancy, and ideal superlattice (Fig. 1.4). For the strong repulsive interaction ($V_{a1} = -10{,}000$ K), the X-ray intensities for three samples are too weak, as shown in the top rows of Figs. 3.11-3.13, which means that there is no obvious short- or long-range ordered structure in the $a$-axis plane and along the $c$-axis. The X-ray intensities calculated by the multiple pair-interaction model show characteristic profiles (second rows of Figs. 3.11-3.13): we note that (i) for $x = 0.15$, three peaks around $\xi = 0$, 0.5, and 1 along ($\xi$ 1/2 1/2) and a very broad peak around $\zeta = 0.5$ along (3/2 0 $\zeta$), (ii) for $x = 0.25$, three peaks around $\xi = 0$, 0.5, and 1 along ($\xi$ 1/2 1/2) and three peaks at $\zeta = 0$, 0.5, and 1 along (0 1/2 $\zeta$), and (iii) for $x = 0.333$, a peak around $\xi = 0.33$ along ($\xi$ 1/3 1/2) and three peaks at $\zeta = 0$, 0.5, and 1 along (1/3 1/3 $\zeta$). These calculated results are in qualitative agreement with those observed experimentally (Figs. 3.10) and also those calculated for the short-range ordered lattice ($x = 0.15$) and superlattices with the fractional Fe occupancy ($x = 0.25$ and 0.333) (third rows of Figs. 3.11-3.13).

The very broad peak around $\zeta = 0.5$ along (3/2 0 $\zeta$) for $x = 0.15$ is quite similar to the experimental profile in Fig. 3.10(a), revealing that the calculated atomic distribution has not a long-range order of $2c$ but a short-range order along the $c$-axis. Furthermore, it is noted that the calculated peaks along the $a^*$-axis are broader than those for the superlattices with fractional occupancy, which indicates a small deviation from the long-range ordered structure, or a randomness of the Fe atoms in the $a$-axis plane. Such randomness may have been omitted in the calculations for the superlattices with fractional Fe occupancy obtained by the Rietveld profile fitting.

The X-ray intensities for the ideal superlattice with the occupancy of unity or zero (bottom rows of Figs. 3.12 and 3.13) are much stronger than those for other distributions, by 10 times for $x = 0.25$ and double for $x = 0.333$. Especially, for $x = 0.25$ there is no peak at $\xi = 0.5$ and $\zeta = 0$ or 1 [Figs. 3.12 (d) and 3.12 (h)], the latter of which is quite different from the pattern observed experimentally [Figs. 3.10(b)].

Thus, from our MC simulations based on the multiple pair-interaction model, we have obtained reasonable X-ray diffraction patterns for $Fe_xTiS_2$ ($x = 0.15$, 0.25, and 0.333), in satisfactory agreement with the experiments.

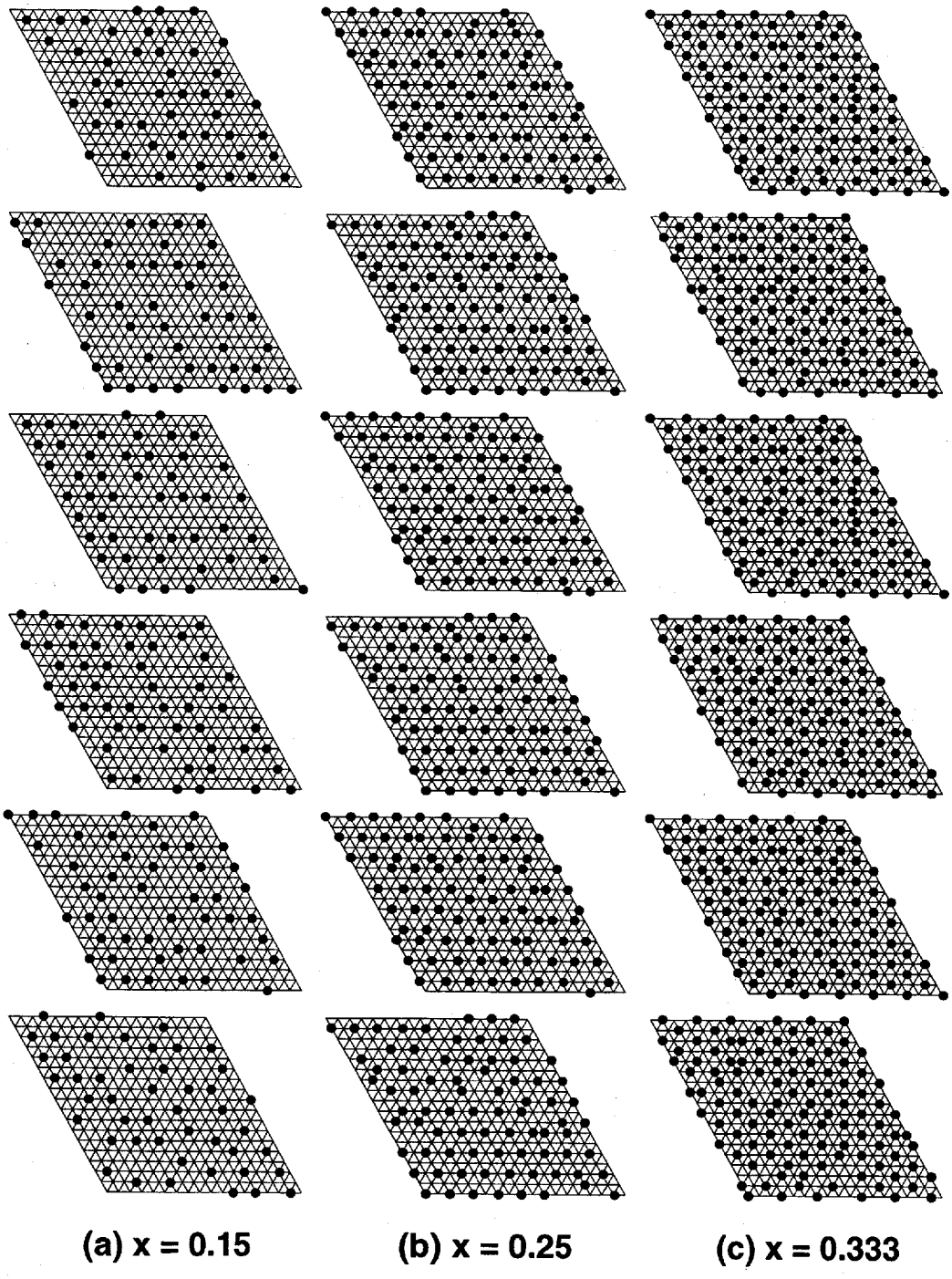


Fig. 3.8 Atomic distributions of the guest Fe atoms in $Fe_xTiS_2$ with (a) $x = 0.15$, (b) $x = 0.25$, and (c) $x = 0.333$, calculated with the multiple pair-interaction model (Table I).

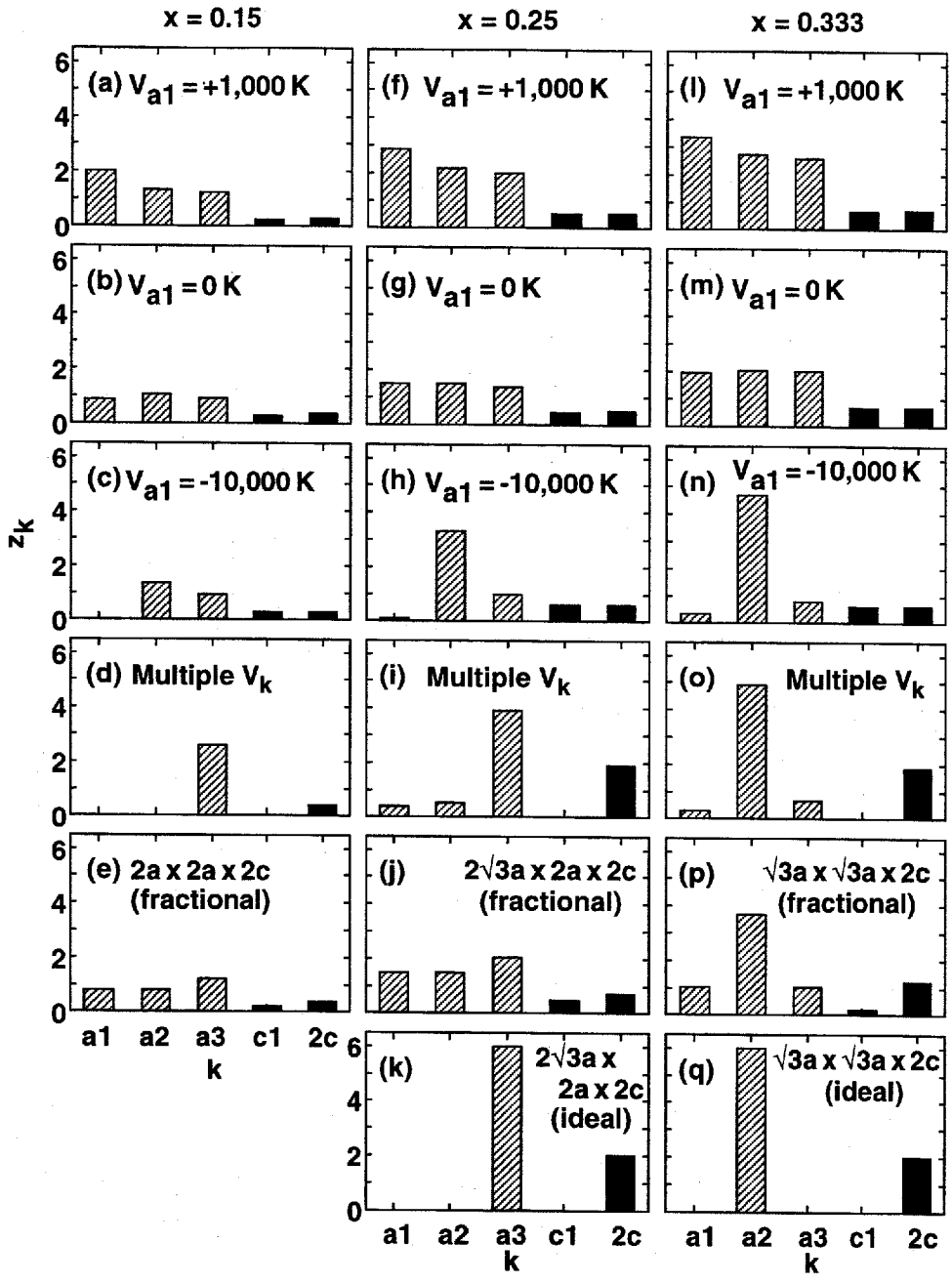


Fig. 3.9 Averaged number $z_k$ ($k$ = a1-2c) for different atomic distributions in $Fe_xTiS_2$ with $x$ = 0.15 (left column), $x$ = 0.25 (center column), and $x$ = 0.333 (right column), calculated with $V_{a1}$ = +1,000 K (top row), $V_{a1}$ = 0 K (second row), $V_{a1}$ = -10,000 K (third row), the multiple pair-interaction model (fourth row), the short-range ordered structure or superlattices with fractional site occupancy (fifth row), and the ideal superlattices (bottom row).

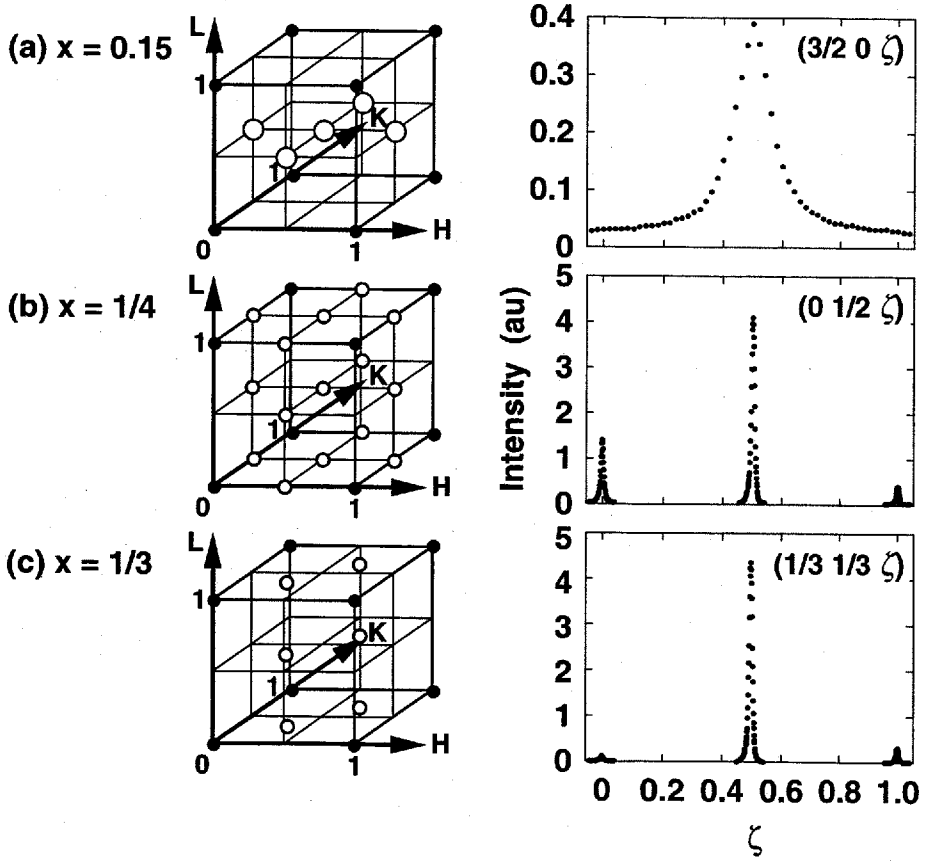


Fig. 3.10 Diffuse scattering and superlattice reflections of $Fe_xTiS_2$ single crystals with (a) $x = 0.15$, (b) $x = 1/4$, and (c) $x = 1/3$ in the reciprocal lattice of $TiS_2$[47]. Bragg reflections, diffuse scattering and superlattice reflections are marked by solid circles, large and small open circles, respectively. Right parts of each figure are profiles of diffuse scattering and superlattice reflections parallel to the $c^*$-axis along (a) (2/3 0 $\zeta$) for $x = 0.15$, (b) (0 1/2 $\zeta$) for $x = 1/4$, and (c) (1/3 1/3 $\zeta$) for $x = 1/3$.

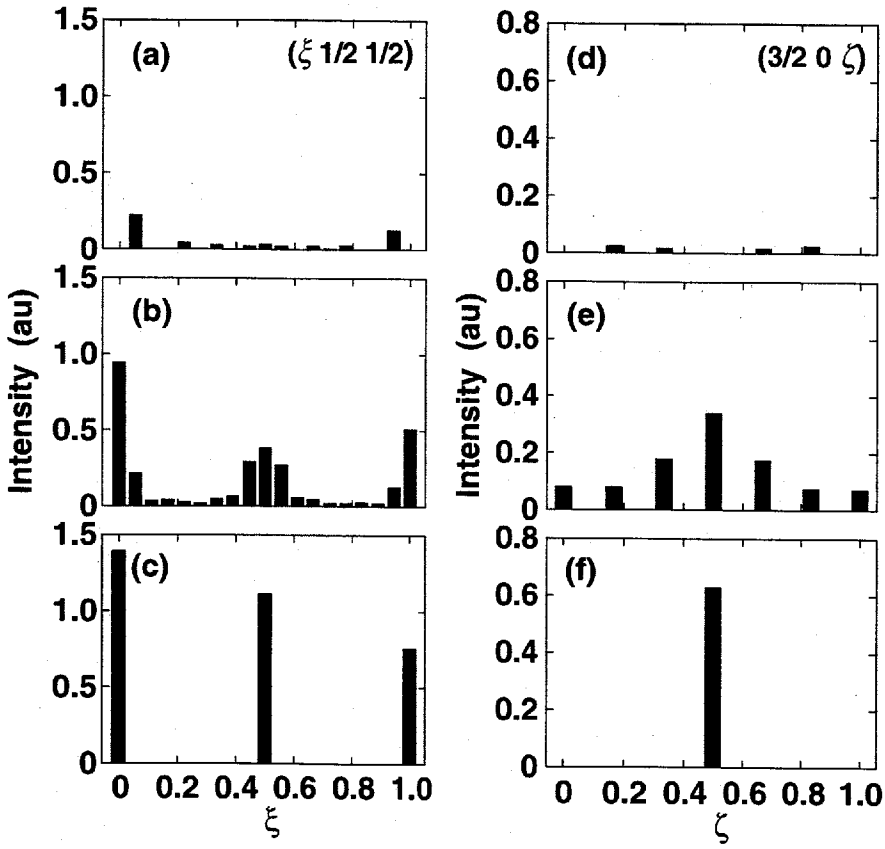


Fig. 3.11 X-ray diffraction intensities for $Fe_xTiS_2$ ($x = 0.15$) along ($\xi$ 1/2 1/2) parallel to the $a^*$-axis [left side, (a)-(c)] and along (3/2 0 $\zeta$) parallel to the $c^*$-axis [right side, (d)-(f)], calculated from three different atomic distributions with $V_{a1}$ = -10,000 K (top row), the multiple pair-interaction model (second row), and the short-range ordered structure $2a \times 2a \times 2c$ with fractional site occupancy (bottom row).

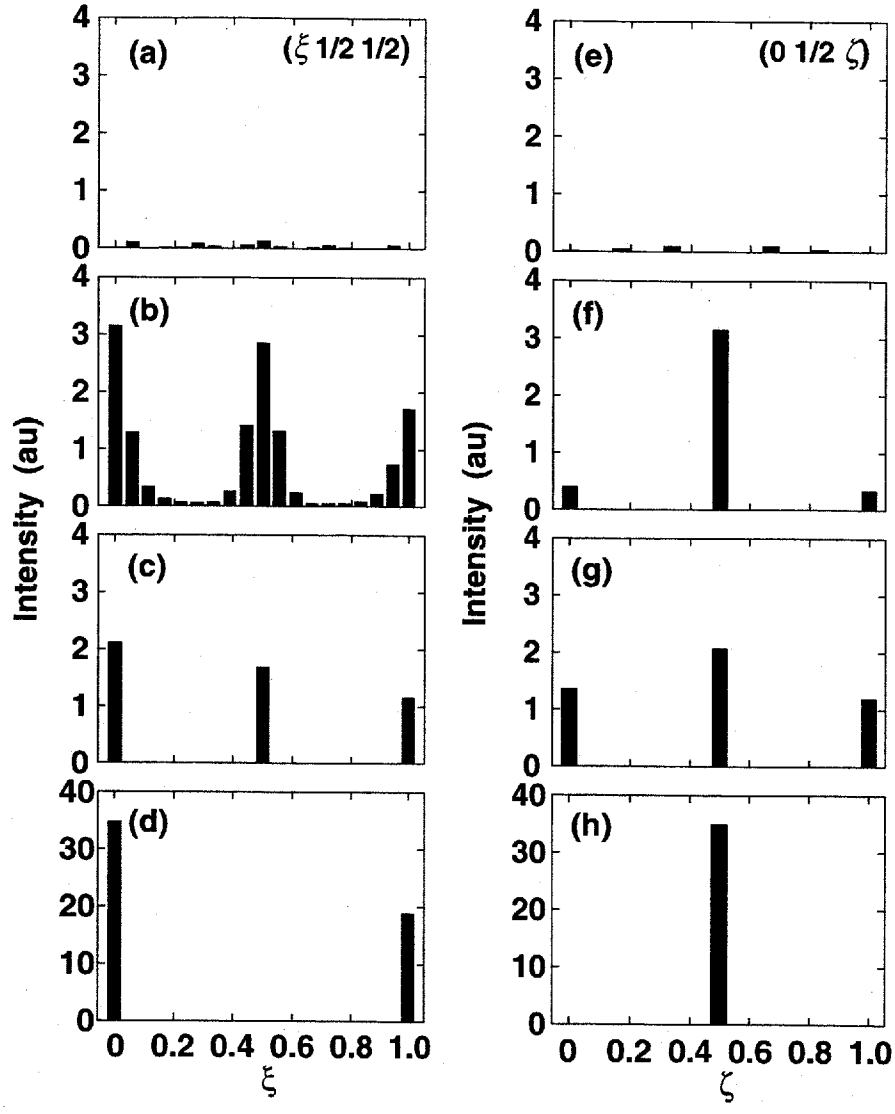


Fig. 3.12 X-ray diffraction intensities for $Fe_xTiS_2$ ($x$ = 0.25) along ($\xi$ 1/2 1/2) [left side, (a)-(d)] and along (0 1/2 $\zeta$) [right side, (e)-(h)], calculated from four different atomic distributions with $V_{al}$ = -10,000 K (top row), the multiple pair-interaction model (second row), the superlattice $2\sqrt{3}a \times 2a \times 2c$ with fractional site occupancy (third row), and the ideal superlattice $2\sqrt{3}a \times 2a \times 2c$ (bottom row).

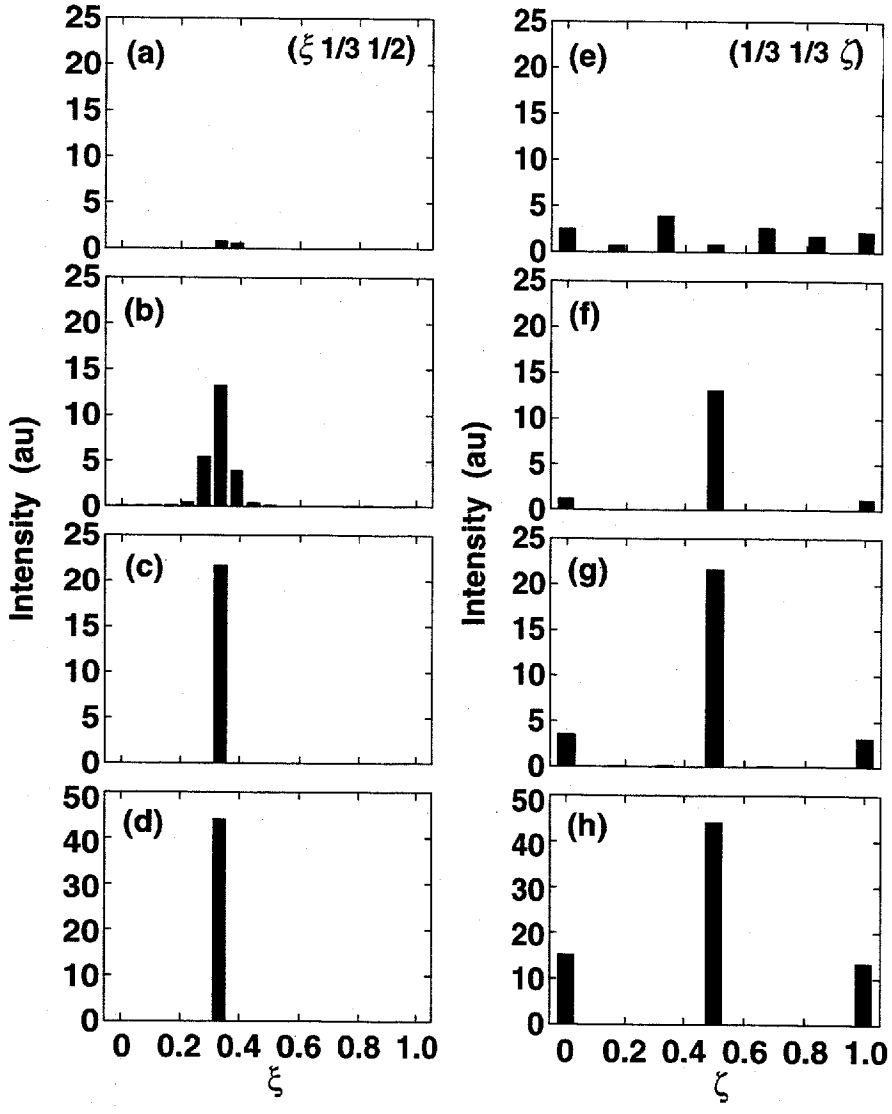


Fig. 3.13 X-ray diffraction intensities for $Fe_xTiS_2$ ($x = 0.333$) along ($\xi$ 1/3 1/2) [left side, (a)-(d)] and along (1/3 1/3 $\zeta$) [right side, (e)-(h)], calculated from four different atomic distributions with $V_{al}$ = -10,000 K (top row), the multiple interaction model (second row), the superlattice $\sqrt{3}a \times \sqrt{3}a \times 2c$ with fractional site occupancy (third row), and the ideal superlattice $\sqrt{3}a \times \sqrt{3}a \times 2c$ (bottom row).

## §3.5 Atomic distributions in stage-2 $Ag_{0.15}TiS_2$

According to the X-ray diffraction studies [58], the stage-2 $Ag_{0.15}TiS_2$ crystal undergoes a phase transition from ordered $\sqrt{3}a \times \sqrt{3}a \times 2c$ to disordered structure around 250-300 K. The formation of $\sqrt{3}a \times \sqrt{3}a$ structure itself is also realized in the $a$-axis planes of $Fe_xTiS_2$ ($x = 0.333$), as revealed by our MC calculations using four kinds of pair-interactions ($V_{a1}$, $V_{a2}$, $V_{c1}$, and $V_{2c}$) in the Hamoltonian [Eq. (9)]. With these parameters, however, only stage-1 structures in $G_xTiS_2$ with any concentrations $x$ are obtained, but not stage-2, along the $c$-axis direction.

In order to reproduce the stage-2 $G_{0.15}TiS_2$ with $\sqrt{3}a \times \sqrt{3}a$ structure, we have taken into account an additional term in the Hamiltonian, *repulsive* pair-interaction, $V_{c2}$, between the 2nd NN guest atoms in the nearest layers separated by $|a + c|$, which plays a crucial role to the atomic distributions in stage-2 $Ag_{0.15}TiS_2$, as described below. In addition, the phase transition occurring around 250-300 K suggests that these pair-interaction strengths may be much weaker than those for $Fe_xTiS_2$ ($x = 0.333$). With these in mind and by considering that the transition probability is given by $W = \exp(-\Delta H/T)$ [Eq. (4)], we have employed a set of weaker pair-interaction strengths for $Ag_{0.15}TiS_2$ as, $V_{a1} = -360$ K, $V_{a2} = +180$ K, $V_{c1} = -180$ K, and $V_{2c} = +180$ K, where the best-fit values obtained for $Fe_{0.333}TiS_2$ (Table I) are used but their magnitudes are reduced by about 1/30 with keeping the ratio $V_k/V_{a1}$ unchanged.

Figure 3.14 illustrates variation in the atomic distribution of $G_{0.15}TiS_2$ at $T = 200$ K with $V_{c2}$ (= 0 , -45, -90, and -180 K). In the case of $V_{c2} = 0$ K, the guest atoms distribute in every layer, forming the stage-1 structure with ~$\sqrt{3}a \times \sqrt{3}a$ arrangements, as expected. While for the repulsive interaction $V_{c2}$, the guest atoms are arranged having the in-plane $\sqrt{3}a \times \sqrt{3}a$ arrangements, which are stacked every two layers along the $c$-axis to form the stage-2 structure. Some domains of stage-2 structure are obtained for $V_{c2} = -45$ K, and the domain size becomes larger with increasing $|V_{c2}|$. These distributions are quite different from that for the stage-1 $Fe_{0.15}TiS_2$ with short-range order of $2a \times 2a \times 2c$ [Fig. 3.8(a)].

With increasing temperature, the guest atoms vary in the $a$-axis layers to destroy the in-plane $\sqrt{3}a \times \sqrt{3}a$ ordered states, as can be seen from the temperature variations in atomic distributions in the stage-2 $G_{0.15}TiS_2$ ($V_{c2} = -45$ K; Figs. 3.15) and stage-1 $G_{0.15}TiS_2$ ($V_{c2} = 0$ K; Figs. 3.16). The guest atom arrangements are changed from the in-plane $\sqrt{3}a \times \sqrt{3}a$ structures below 200 K to the disordered states above 250 K. Temperature dependence of the averaged numbers of neighboring atoms $z_k$ ($k$ = a1 and a2 in the $a$-axis planes, and $k$ = c1, c2, and 2c along the $c$-axis) for four different pair-interaction strengths $V_{c2}$ (= -180, -90, -45, and 0 K) are shown in Fig. 3.17. At $T = 100$ K the numbers $z_{a2}$ and $z_{2c}$, corresponding to attractive interactions $V_{a2}$ and $V_{2c}$, have rather large values, $z_{a2} = 4.2$ and $z_{2c} = 1.6$, but those to repulsive interactions $V_{a1}$ and $V_{c1}$ are small, $z_{a1} \sim 0$ and $z_{c1} \leq 0.2$. The value of $z_{c2}$ is strongly dependent on $V_{c2}$ from $z_{c2} = 2.9$ for $V_{c2} = 0$ K to $z_{c2} = 0.0$ for $V_{c2} = -180$ K. These results give us the reason why the stage-2 structure with nearly $\sqrt{3}a \times \sqrt{3}a \times 2c$ arrangement is formed by the interaction strengths used for our calculation; the repulsive interaction $V_{2c}$ is needed to satisfy the necessary condition for the stage-2 structure, $z_{c2} \sim 0$. With increasing temperature, the values of $z_{a2}$ and $z_{2c}$ decrease, while others increase, and they tend to approach the values of random distributions, $z_{a1} \sim z_{a2} \sim 6x = 0.9$, $z_{c1} \sim z_{c2} \sim 2x = 0.3$, and $z_{2c} \sim 12x = 1.8$. Here we should notice that the averaged number $z_{a2}$, which is strongly related to the in-plane $\sqrt{3}a \times \sqrt{3}a$ structure, decreases gradually with temperature, which

means that the number $z_{a2}$ is useful as an prospect of the in-plane ordered states but not enough to be an order parameter specifying the order-disorder transition of the $\sqrt{3}a \times \sqrt{3}a$ structure.

It should be emphasized that this is for the first time to construct such stage-2 structure only with pair-interactions between neighboring atoms, to our knowledge; some long-range interlayer and/or intralayer interactions are employed for the explanation of the stage-*n* structures in GIC [59, 66].

## §3.6 X-ray diffraction patters for $Ag_{0.15}TiS_2$

Now, we shall discuss more quantitatively the phase transition around 250-300 K in $Ag_{0.15}TiS_2$ from the X-ray scattering patterns calculated using the atomic distributions obtained by our MC simulations. Figure 3.18 shows the experimental results of (a) diffuse scattering patterns (called diffuse rod) in $Ag_{0.15}TiS_2$, parallel to the $c^*$-axis direction centered on (5/3 2/3 0) and (b) those of in-plane diffuse scattering along [1 1 0] direction at (5/3 2/3 1/2); the integrated intensity and full width at half maximum of the latter are plotted against temperature in Figs. 3.18(c) and (d), respectively. It is noted that the diffuse rod is very anisotropic elongated along the $c^*$-axis direction and it has small peaks at $\ell$ of half integers. The integrated intensity is decreased remarkably above 200 K with inflection point around 240 K, above which the width becomes broader. We have calculated the X-ray profiles along (5/3 2/3 $\ell$) using Eqs. (3) and (4), and the calculated atomic distributions at $T$ = 200 K in Fig.3.14; the results for $V_{c2}$ = -180 K, -90 K, -45 K, and 0 K are shown in Fig. 3.19. With increasing $|V_{c2}|$, the intensities at $\ell$ of integer increase, but those at $\ell$ of half-integer decrease oppositely. The calculated pattern with $V_{c2}$ = -45 K [Fig. 3.19(c)] is best agreement with the experimental profile for $Ag_{0.15}TiS_2$.

Temperature variations of diffuse scattering intensity profiles parallel to the $c^*$-axis direction centered on (5/3 2/3 0) are shown in Fig. 3.20(a). For $\ell$ of integers and half integers very sharp peaks appear at low temperatures, whose intensities take maximum values around 200 K, and decrease with increasing temperature, as shown in Fig. 3.20(b). The results along [1 1 0] direction at (5/3 2/3 1/2) are illustrated in Fig. 3.21; the calculated profiles are very sharp compared with those along the $c^*$-axis direction and its integrated intensity shows similar temperature dependence to that shown in Fig. 3.20(b). Thus, overall behavior of the diffuse rod observed in the stage-2 $Ag_{0.15}TiS_2$ are reproduced successfully using the atomic distributions in Fig. 3.15 simulated with the repulsive $V_{c2}$ = -45 K and other four pair-interactions.

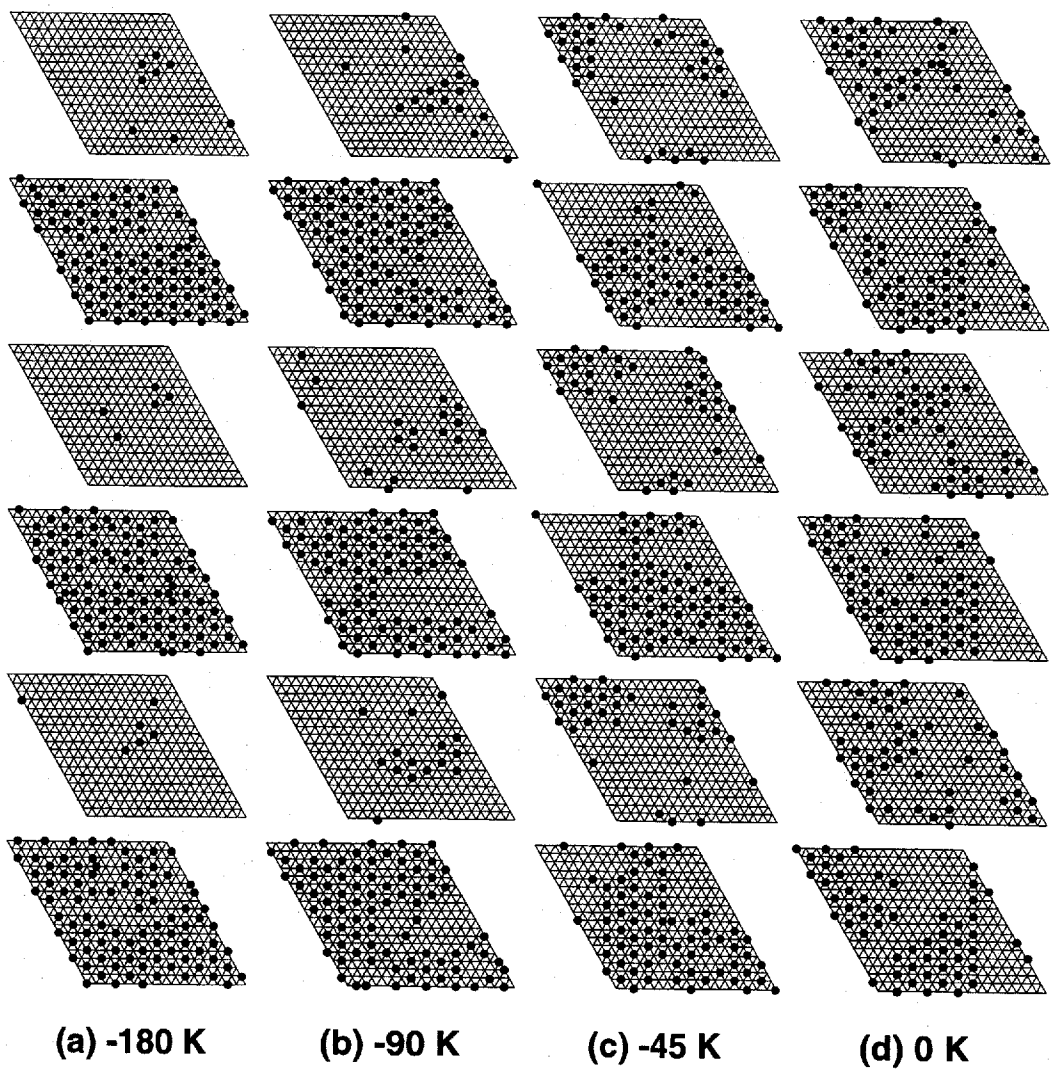


Fig. 3.14 Variation in atomic distribution of guest atoms for $G_{0.15}TiS_2$ at $T = 200$ K with pair-interaction strength $V_{c2}$, when the values of other pair- interactions are fixed to be $V_{a1} = -360$ K, $V_{a2} = +180$ K, $V_{c1} = -180$ K, and $V_{2c} = +180$ K.

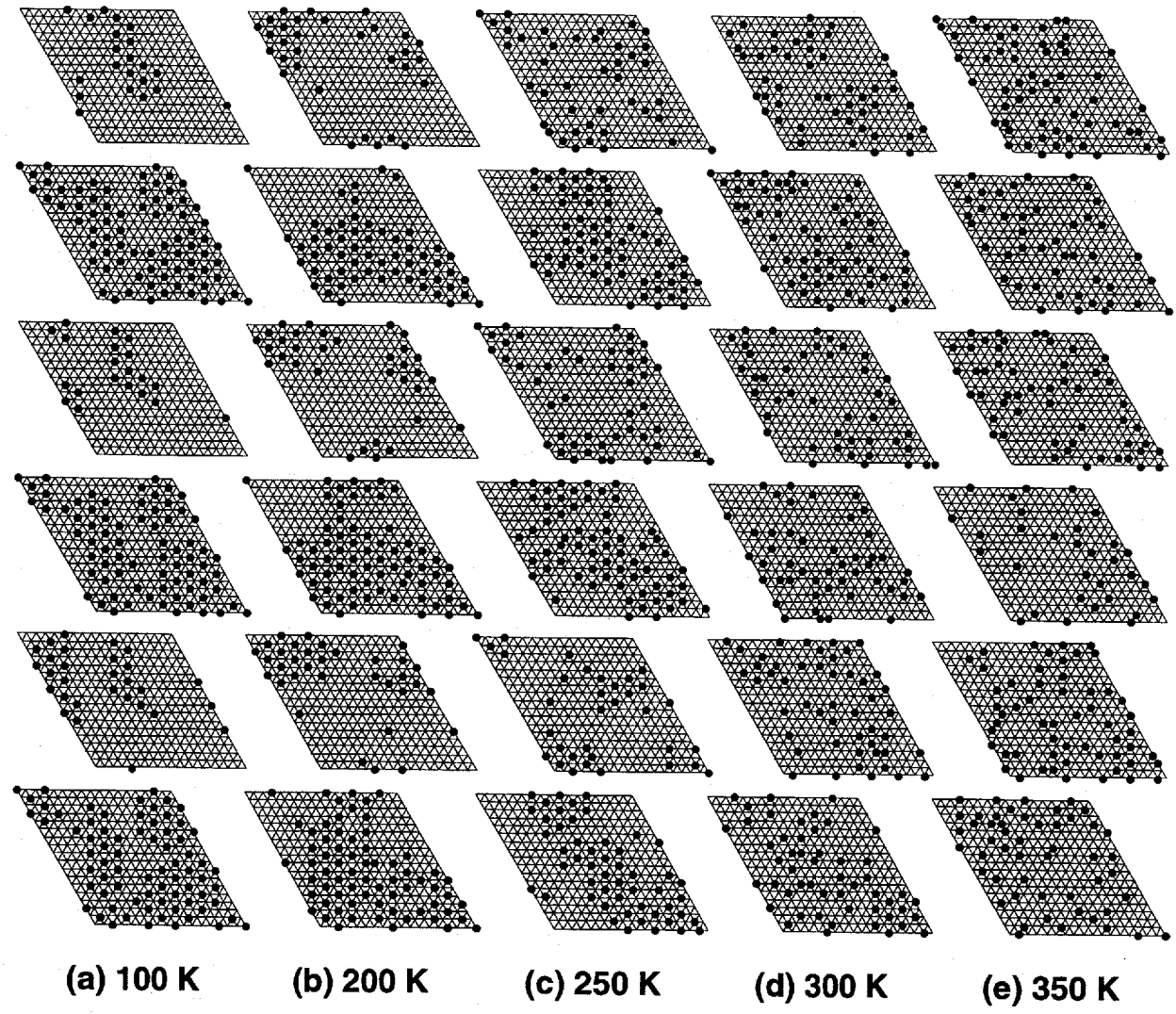


Fig. 3.15 The temperature variation in the atomic distributions of the guest atoms in the stage-2 $G_{0.15}TiS_2$ with $V_{c2}$ = -45 K shown in Fig. 3.14; these distributions can reproduce the observed X-ray patterns for $Ag_{0.15}TiS_2$.

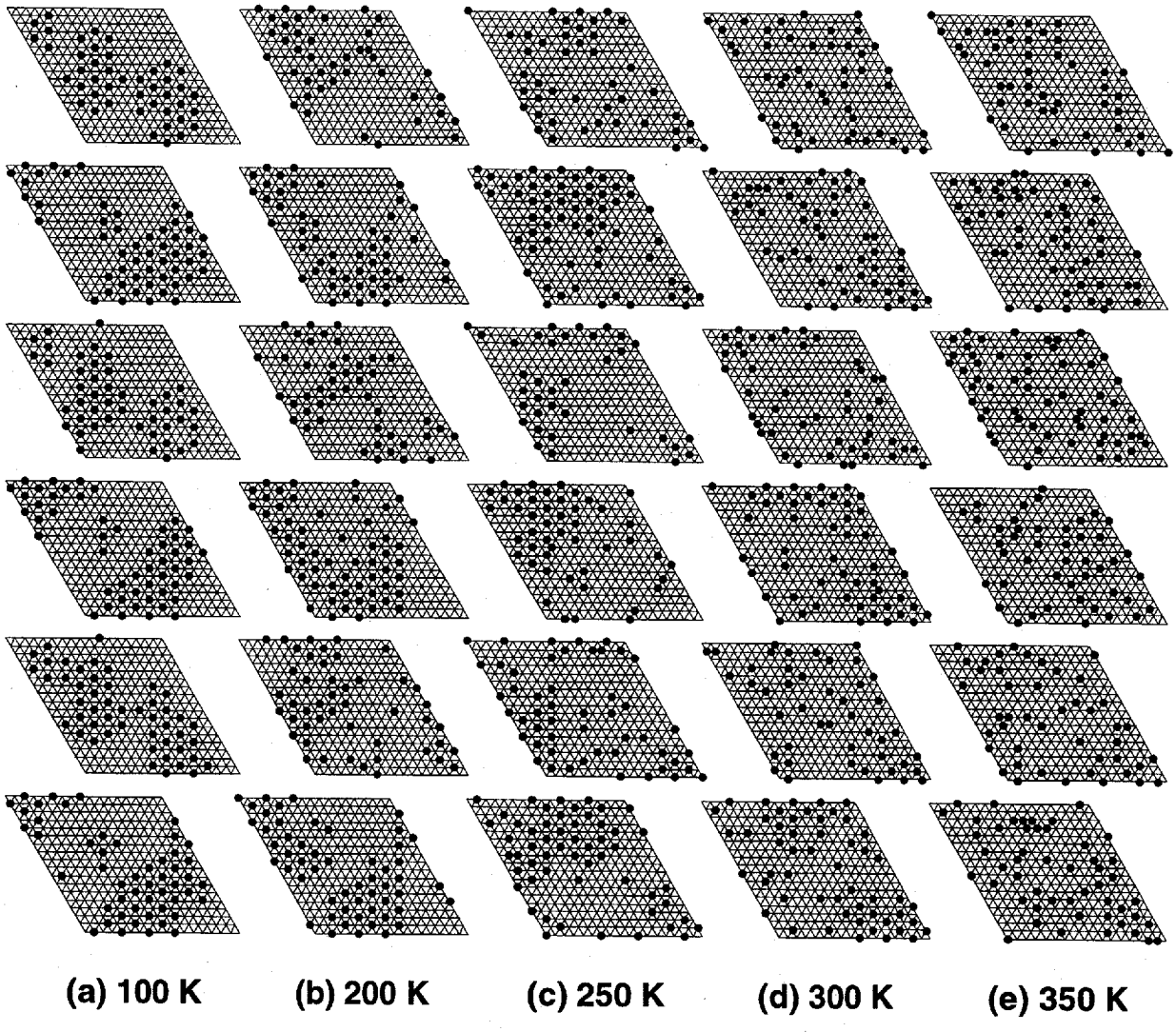


Fig. 3.16 The temperature variation in the atomic distributions of the guest atoms in the stage-1 $G_{0.15}TiS_2$ with $V_{c2}$ = 0 K shown in Fig. 3.14.

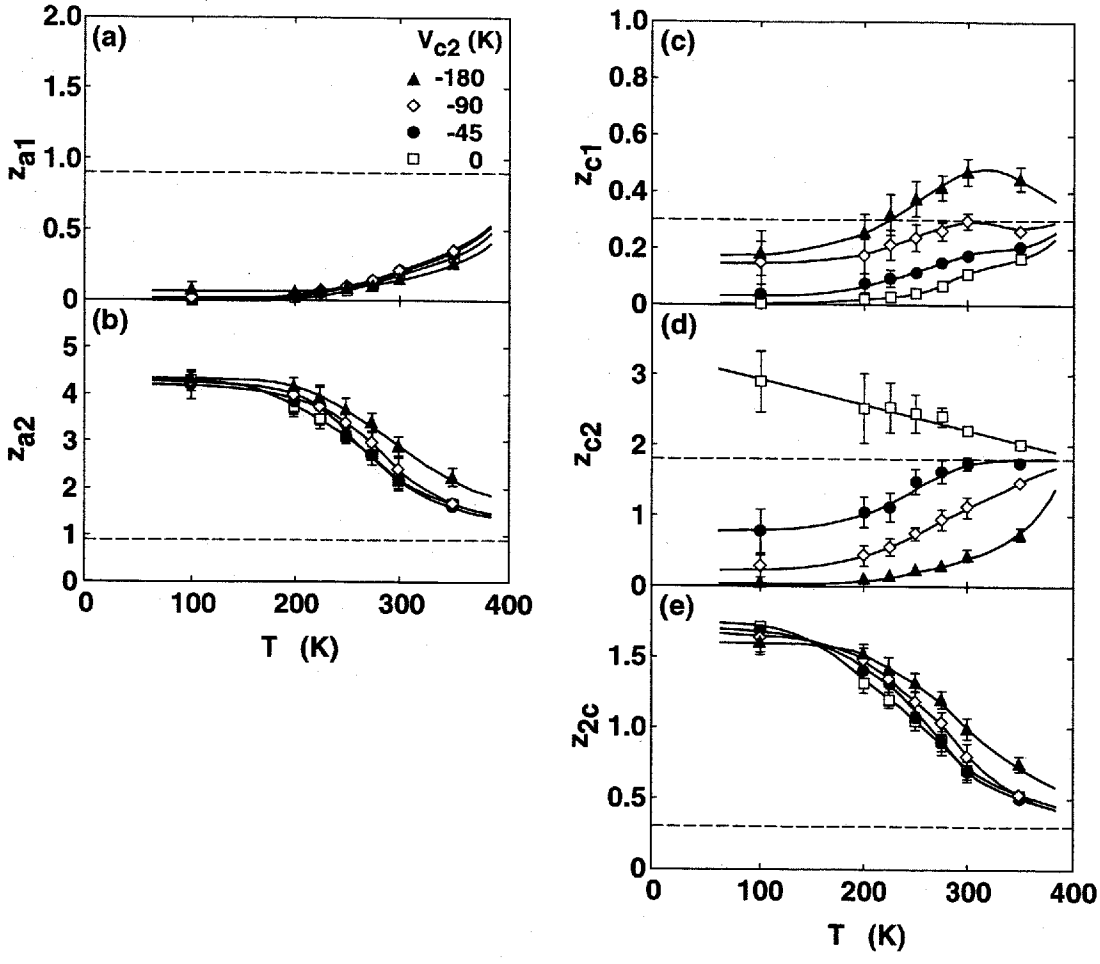


Fig. 3.17 The variation in the temperature dependence of $z_k$ ($k$ = a1, a2, c1, c2, and 2c) for $G_{0.15}TiS_2$ with four different $V_{c2}$.

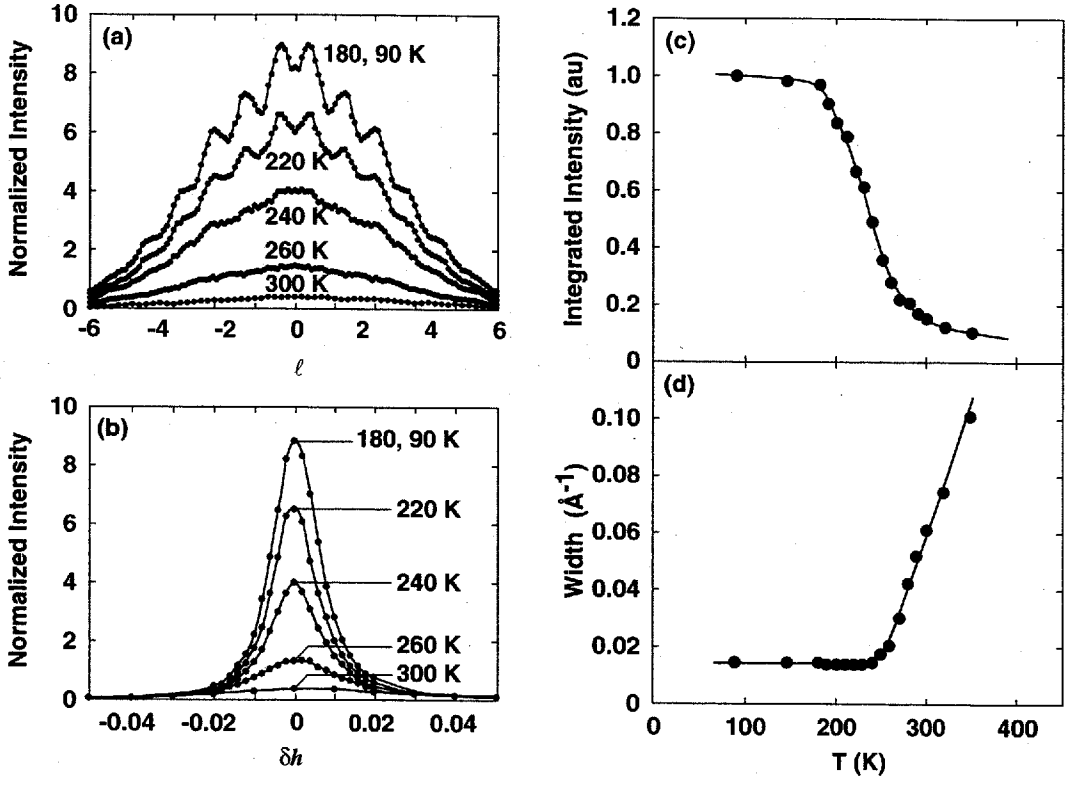


Fig. 3.18 (a) X-ray diffraction profiles of the diffuse rod observed for $Ag_{0.15}TiS_2$ pararell to the $c^*$-axis direction centered on (5/3 2/3 0) and (b) those of in-plane diffuse scattering along [1 1 0] direction at (5/3 2/3 1/2) at different temperatures [58]. Temperature dependence of (c) the integrated intensity and (d) the full width at half maximum of the in-plane diffuse scattering.

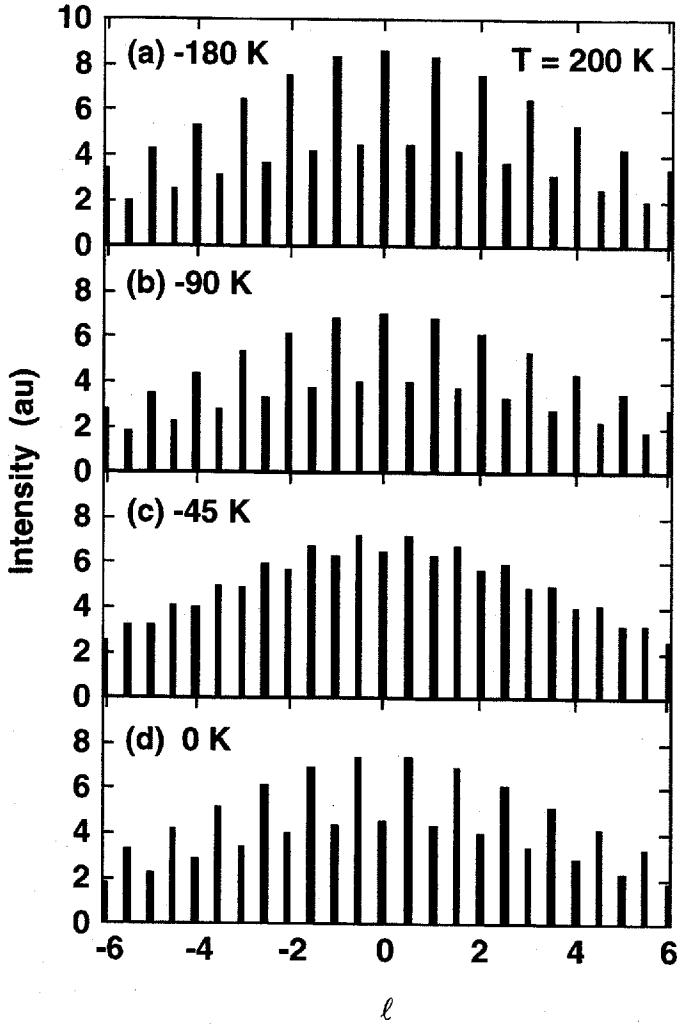


Fig. 3.19 Variation in X-ray diffraction profiles of the diffuse rod with $V_{c2}$ for $G_{0.15}TiS_2$ pararell to the $c^*$-axis direction centered on (5/3 2/3 0) at $T$ = 200 K. The result calculated with $V_{c2}$ = -45 K resembles well to the observed profiles for $Ag_{0.15}TiS_2$shown in Fig. 3.18.

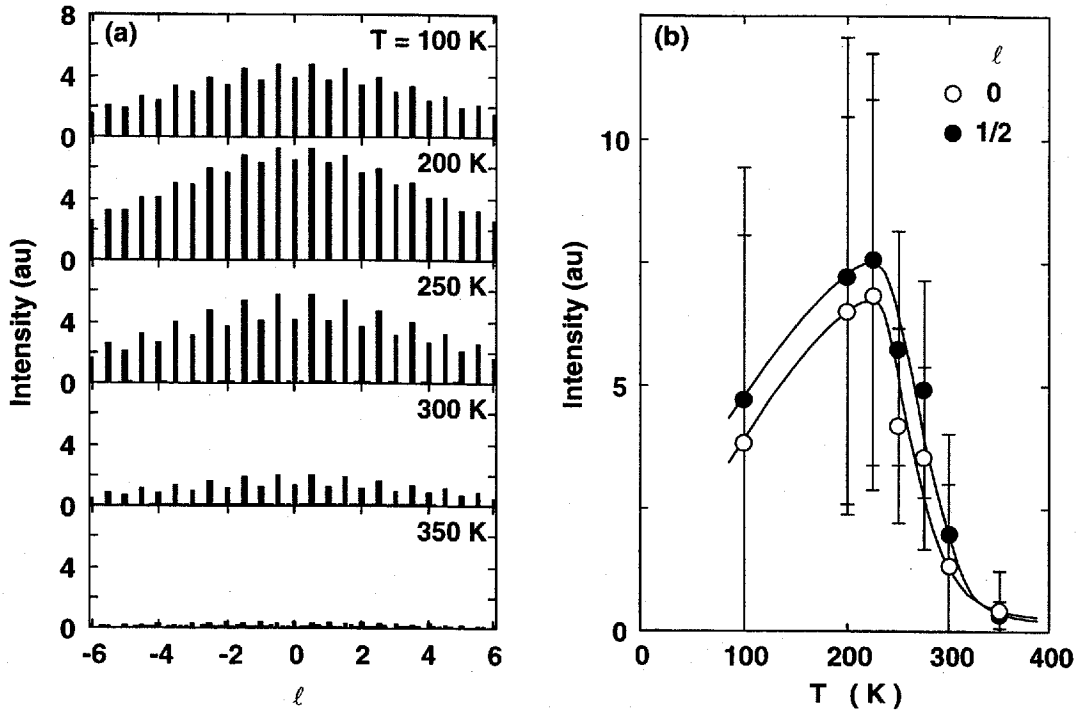


Fig. 3.20 (a) Temperature variation in X-ray diffraction profiles of the diffuse rod centered on (5/3 2/3 0) for $Ag_{0.15}TiS_2$ and (b) the values of the peak intensity at (5/3 2/3 0) and (5/3 2/3 1/2) plotted against temperature.

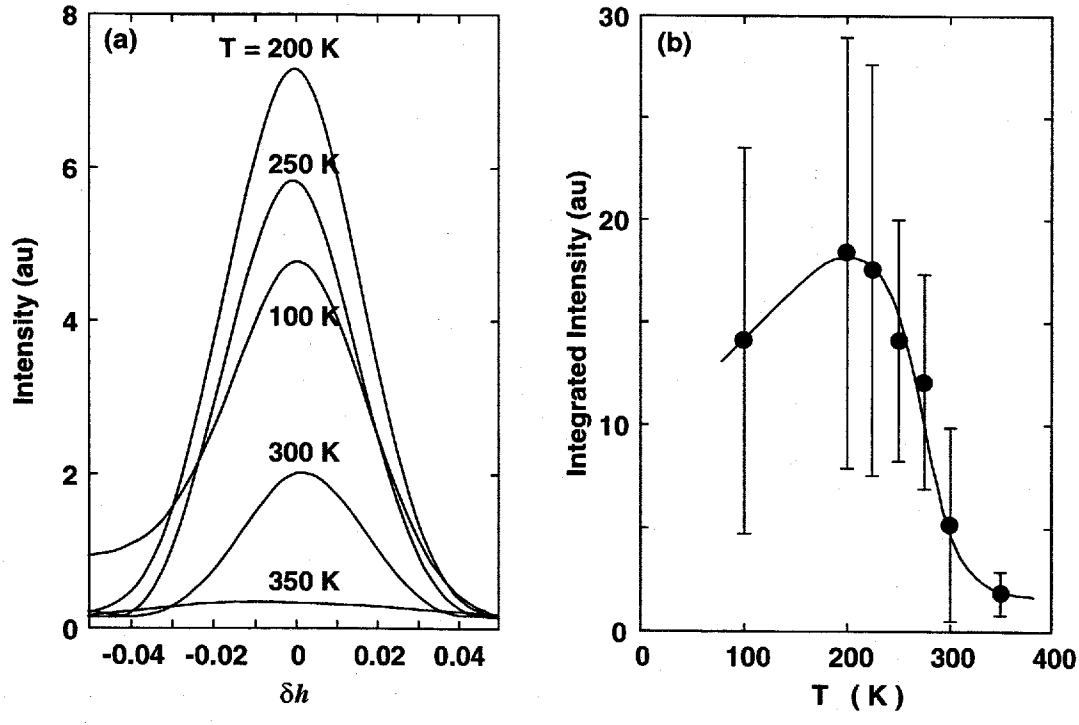


Fig. 3.21 (a) Temperature variation in X-ray diffraction profiles of the in-plane diffuse scattering along [1 1 0] direction at (5/3 2/3 1/2) for $Ag_{0.15}TiS_2$ and (b) the values of the integrated intensity plotted against temperature.

# Chapter 4

# Discussion

## §4.1 $Fe_xTiS_2$

### 4.1.1 Formation of clusters and percolation

We shall now discuss on the formation of *clusters* of the guest atoms in $Fe_xTiS_2$ in the *a*-axis plane and along the *c*-axis. Fig. 4.1 illustrates typical atomic distributions in the first layer ($m$ = 1) obtained with the multiple pair-interaction model for (a) $x$ = 0.15, (b) 0.25, and (c) 0.333, where Fe-occupied sites are marked by solid points. Solid lines (top row) mark the clusters that are formed by connecting the 1st NNs ($k$ = al), which we refer to as the a1-cluster for short. Since the number of $z_{a1}$ for $x$ = 0.15 is zero [Fig. 3.9(d)], there is no a1-cluster, while for $x$ = 0.25 and 0.333 very small al-clusters exist that are isolated each other. Similarly, the a2-clusters are formed by connecting the 1st and 2nd NNs ($k$ = al and a2) (middle row). The a2-clusters for $x$ = 0.15 and 0.25 are small, while those for $x$ = 0.333 are connected each other throughout the *a*-axis plane like a web pattern, forming so-called *a percolation cluster* [67]. As shown in the bottom row of Fig. 4.1, the a3-clusters formed by the 1st, 2nd, and 3rd NNs for $x$ = 0.15 are large, and those for $x$ = 0.25 and 0.333 extend to form a large percolation cluster having a web-like connection. Furthermore, it is noted that the dimension of the percolation cluster of the a3-cluster appearing in some layers for $x$ = 0.15 is one-dimensional (1D), while those of the a2- and a3-clusters for $x$ = 0.25 and 0.333 are two-dimensional (2D), as listed in Table II for three samples.

We here define a cluster size, $s_k$, as the number of the connected atoms in the $k$-cluster and a total number, $N(s_k)$, as the number of total guest atoms in its cluster of size $s_k$ within the sample lattice considered ($18 \times 18 \times 6$). Fig. 4.2 plots the total number $N(s_k)$ versus cluster size $s_k$ ($k$ = a1-a3) for (a) $x$ = 0.15, (b) 0.25, and (c) 0.333 — so-called *cluster-size distribution* —. For $x$ = 0.15, we get a large value of $N(s_k)$ with $s_{a1} = 1$ and $s_{a2} \leq 2$, which indicates that the a1- and a2-clusters are almost isolated, while the cluster-size distribution of the a3-cluster is broad ($s_{a3}$ = 1 - 48). For $x$ = 0.25, the cluster size is increased ($s_{a1} \leq 3$ and $s_{a2} \leq 10$), and the a2-cluster has a particularly broad distribution. In addition, for the a3-cluster we get $s_{a3}$ = 80, nearly equal to the total number of the guest atoms per layer, ~ $Nx/6$, which shows that the a3-cluster is formed by almost all intercalated guest atoms. For further intercalation ($x$ = 0.333), we have a little broad distribution with larger cluster size ($s_{a1} \leq 7$) for the a1-cluster and a single distribution with $s_{a2} \sim s_{a3} \sim 108$ (= $Nx/6$) for the a2- and a3-clusters.

Moreover, the c1- (top row), 2c- (second row), and c2-clusters (third row) for $Fe_xTiS_2$ with $x$ = 0.15, 0.25, and 0.333 are formed along the *c*-axis, as illustrated in Figs. 4.3(a), (b), and (c), respectively, where atomic distributions are depicted in the *ac*-plane. In all samples, there is no c1-cluster and the Fe atoms are completely isolated (top row), while the 2c-clusters form linear chains along the *c*-axis (second row), and thus these chains are 1D percolation clusters. In con-

trast, the c2-clusters have long-range zigzag chains for $x = 0.15$, linear chains with partially zigzag connection for $x = 0.25$, and wide web-like network for $x = 0.333$ (third row). In addition, the bottom row of Fig. 4.3 shows these c2-clusters projected on the $a$-axis plane ($m = 1$), where solid points indicate the Fe atoms in this layer and open circles those in the NN layers ($m = 2$ and 6, because of the periodic condition of the lattice). From these projected patterns, it is readily seen that the dimension of the percolation cluster of c2-cluster is 3D for all samples (Table II).

Figure 4.4 shows the cluster-size distributions of the c1- (top row), 2c- (middle row), and c2-clusters (bottom row) for (a) $x = 0.15$, (b) 0.25, and (c) 0.333. We see a large single peak at $s_{c1} = 1$, which indicates that the Fe atoms formed with the 1st NNs are completely isolated. The distributions for the 2c-clusters (middle row) are broad ($s_{2c} = 1$-3). On the other hand, the c2-clusters have large peaks at $s_{c2} \sim 250$, 460, and 650 for $x = 0.15$, 0.25, and 0.333, respectively, which are nearly equal to the total guest atoms $Nx$. Thus the cluster formation and the dimension of the percolation cluster are strongly dependent on the type and the number of neighboring guest atoms in both directions.

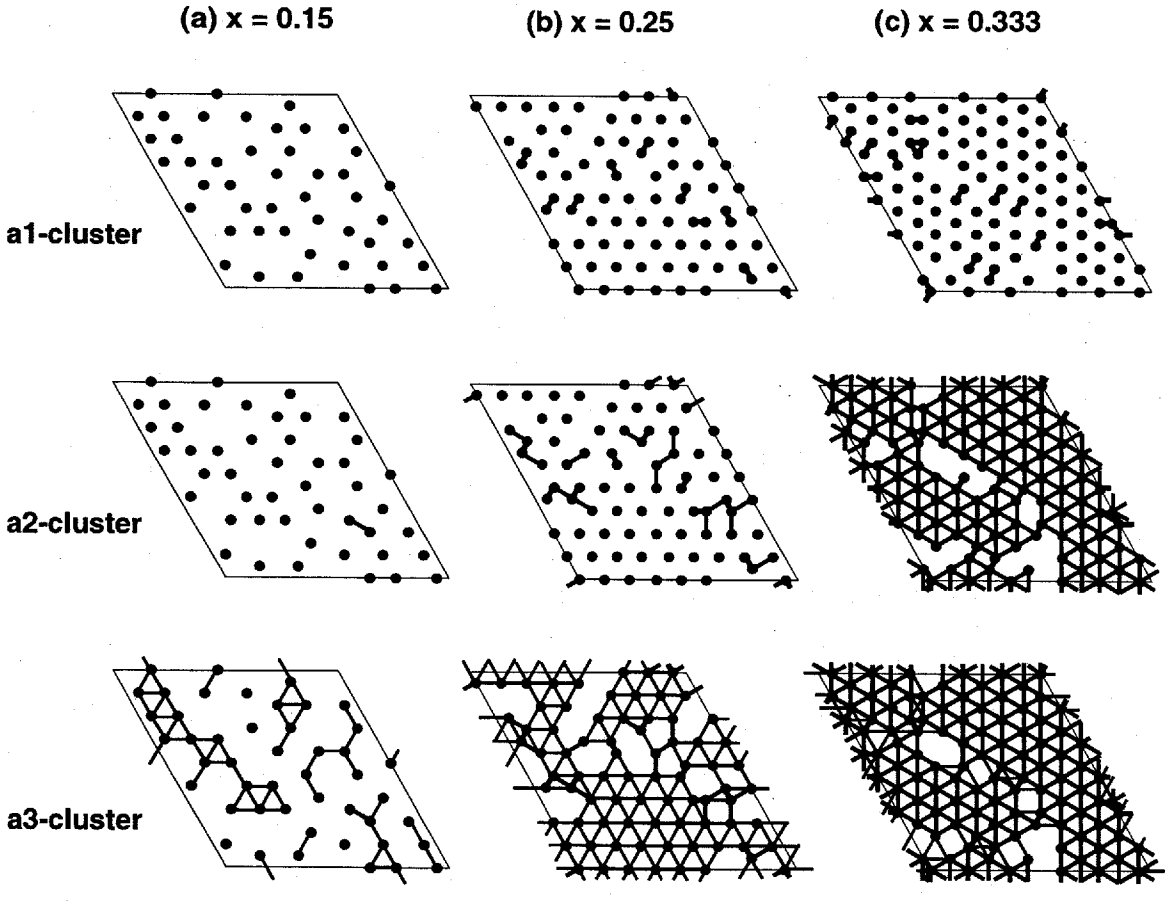


Fig. 4.1 Formation of the al- (top row), a2- (middle row), and a3-clusters (bottom row) in the $a$-axis plane ($m = 1$) for $Fe_xTiS_2$ with (a) $x = 0.15$, (b) $x = 0.25$, and (c) $x = 0.333$. Solid points mark the Fe atoms and solid lines clusters formed.

Table II Dimension of the percolation cluster of each $k$-cluster ($k$ = al, a2, a3, c1, 2c, and c2) formed in $Fe_xTiS_2$ ($x$ = 0.15, 0.25, and 0.333), obtained with the multiple pair-interaction model.

| $k$ | $x = 0.15$ | $x = 0.25$ | $x = 0.333$ |
|---|---|---|---|
| a1 | — | — | — |
| a2 | — | — | 2D |
| a3 | 1D | 2D | 2D |
| c1 | — | — | — |
| 2c | 1D | 1D | 1D |
| c2 | 3D | 3D | 3D |

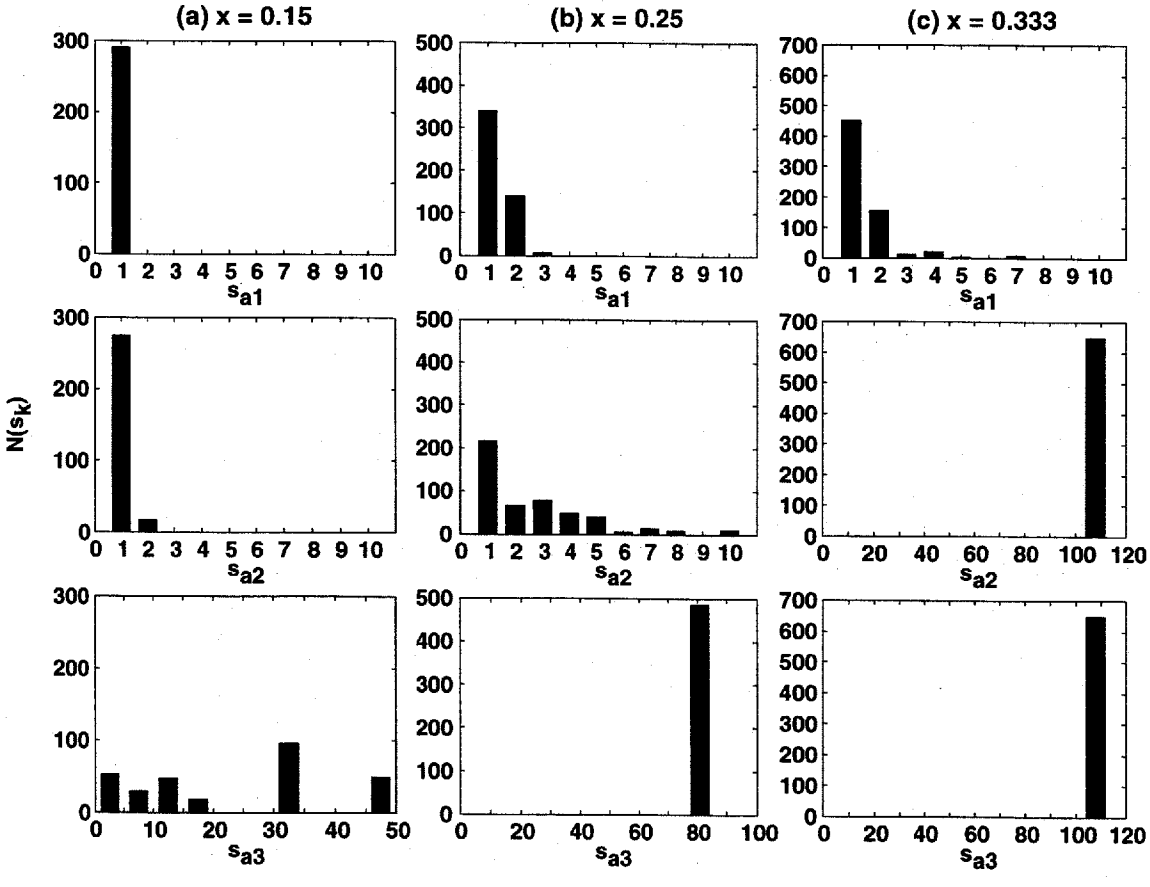


Fig. 4.2 Total number of the guest Fe atoms $N(s_k)$ in the $k$-cluster of size $s_k$ in the $a$-axis layer involved in the whole lattice site ($18 \times 18 \times 6$) for $Fe_xTiS_2$ with (a) $x = 0.15$, (b) $x = 0.25$, and (c) $x = 0.333$, plotted against the cluster size $s_k$ ($k$ = a1, a2, and a3).

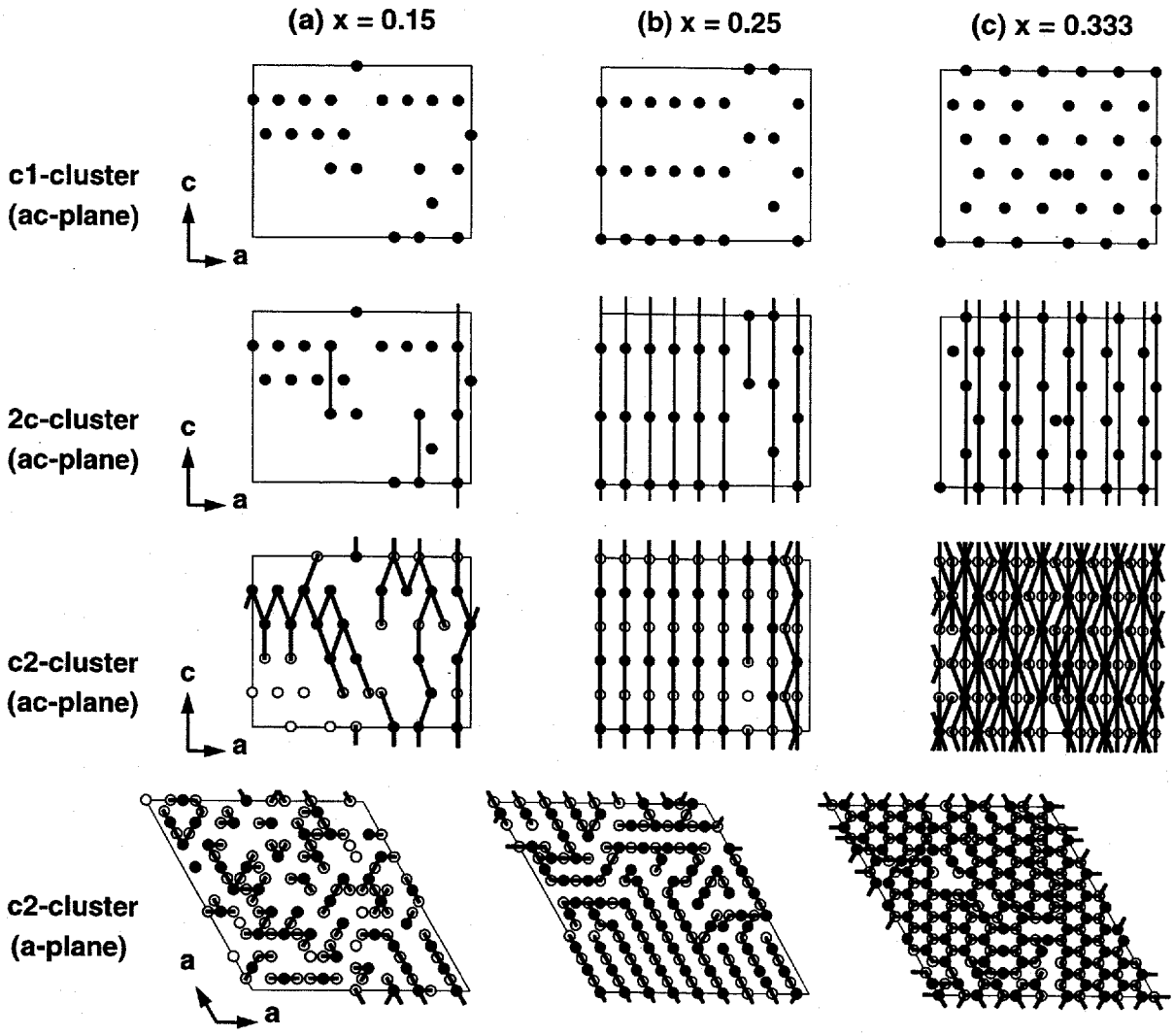


Fig. 4.3 Formation of the cl- (top row), 2c- (second row), and c2-clusters (third row) for $Fe_xTiS_2$ with (a) $x = 0.15$, (b) $x = 0.25$, and (c) $x = 0.333$. Solid points mark the Fe atoms in the *ac*-plane and solid lines the clusters formed. In the bottom row are shown the projections of the Fe atoms and clusters on the first *a*-axis plane ($m = 1$), where solid and open circles indicate the Fe atoms in the plane and in the next nearest planes, respectively.

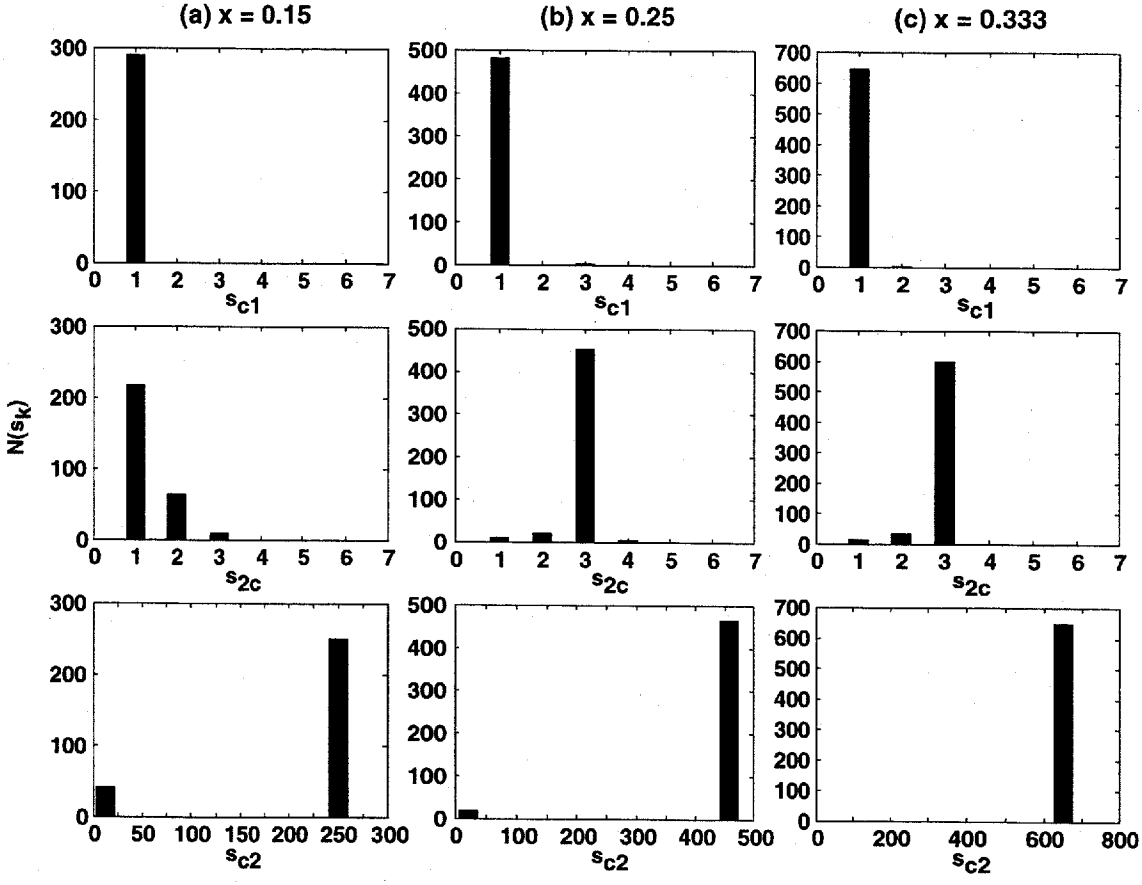


Fig. 4.4 Total number $N(s_k)$ of the guest Fe atoms within the $k$-cluster of size $s_k$ plotted against cluster size $s_k$ ($k$ = c1, 2c, and c2) formed along the $c$-axis for $Fe_xTiS_2$ with (a) $x = 0.15$, (b) $x = 0.25$, and (c) $x = 0.333$.

### 4.1.2 Magnetic properties

As described in Chapter 1, $Fe_xTiS_2$ shows SG ($0.01 \leq x \leq 0.20$), CG ($0.20 < x \leq 0.40$), and F ($0.40 < x \leq 1$) phases having a strong anisotropy with the easy axis along the $c$-axis. The positive Curie-Weiss temperature observed in the paramagnetic phase above the phase transition temperature [36] indicates the existence of strong ferromagnetic exchange interaction between the Fe spins in the $a$-axis plane and some weak but ferromagnetic exchange interaction between the Fe spins along the $c$-axis. In addition, we have found interesting behaviors in the relaxation phenomena of thermoremanent magnetization $M_r$ of the SG and CG phases. Some of these magnetic properties can be understood from the present results of computer simulations as follows:

(1) The ferromagnetic exchange interaction between the Fe atoms is considered as due to the 2nd and 3rd NN atoms in the $a$-axis layers, but not due to the 1st NNs, since $z_{a1} \sim 0$ for all samples ($x \leq 0.333$). (2) The observed CG phase is primarily stemmed from the web-like 2D percolation cluster formed for $x = 0.25$ and 0.333 in the $a$-axis plane (see Fig. 4.1). On the other hand, the SG phase ($x = 0.15$) has no 2D percolation cluster but its percolation cluster is one-dimensional. (3) In the relaxation behavior of $M_r$, we have found that the equilibrium relaxation spectra for $x = 0.333$ is much broader than those for $x = 0.25$ [44-46]. Such a difference is now attributable to the difference in the type of the percolation cluster, where 2D percolation cluster is formed by the 3rd NNs for $x = 0.25$ and by the 2nd NNs for $x = 0.333$. In the relaxation process of $M_r$, an Fe spin reverses gradually its direction after a magnetic field applied along the $c$-axis is switched off. In the present case, this process corresponds to the removal of some Fe atoms from a given atomic distribution. This in turns means that the percolation cluster for $x = 0.25$ is destroyed into some smaller clusters which no longer percolate over the $a$-axis plane. But the 3D percolation cluster for $x = 0.333$ may not be destroyed, because in this case it is formed with the 2nd NNs. (4) Since the c2-cluster is a 3D percolation cluster for $x = 0.15$-$0.333$, the exchange interaction between the c2-cluster along the $c$-axis may be much weaker that those between the 2nd and 3rd NNs in $a$-axis plane.

For further quantitative discussion on the magnetic properties in SG and CG phases, especially on their spin dynamics, simulations taking into account the exchange interactions between the $k$-th neighboring Fe atom ($k$ = a2, a3, c2, and 2c) will be needed.

### 4.1.3 Local structures

EXAFS studies of $M_xTiS_2$ [11,12] have revealed that the interatomic distance between the guest atoms $M$ and host sulfur atoms S, $R(M\text{-S})$, depends strongly on the kind of $M$ but not on its concentration $x$, while the Ti-S distance, $R$(Ti-S), increases with $x$ (Fig. 4.5). Such changes in the local structures are in qualitative agreement with the concentration dependence of the lattice parameters $a$ and $c$ of $M_xTiS_2$ (Fig. 4.6) [8]. More detailed discussion has been done by considering that the S atoms change their position [$A(n)$, $H(n)$] depending on the number of the surrounding guest atoms, $n$ (integer), as shown in Fig. 4.7, using a random guest atom distribution [12]. In the present work, we shall give further discussion on these local structures based on our calculated atomic distributions in $M_xTiS_2$.

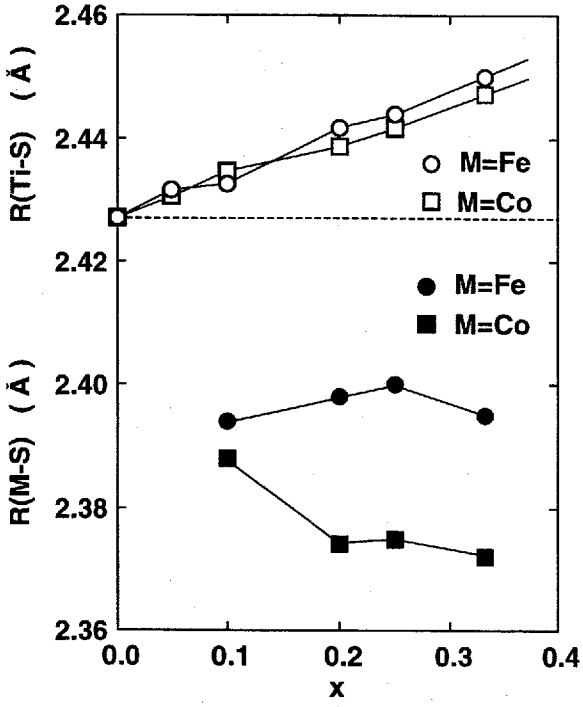


Fig. 4.5 Interatomic distances (a) $R(M\text{-S})$ and (b) $R(\text{Ti-S})$ obtained from $M$ and Ti K-edges EXAFS experiments for $M_x TiS_2$ ($M$ = Fe and Co) plotted against the guest concentration $x$ [11,12].

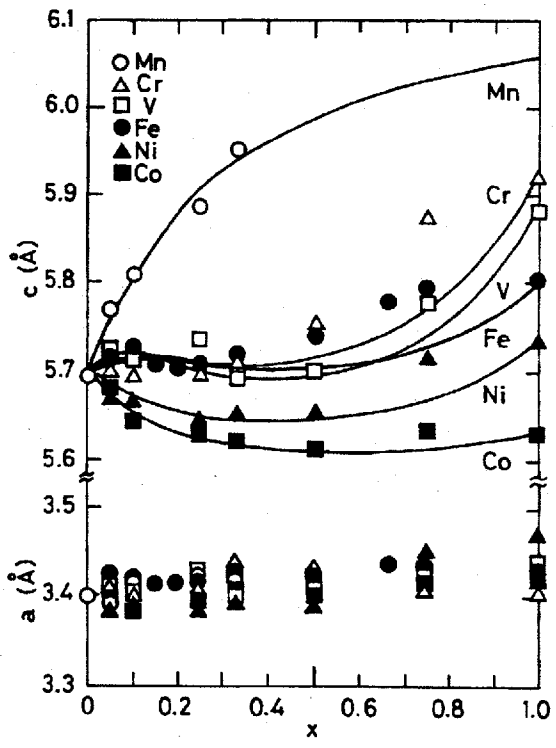


Fig. 4.6 Lattice parameters $a$ and $c$ plotted against the guest concentration $x$ for $M_x TiS_2$ ($M$ = V, Cr, Mn, Fe, Co, and Ni) [8].

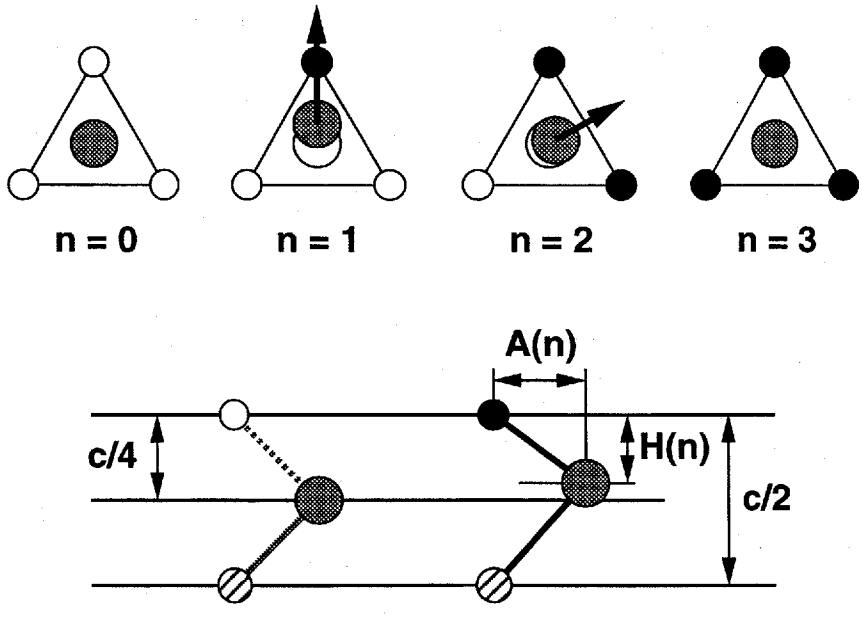


Fig. 4.7 Schematic top view for the displacement of the host S atom (large circle) according to the number of the surrounded guest atoms (solid circles), $n$ (= 0, 1, 2, and 3) for $M_xTiS_2$; open small circle indicates unoccupied site. Corresponding cross-section for the position of the S atom, [$A(n)$, $H(n)$] from guest atom; the S atoms with no surrounded guest atom ($n$ = 0) are assumed to be at $H(n)$ = $c/4$.

As a typical result, Figure 4.8 illustrates the atomic distribution of the guest Fe atoms calculated with the multiple pair-interaction model [solid circles; bottom row of Fig. 3.8(b)] and of the host S atoms in the first layer ($m$ = 1) for $Fe_xTiS_2$ ($x$ = 0.25). The S atoms with the number of its nearest Fe atoms, $n$ = 0, 1, and 2 are marked by open circles, hatched circles, and open squares, respectively. In this case, there is no S atom with $n$ = 3. For numerical treatment of these atomic distribution, we here introduce the probability that one host S atom has $n$ nearest guest atoms, which we express as,

$$p(n) = N(n)/N_S, \tag{10}$$

where $N(n)$ is the total number of the S atoms associated with the $n$ nearest Fe atoms and $N_S$ (= 18 × 18 × 6 × 2 = 3888) the total number of the S atoms in the whole lattice.

In Fig. 4.9 are shown the calculated values of $p(n)$ plotted against $n$ for all samples ($x$ = 0.15, 0.25, and 0.333) obtained from various atomic distributions (Figs. 3.1-3.3, and 3.8). We should note that the $p(n)$-$n$ plot obtained by the multiple pair-interaction model for each sample is nearly similar to those obtained with the repulsive interaction ($V_{a1}$ = -10,000 K). This result is in good agreement with the fact that the averaged number of the 1st NN guest atoms $z_{a1}$ is nearly zero ($z_{a1}$ ~ 0), which arises from the strong repulsive pair-interaction $V_{a1}$ in the $a$-axis plane, as mentioned above (Fig. 3.10). Using the probability $p(n)$ obtained with the multiple pair-interaction model and random distribution, and the observed lattice constants $a$ and $c$ [Fig. 4.6], we have evaluated the Ti-S distance $R$(Ti-S), or the change in the local structure near the S atoms. For simplicity, we assume that the host Ti atoms array regularly with the periodicity of the lattice spacings $a$ and $c$, and express the S position as, [$A(n)$, $H(n)$], from the guest atom $M$ in the plane

including the direction of $M$-S-Ti bondings. Based on this model, we obtain the relations, $A(3) = \sqrt{3}a/3$, $H(0) = c/4$, and $A^2(n) + H^2(n) = R^2(M\text{-S})$ for $n$ = 1, 2, and 3; therefore, $H(3) = [R^2(M\text{-S}) - a^2/3]^{1/2}$. In addition, the displacement $H(n)$ of the S atom from $H(0)$ to $H(3)$ is not always linear to $n$, since the strength of the bonding between the guest $M$ and S atoms is often much stronger than that between the vacant site and S atoms. In facts, semiempirical analysis of the guest concentration dependence of the interlayer spacing $c$ based on the concept of "resonance" in chemical bonding, have revealed that the force constant for the $M$-S bond is larger than that for the vacancy-S bond in the van der Waals gap in $M_xTiS_2$ [8]. Therefore, we assume a nonlinear dependence of $H(n)$ on $n$ as,

$$H(n) = H(0) + [H(3) - H(0)]\,(n/3)\,\{(1+\delta)/[1+\delta(n/3)]\}. \tag{11}$$

Here $\delta$ is a parameter to specify a nonlinear dependence of $H(n)$ on the number $n$; for $\delta = 0$ $H(n)$ changes from $H(0)$ to $H(3)$ linearly, while for a positive $\delta$ it does concavely with $n$ when $H(3) < H(0)$, and oppositely for a negative $\delta$. Then, $R$(Ti-S) can be written as,

$$R(\text{Ti-S}) = \sum_n p(n)\, R_n(\text{Ti-S}), \tag{12}$$

where $p(n)$ is the probability obtained above and $R_n$(Ti-S) is the interatomic distance for $n$, which is given by

$$R_n(\text{Ti-S}) = (n/3)\{A^2(n) + [(c/2) - H(n)]^2\}^{1/2} + (1 - n/3)\{B^2(n) + [(c/2) - H(n)]^2\}^{1/2}, \tag{13}$$

using $B(0) = \sqrt{3}a/3$, $B(1) = \{(a/2)^2 + [(\sqrt{3}a/2) - A(1)]^2\}^{1/2}$, and $B(2) = (\sqrt{3}a/2) - [A^2(2) - (a/2)^2]^{1/2}$. The first term in Eq. (13) is for the Ti atoms above or below the guest atoms and the second term for those around the unoccupied sites. The best-fit values of $\delta$, $A(n)$, and $H(n)$, are listed in Table III for two samples ($x$ = 0.25 and 0.333). We see that the nonlinear parameter $\delta$ is very small (-0.02 for $x$ = 0.25 and -0.15 for $x$ = 0.333), which means that the change in the S atom position along the $c$-axis is almost linear to the number of the nearest Fe atoms $n$ [Fig. 4.10(a) and (b])]. In addition, with increasing $n$, $A(n)$ is almost unchanged but $H(n)$ is reduced. However, no clear difference in the values of $A(n)$ and $H(n)$ are seen among these samples, regardless of the type of the distributions used.

Similar calculations for other intercalation compounds $M_xTiS_2$ have been made in the same way as done above. The best-fit values for $Co_xTiS_2$ are summarized in Table IV, where the probability of $Fe_xTiS_2$ is used, since much less is known about the structural studies of this compound to our knowledge. We have found that among others $Co_xTiS_2$ has the largest value of $\delta$; $\delta$ = 3.8 for $x$ = 0.25 and 2.2 for $x$ = 0.333 (multiple pair-interaction model) and 9.8 for $x$ = 0.25 and 6.3 for $x$ = 0.333 (random distribution). Thus, we have clarified that atomic distribution of the guest atoms around their host S atoms play a crucial role on the local structures in the intercalation compounds. Such large values of $\delta$ for Co guest atoms means that the host S atoms can be shifted easily along the $c$-axis by even one Co atom [Fig. 4.10(c) and (d)], which may be due to a very strong bonding between Co and S atoms. From these analyses, variations in the local structure for $Fe_xTiS_2$ and $Co_xTiS_2$ are illustrated schematically in the (1 1 0) cross-sections of Fig. 4.11(a) and

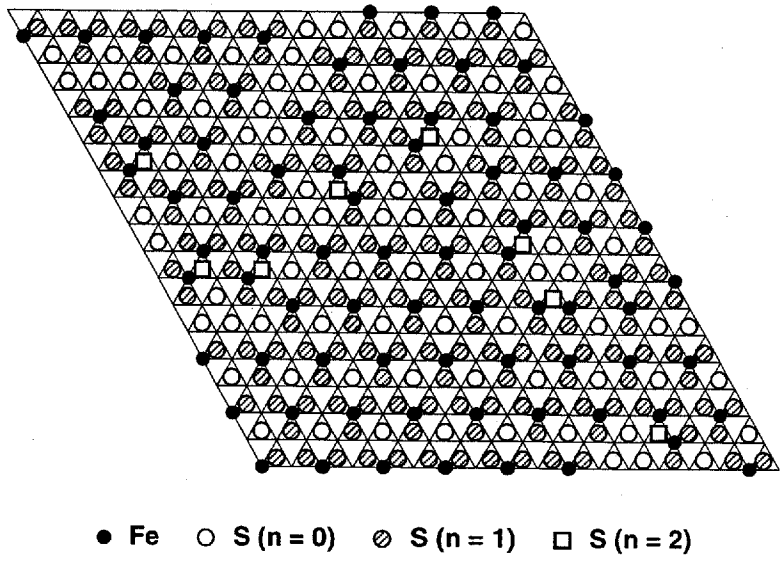


Fig. 4.8 Atomic distribution of the host S atoms with $n$ nearest Fe guest atoms (solid circles) in the $a$-axis layer ($m$ = 1) for $Fe_xTiS_2$ ($x$ = 0.25), calculated with the multiple pair-interaction model. Open circles, hatched circles, and open squares mark the host S atoms with the number of its nearest Fe atoms, $n$ = 0, 1, and 2, respectively.

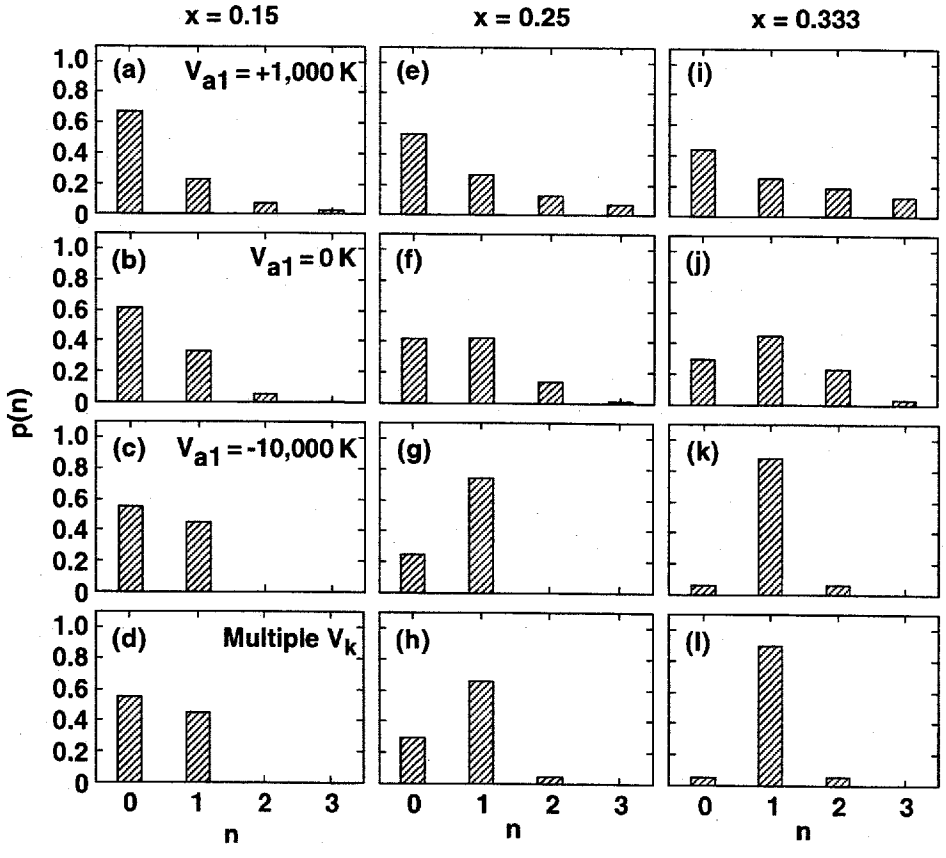


Fig. 4.9 Probability $p(n)$ defined by Eq. (10) plotted against the number of nearest Fe atoms around the host S atoms for different atomic distributions in $Fe_xTiS_2$ with $x$ = 0.15 (left column), $x$ = 0.25 (center column), and $x$ = 0.333 (right column), calculated with $V_{a1}$ = +1,000 K (top row), $V_{a1}$ = 0 K (second row), $V_{a1}$ = -10,000 K (third row), and the multiple pair-interaction model (bottom row).

Table III Best-fit values of nonlinear parameter $\delta$, probability $p(n)$, and positions $A(n)$ and $H(n)$ (in units of Å) of the host S atom with $n$ nearest guest Fe atoms in $Fe_xTiS_2$ ($x = 0.25$ and 0.333), obtained from the atomic distribution with the multiple pair-interaction model and random distribution.

| | Multiple pair-interaction | | | Random distribution | | |
|---|---|---|---|---|---|---|
| $n$ | $p(n)$ | $A(n)$ | $H(n)$ | $p(n)$ | $A(n)$ | $H(n)$ |
| $x = 0.25$ | | $\delta = -0.022$ | | | $\delta = -0.028$ | |
| 0 | 0.295 | — | 1.428 | 0.422 | — | 1.428 |
| 1 | 0.660 | 1.943 | 1.407 | 0.422 | 1.943 | 1.407 |
| 2 | 0.045 | 1.959 | 1.385 | 0.141 | 1.959 | 1.385 |
| 3 | 0.000 | 1.974 | 1.363 | 0.016 | 1.974 | 1.363 |
| $x = 0.333$ | | $\delta = -0.15$ | | | $\delta = -0.20$ | |
| 0 | 0.050 | — | 1.429 | 0.297 | — | 1.429 |
| 1 | 0.900 | 1.940 | 1.406 | 0.444 | 1.940 | 1.407 |
| 2 | 0.050 | 1.958 | 1.381 | 0.222 | 1.957 | 1.382 |
| 3 | 0.000 | 1.977 | 1.353 | 0.0370 | 1.977 | 1.353 |

(b), respectively. In $Fe_xTiS_2$ the contraction due to S-Fe-S bonding and the expansion of the host layer, which caused mainly due to charge transfer from Fe atom to Ti atom, compensate each other and the interlayer spacing $c$ is less changed upon intercalation, while in $Co_xTiS_2$ the contraction due to S-Co-S bonding overcomes the expansion of the host layer, leading to the contraction of the interlayer spacing $c$ (Fig. 4.6).

Furthermore, the difference in $\delta$ between $Fe_xTiS_2$ and $Co_xTiS_2$ is attributable to the difference in the bond nature between the guest atom and the surrounding S atoms or Ti atoms. As pointed out by N. Suzuki *et al.* [40], in $M_xTiS_2$ ($M$ = Mn, Fe, Co, and Ni; $x$ = 1/3 and 1) the $M$ 3d$\gamma$ states are hybridized strongly with S 3p states, and the bond order between them is large and plays a dominant role in the chemical bondings, leading to a large value of $\delta$. In $Fe_xTiS_2$, however, the Fe 3d$\varepsilon$ states are also hybridized strongly with Ti 3d$\varepsilon$ states, and the bond order of Fe 3d$\varepsilon$-Ti 3d$\varepsilon$ bonding along the $c$-axis direction is fairly large comparable to that of Fe 3d$\gamma$-S 3p bonding, which may be the main reason why the parameter $\delta$ specifying the nonlinearlity in the Fe-S bonding along the $c$-direction is very small in the Fe intercalates.

Table IV Best-fit values of nonlinear parameter $\delta$, and positions $A(n)$ and $H(n)$ (in units of Å) of the host S atoms with $n$ nearest guest Co atoms in $Co_xTiS_2$ ($x$ = 0.25 and 0.333), obtained from the atomic distribution with the multiple pair-interaction model and random distribution, where the probability $p(n)$ for $Fe_xTiS_2$ (Table V) is used.

| | Multiple pair-interaction | | Random distribution | |
|---|---|---|---|---|
| $n$ | $A(n)$ | $H(n)$ | $A(n)$ | $H(n)$ |
| $x$ = 0.25 | $\delta$ = 3.8 | | $\delta$ = 9.8 | |
| 0 | — | 1.410 | — | 1.410 |
| 1 | 1.950 | 1.352 | 1.958 | 1.341 |
| 2 | 1.961 | 1.336 | 1.964 | 1.332 |
| 3 | 1.967 | 1.328 | 1.967 | 1.328 |
| $x$ = 0.333 | $\delta$ = 2.2 | | $\delta$ = 6.3 | |
| 0 | — | 1.410 | — | 1.410 |
| 1 | 1.944 | 1.358 | 1.954 | 1.343 |
| 2 | 1.959 | 1.336 | 1.963 | 1.330 |
| 3 | 1.967 | 1.325 | 1.967 | 1.325 |

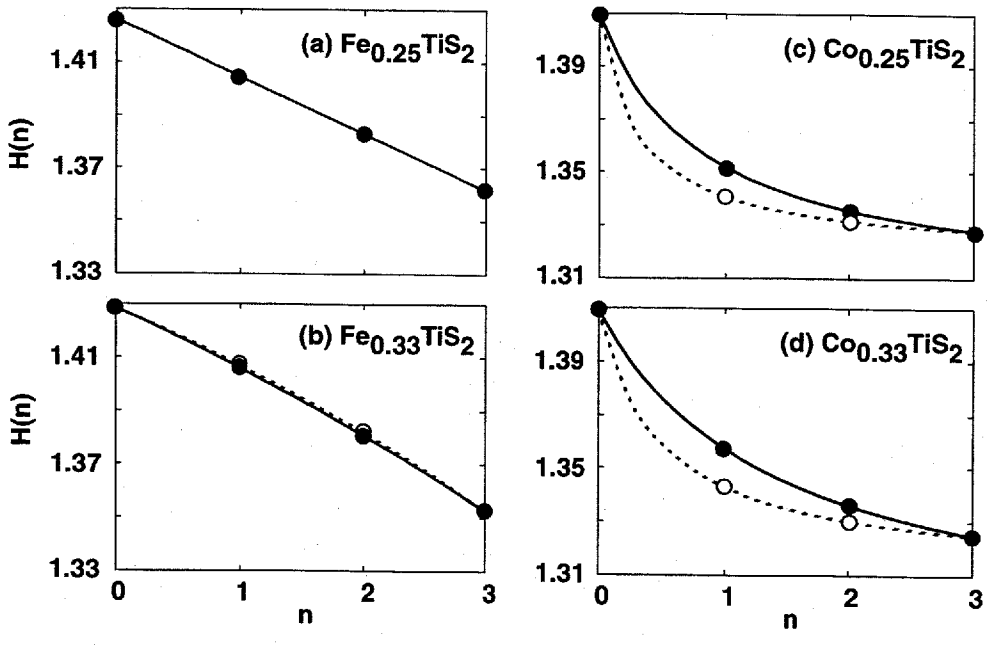


Fig. 4.10 Variation in the displacement $H(n)$ of the S atoms along the $c$-axis direction with $n$ nearest guest atoms for (a) $Fe_{0.25}TiS_2$, (b) $Fe_{0.33}TiS_2$, (c) $Co_{0.25}TiS_2$, and (d) $Co_{0.33}TiS_2$. Solid and open circles shows the values obtained from the atomic distribution with the multiple pair-interaction model and those from random distribution, respectively.

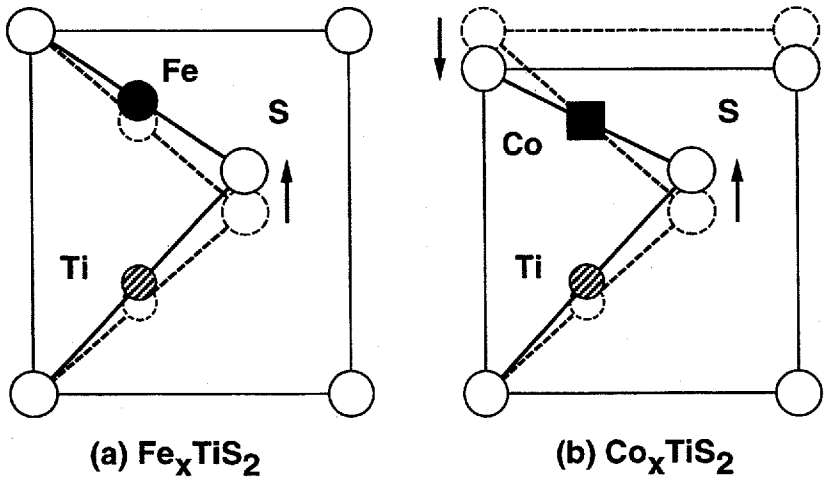


Fig. 4.11 Schematic (1 1 0) cross-section for the variation in the local structure in (a) $Fe_xTiS_2$ and (b) $Co_xTiS_2$ upon intercalation of the guest atoms.

## §4.2 Phase transition in $Ag_{0.15}TiS_2$

Now we shall discuss phase transition in stage-2 $Ag_{0.15}TiS_2$. As described above, the atomic distribution in $Ag_{0.15}TiS_2$ shows in-plane $\sqrt{3}a \times \sqrt{3}a$ structure at low temperatures, and the ordered structure is destroyed with raising temperature [Fig. 3.15]. This order-disorder transition occurs due to the small values of pair-interactions $V_k$ of the order of 100 K in the present simulation. Here, we should point out two experimental evidence, thermal displacement of the host and guest atoms in-plane and along the $c$-axis determined by X-ray analysis [51,53], and entropy of phase transition evaluated from the specific heat measurements [56,57].

The $c$-axis length for one silver layer in stage-2 $Ag_{0.15}TiS_2$ has a spacing elongation of 0.71Å compared with the van der Waals gap of the host $TiS_2$, as illustrated in Fig. 1.5 [51]. Furthermore, temperature factors of the constituent Ti and S atoms and guest Ag atom, $B_{Ti}$, $B_S$, and $B_{Ag}$, for $TiS_2$ and $Ag_{0.15}TiS_2$ are listed in Table V, as well as their mean square thermal displacements, $\mu_{th,A}$, evaluated using the relation $B_A = 8\pi^2\mu_{th,A}^2$ for atom $A$ (= Ti, S, and Ag). From these results, we can see that upon intercalation of Ag atoms, vibrational amplitude of Ti atoms becomes larger both in-plane and along the $c$-axis, while that of S atoms is almost unchanged, which means that the expansion of the host layers leads to the large vibration of Ti atoms. Furthermore, it is noted that the value of $B_{Ag}$ is very large, especially in the $a$-axis planes ($B_{Ag} = 3.0$ Å$^2 >> B_{Ti}, B_S$). This fact also supports that the pair-interactions between the neighboring Ag atoms are rather weak, and the in-plane arrangements of the Ag atoms are easily destroyed by the thermal fluctuation of the order of 300 K into disordered states, as shown in Fig. 3.15.

Specific heat measurements for $Ag_xTiS_2$ ($0.09 \le x \le 0.34$) [56,57] confirmed that the transition temperature is about 280 K, which is less dependent on Ag concentration $x$, and its entropy per 1 mol of guest Ag atoms due to this transition is evaluated to be $S = 9.9 \pm 1.0$ JK$^{-1}$Ag-mol$^{-1}$ from the extra specific heat shown in Fig. 4.12. The obtained value is close to the expected value $R$ln3 (= 9.13 JK$^{-1}$mol$^{-1}$) when the Ag atom is accessible only to three sites $\alpha$, $\beta$, and $\gamma$within a $\sqrt{3}a \times \sqrt{3}a$ unit cell [56].

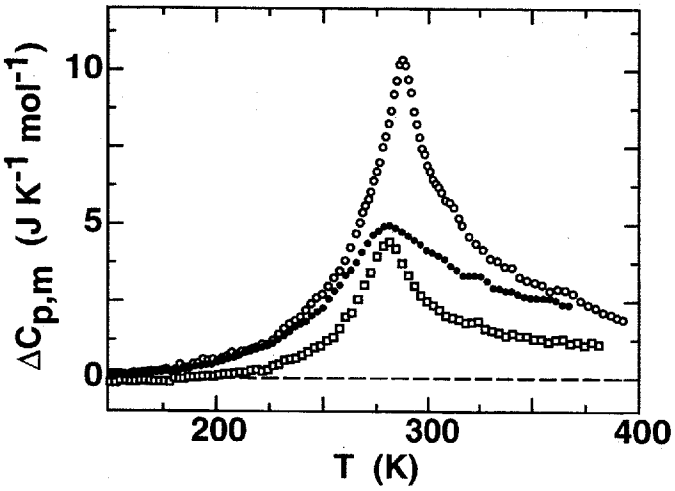


Fig. 4.12 Temperature dependence of the extra specific heat observed for $Ag_xTiS_2$ with $x = 0.0902$ (open square), 0.181(solid circle), and 0.361 (open circle) [57].

Table V Temperature parameters $B_A$ for $A$ atoms (= Ti, S, and Ag) in the $a$-axis and along the $c$-axis for $TiS_2$ and $Ag_xTiS_2$ with $x = 0.18$ at room temperature [51,57]. The mean square thermal displacement, $\mu_{th,A}$, is evaluated using $B_A = 8\pi^2\mu_{th,A}{}^2$.

| | direction | $B_{Ti}$ (Å$^2$) | $B_S$ (Å$^2$) | $B_{Ag}$ (Å$^2$) | $\mu_{th,Ti}$ (Å) | $\mu_{th,S}$ (Å) | $\mu_{th,Ag}$ (Å) |
|---|---|---|---|---|---|---|---|
| $TiS_2$ | $a$ | 0.76 | 1.00 | – | 0.098 | 0.113 | – |
| | $c$ | 1.78 | 1.6 | – | 0.150 | 0.14 | – |
| $Ag_xTiS_2$ | $a$ | 1.18 | 1.08 | 3.0 | 0.122 | 0.117 | 0.195 |
| | $c$ | 1.9 | 1.6 | 1.6 | 0.16 | 0.14 | 0.14 |

## §4.3 Comparison between $Fe_xTiS_2$ and $Ag_{0.15}TiS_2$

Finally, we shall compare the results for $Fe_xTiS_2$ and $Ag_{0.15}TiS_2$. The intercalation compound $Fe_xTiS_2$ shows stage-1 structure over whole Fe concentrations $x = 0$-1, but $Ag_xTiS_2$ shows stage-2 structure in the restricted Ag concentration range $0.1 \leq x \leq 0.3$. The interaction strengths $V_k$ ($k$ = a1, a2, c1, and 2c) for $Ag_{0.15}TiS_2$ are much smaller than those for stage-1 $Fe_{0.15}TiS_2$ and $Fe_{0.333}TiS_2$, and $V_{c2}$ is necessary to obtain the stage-2 structure in $Ag_{0.15}TiS_2$, as described in Chapter 3. Such differences are attributable to the differences in the bond strengths between the guest atoms and host atoms; the bondings between the Ag-S atoms and Ag-Ti ones seem to be much weaker than the strong bondings between the Fe-S and Fe-Ti atoms through the hybridization of the Fe 3d, S 3p and Ti 3d orbitals [38-42].

Furthermore, it is instructive to recall that stage-1 structure appears for other $G_xTiS_2$ with the guests of Li and transition-metal atom $M$ (= Ti, V, Cr, Mn, Co and Ni), while the stage-2 does

Table VI The valence, spin state, and crystal radius for guest atom $G$ with the coordination number $CN = 6$ at the octahedral site in $G_xTiS_2$, as well as the stage number $n$ for $G_xTiS_2$ with $x = 0.15$.

| Guest | valence | spin state | radius (Å) | stage-$n$ |
|---|---|---|---|---|
| Co | 2+ | low spin | 0.79 | 1 |
| Fe | 2+ | high spin | 0.92 | 1 |
| Ag | + | — | 1.29 | 2 |
| Li | + | — | 0.90 | 1 |
| Na | + | — | 1.16 | 2 |
| K | + | — | 1.52 | 2 |

for Na, and K guests with rather large ionic radius. In Table VI are listed the crystal radius of the guest atom with coordination number of 6, together with their valence, spin-state, and stage number for $G$ = Co, Fe, Ag, and alkaline metal Li, Na and K; here we employ the crystal radius $r_c$ reported by R.D. Shannon [68], which can be converted into effective ionic radius $r_i$, by $r_i = r_c$ - 0.14 Å. From Table VI, it is clear that the small size of guest atom with $r_c$ less than 1.00 Å (0.79 Å for $Co^{2+}$, 0.92 Å for $Fe^{2+}$, 0.90 Å for $Li^+$) produces the stage-1 structure, while large size of guest atom with $r_c$ larger than 1.0 Å (1.29 Å for $Ag^+$, 1.16 Å for $Na^+$, 1.52 Å for $K^+$) produces the stage-2 compounds. These results indicates that the local lattice deformation around the guest atoms caused upon intercalation plays a key role to determine the pair-interaction strengths in the stage-2 or stage-1 structure.

Schematic model for local lattice deformation upon guest atoms and its effect to the neighboring guest sites is depicted in Fig. 4.13, where (100) plane cross-sections are illustrated. For small guest atom with $r_c < 1.0$ Å, an induced deformation is rather small and it affects on 1st NNs both in the plane and along the $c$-axis as repulsive interactions $V_{a1}$ and $V_{c1}$, while it gives no direct effect on 2nd NN sites in the plane separated by $\sqrt{3}a$. On the other hand, for large guest atom with $r_c > 1.0$ Å, the van der Waals gap is remarkably expanded, and lattice deformation becomes larger, and it affects on the c2 sites between the 2nd NNs in the next layers as some repulsive interaction $V_{c2}$, as well as repulsive interactions $V_{a1}$ and $V_{c1}$, since the superposition of the deformations at c2 sites become too large to neglect. Thus, the size of the guest atom determines whether the pair-interaction $V_{c2}$ may be neglected or not. However, it is difficult to explain the origin of $V_{a2}$ and $V_{2c}$ between 2nd NN sites in the $a$-axis plane and those in the next nearest neighboring layers, because they may be determined as the result of the superposition of the various interactions, such as bond strengths between the guest and host atoms (Ti-S, $G$-S, and $G$-Ti bonds), van der Waals force, and local lattice deformation, each of which is strongly dependent on the valence and electronic configuration of the intercalated guest atom, as well as it's concentration $x$.

For further understanding of the origin of the repulsive or attractive pair-interactions and their magnitudes, more theoretical and experimental studies will be needed, such as bond orders based on the electronic structures [40], precise X-ray diffraction and X-ray absorption using

synchrotron radiation source, and scanning tunneling microscopy, as done for $Fe_xTiS_2$ [69] and the surface atomic arrangements of the $\sqrt{3}a \times \sqrt{3}a$ structure in Ag/Si(111) [70,71], where the displacements of surface Ag atoms and the Si atoms in the top layer of the substrate are essential.

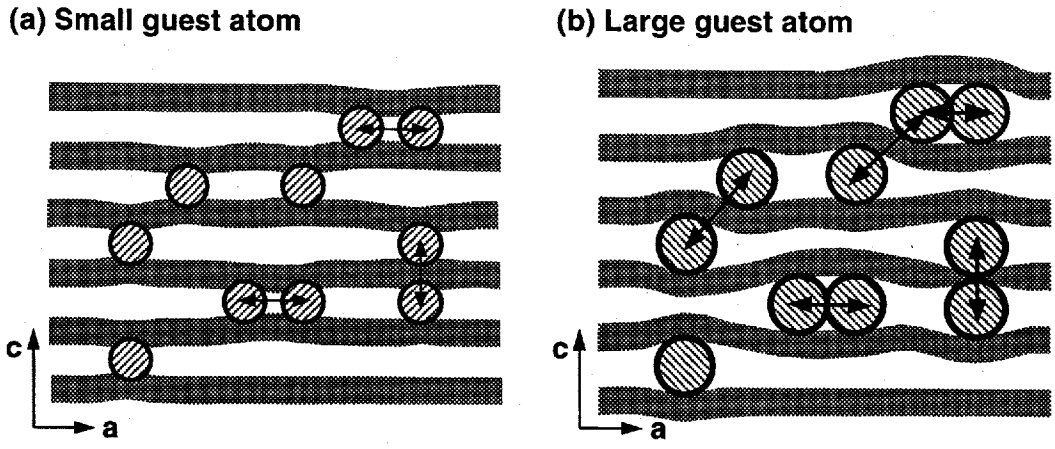


Fig. 4.13 Schematic model for local lattice deformation in $G_xTiS_2$ upon intercalation. The (100) plane cross-sections for (a) small guest atom ($r_c$ < 1.0 Å), and (b) large guest atom ($r_c$ > 1.0 Å). The arrows show repulsive pair-interactions between guest atoms. For the large arom, the van der Waals gap is remarkably expanded, and lattice deformation becomes larger, and it affects on the c2 sites between the 2nd NNs in the next layers.

# Chapter 5

# Conclusion

Monte Carlo simulations of atomic distribution of guest atoms $G$ in intercalation compound $G_xTiS_2$ have been carried out in the triangular lattices in the $a$-axis plane stacked with 6 layers along the $c$-axis (lattice size: $18 \times 18 \times 6$), by taking into account attractive or repulsive pair-interactions between the neighboring guest atoms in the $a$-axis plane $V_{a1}$ and $V_{a2}$, and those along the $c$-axis, $V_{c1}$, $V_{2c}$, and $V_{c2}$. From these calculations, we have made clear the followings.

(1) The atomic distribution of the guest atoms in the $a$-axis planes is primarily determined by the pair-interactions between the 1st NNs $V_{a1}$ and the 2nd NN pair-interaction $V_{a2}$ as well. The pair-interaction $V_{c1}$ between the nearest layers separated by $c$ along the $c$-axis governs the atomic distribution along this direction, and in particular, the attractive interaction $V_{2c}$ between the next nearest layers separated by $2c$ can account for the observed $2c$-periodicity in the superlattices $2\sqrt{3}a \times 2a \times 2c$ for $Fe_xTiS_2$ ($x$ = 1/4) and $\sqrt{3}a \times \sqrt{3}a \times 2c$ for $Fe_xTiS_2$ ($x$ = 1/3) and stage-2 structure of $Ag_{0.15}TiS_2$.

(2) The X-ray diffraction patterns for $Fe_xTiS_2$ are calculated from the atomic distributions obtained using four kinds of pair-interactions, in qualitative agreement with the experimental data of the $2a \times 2a \times 2c$ short-range ordered structure for $x = 0.15$, and superlattices of $2\sqrt{3}a \times 2a \times 2c$ for $x = 0.25$ and $\sqrt{3}a \times \sqrt{3}a \times 2c$ for $x = 0.333$ with fractional site occupancy.

(3) A set of averaged numbers of the neighboring guest atoms, $z_k$ ($k$ = a1, a2, a3, c1, and 2c), specify a given atomic distribution. The comparison of the averaged numbers for the calculated distributions with those for the superlattices with the fractional occupancies in $Fe_xTiS_2$ confirms that the latter is not enough to reproduce the details of the atomic distributions, because we have used the averaged fractional values.

(4) Based on the calculated Fe atomic distributions in $Fe_xTiS_2$, we have discussed on the formation of various types of clusters and the percolation cluster. We have found that one- and two-dimensional percolation clusters are formed by the 3rd NNs in the $a$-axis plane for $x = 0.15$ and 0.25, respectively, and a two-dimensional one is formed by the 2nd NNs for $x = 0.333$, which corresponds to the magnetic phase diagram [spin-glass ($x = 0.15$) and cluster-glass ($x = 0.25$ and 0.333)]. The difference in the type of 2D-percolation cluster is responsible for the difference in the dynamical relaxation behaviors in the thermoremanent magnetization.

(5) Furthermore, using the probability of the number of the Fe atoms near the host S atoms, $p(n)$, evaluated from the Fe atom distributions obtained by the Monte Carlo simulation, as well as EXAFS data, we have calculated the interatomic distance $R$(Ti-S) for $M_xTiS_2$. In the case of $Fe_xTiS_2$ the change in the S atom position along the $c$-axis is almost linear to the number of the nearest Fe atoms $n$, whereas for $Co_xTiS_2$ it is nonlinear. The atomic distributions of the guest atoms around their host S atoms affect the local structures.

(6) Taking account of the repulsive pair-interaction strength $V_{c2}$, in addition to four kinds of pair-interactions $V_{a1}$, $V_{a2}$, $V_{c1}$, and $V_{2c}$, used for $M_xTiS_2$ atomic distributions in stage-2 $G_xTiS_2$

with the in-plane $\sqrt{3}a \times \sqrt{3}a$ structure are obtained. The domain size of the stage-2 structure depends on the strength $V_{c2}$. From the temperature dependence of the atomic distributions, the phase transition from the $\sqrt{3}a \times \sqrt{3}a$ to random arrangement is confirmed.

(7) The X-ray diffraction patterns of $Ag_{0.15}TiS_2$ with stage-2 structure are calculated from the obtained distributions, in good agreement with the experimental data of diffuse rod elongated along the $c^*$-axis. The in-plane order-disorder phase transition of the Ag atoms are discussed based on the calculated distributions, together with experimental results of the thermal displacements of Ti, S, and Ag atoms and entropy change due to the phase transition.

(8) Difference between $Fe_xTiS_2$ and $Ag_{0.15}TiS_2$ is discussed from the viewpoint of local lattice deformation caused upon intercalation of guest atoms. The size of the guest atom plays a crucial role to form stage-2 intercalation compound. Stage-2 compound is formed only for large guest atom with crystal radius of $r_c > 1.0$ Å, due to a large lattice deformation, which affects on the 2nd NN sites in the next layers to exert some repulsive interaction $V_{c2}$.

Thus, Monte Carlo simulation method with the pair-interactions is powerful and useful to get atomic distribution of guest atoms in $G_xTiS_2$, as shown in this work. This work will be extended further to the pressure-induced stage transition in $Ag_{0.35}TiS_2$ from stage-2 at ambient pressure to stage-1 at high pressure [72], and to $G_xTiS_2$ with higher guest concentration $x \geq 0.40$, where the effect of the interaction between the 1st NNs could be dominant and some complicated patterns could be appeared.

# Acknowledgements

The author would like to express her sincere thanks to Prof. Masafumi Sera for his interest and encouragement through this work. Furthermore, she would like to express her sincere gratitude to Emeritus Prof. Masasi Inoue for his patient guidance, constant encouragement and interest, and Prof. M. Sasaki for his valuable discussion, useful suggestions and kind advice. She is deeply grateful to Dr. H. Negishi for his beneficial discussions and continuous support. She appreciate Prof. Y. Kuroiwa at Okayama University for giving her research group the detailed experimental data of the neutron and X-ray diffractions on $Fe_xTiS_2$ and $Ag_xTiS_2$, and valuable discussion.

She would like to thank Emeritus Prof. H. Fujiwara, Prof. M. Nomura at Ube National College of Technology, the late Prof. H. Kadomatsu, and Dr. K. Umeo, who helped her to continue her research works with their encouragements. Sincere thanks are due to Prof. S. Keitoku and Dr. K. Nishioka at Hiroshima Women's University for their collaboration, who taught infinite possibility to research under restricted conditions to the author. She is grateful to Ms. R. Tsukamoto, Ms. J. Nakagawa, Ms. J. Koyama, Ms. Y. Nishigaki, Ms. Y. Okuda, and Ms. S. Tokumitsu for their supports on office routine and heartful encouragements. She also acknowledges Drs. S. Ohara, K. Takase, Y. Hara, Mrs. A. Yamasaki, H. Yamada, S. Kakita, and all members of Inoue Laboratory for their collaborations, exciting discussions and friendly help.

Finally, I acknowledge my parents, children, and all persons who have helped me from the outside of this work for their understanding on my work and heartful supports.

# References


1) F. Levy: *Intercalated Layered Materials*, (D. Reidel, Dortrecht, 1979).
2) M.S. Whittingham and A.J. Jacobson: *Intercalation Chemistry*, (Academic Press, New York, 1982).
3) M.S. Dresselhouse, G.D. Dresselhouse, J.E. Fisher, and M.J. Moran: *Intercalated Graphite*, (North-Holland, New York, 1983).
4) M.S. Whittingham: Prog. Solid State Chem. **12** (1978) 41.
5) W. Muller-Warmuth and R. Schöllhorn: *Progress in Intercalation Reserch*, (Kluwer Academic Publ., Dortrecht, 1994).
6) M. Inoue, H.P. Hughes, and A.D. Yoffe: Adv. Phys. **38** (1989) 565.
7) M. Inoue and H. Negishi: *Magnetic and Transport Properties of Transition-Metal Intercalation Compounds* in *Recent Advances in Magnetism of Transition Metal Compounds*, eds. A. Kotani and N. Suzuki, (World Scientific, Singapore, 1993), p. 193.
8) M. Inoue and H. Negishi: J. Phys. Chem. **90** (1986) 235.
9) H. Negishi, S. Ôhara, and M. Inoue: Phys. Stat. Sol. (b) **151** (1989) 441.
10) T. Kusawake, Y. Takahashi, and K. Ohshima: Mat. Res. Bull. **33** (1998) 1009.
11) H. Negishi, S. Ôhara, Y. Takata, T. Yokoyama, M. Taniguchi, and M. Inoue: Mater. Sci. Forum **91-93** (1992) 603.
12) H. Negishi, S. Negishi, M. Sasaki, M. Inoue, and S. Ôhara: Mol. Cryst. Liq. Cryst. **341** (2000) 63.
13) M. Inoue, Y. Muneta, H. Negishi, and M. Sasaki: J. Low Temp. Phys. **63** (1986) 235.
14) K. Takase, H. Negishi, M. Sasaki, and M. Inoue: J. Low Temp. Phys. **103** (1996) 107.
15) Y. Ueda, H. Negishi, M. Koyano, M. Inoue, K. Soda, H. Sakamoto, and S. Suga: Solid State Commun. **57** (1986) 839.
16) Y. Ueda, K. Fukushima, H. Negishi, M. Inoue, M. Taniguchi, and S. Suga: J. Phys. Soc. Jpn. **56** (1987) 2471.
17) A. Fujimori, S. Suga, H. Negishi, and M. Inoue: Phys. Rev. B **38** (1988) 3676.
18) H. Namatame, S. Nohara, H. Negishi, M. Inoue, and S. Suga: Surf. Sci. **242** (1991) 294.
19) A. Kimura, S. Suga, T. Matsushita, S. Imada, N. Shino, Y. Saitoh, H. Shigeoka, H. Daimon, T. Kinoshita, A. Kakizaki, S.-J. Oh, H. Negishi, and M. Inoue: Jpn. J. Appl. Phys. **32** (1993) 255.
20) T. Matsushita, S. Suga, Y. Tanaka, H. Shigeoka, T. Nakatani, T. Okuda, T. Terauchi, T. Shishidou, A. Kimura, H. Daimon, S.-J. Oh, A. Kakizaki, T. Kinoshita, H. Negishi, and M. Inoue: J. Electron Spectrosc. and Relat. Phenom. **78** (1996) 477.
21) A Kimura, S. Suga, T. Matsushita, S. Imada, H. Negishi, and M. Inoue: Physica B **237-238**, (1997) 388.
22) T. Matsushita, S. Suga, A. Kimura, H. Negishi, and M. Inoue: Phys. Rev. B **60** (1999) 1678.
23) S. Suga: Mol. Cryst. Liq. Cryst. **341** (2000) 9.

24) M. Koyano, H. Negishi, Y. Ueda, M. Sasaki, and M. Inoue: Phys. Stat. Sol. (b) **138** (1986) 357.
25) M. Inoue, M. Koyano, K. Fukushima, H. Negishi, and M. Sasaki: Phys. Stat. Sol. (b) **139** (1987) 273.
26) M. Koyano, S. Horisaka, H. Negishi, M. Sasaki, M. Inoue, N. Suzuki, and K. Motizuki: J. Low Temp. Phys. **78** (1990) 141.
27) H. Negishi, H. Yamada, K. Yuri, M. Sasaki, and M. Inoue: Phys. Rev. B **56** (1997) 11144.
28) H. Negishi, S. Kakita, H. Yamada, S. Negishi, M. Sasaki, and M. Inoue: Solid State Commun. **112** (1999) 275.
29) M. Inoue and H. Negishi: J. Phys. Soc. Jpn. **54** (1985) 380.
30) M. Inoue, M. Matsumoto, H. Negishi, and H. Sakai: J. Magn. Magn. Mater. **53** (1985) 131.
31) M. Danot, J. Rouxell, and O. Gorochov: Mater. Res. Bull. **9** (1974) 1383.
32) T. Yoshioka and Y. Tazuke: J. Phys. Soc. Jpn. **54** (1985) 2088.
33) H. Negishi, A. Shoube, H. Takahashi, Y. Ueda, M. Sasaki, and M. Inoue: J. Magn. Magn. Mater. **67** (1987) 179.
34) H. Negishi, H. Takahashi, and M. Inoue: J. Magn. Magn. Mater. **68** (1987) 271.
35) H. Negishi, M. Koyano, M. Inoue, T. Sakakibara, and T. Goto: J. Magn. Magn. Mater. **74** (1988) 27.
36) H. Negishi, S. Ohara, M. Koyano, M. Inoue, T. Sakakibara, and T. Goto: J. Phys. Soc. Jpn. **57** (1988) 4083.
37) K. Takase, Y. Kubota, Y. Takano, H. Negishi, M. Sasaki, M. Inoue, and K. Sekizawa: Physica B **284-288** (2000) 1517.
38) T. Yamasaki, N. Suzuki, and K. Motizuki: J. Phys. C **20** (1987) 419.
39) N. Suzuki, T. Yamasaki, and K. Motizuki: J. Magn. Magn. Mater. **70** (1987) 64.
40) N. Suzuki, T. Yamasaki, and K. Motizuki: J. Phys. C **21** (1988) 6133; T. Yamasaki: Dr Thesis (Osaka Univ., 1989).
41) N. Suzuki, T. Yamasaki, and K. Motizuki: J. Phys. Soc. Jpn. **58** (1989) 3280.
42) T. Teshima, N. Suzuki, and K. Motizuki: J. Phys. Soc. Jpn. **60** (1991) 1005.
43) Y. Hara, H. Negishi, M. Sasaki, and M. Inoue: J. Magn. Magn. Mater. **159** (1996) 125.
44) H. Negishi, Y. Hara, M. Sasaki, and M. Inoue: J. Phys. Chem. Solids **57** (1996) 1097.
45) Y. Hara, A. Yamasaki, H. Negishi, M. Sasaki, and M. Inoue: J. Magn. Magn. Mater. **168** (1997) 213.
46) H. Negishi, A. Yamasaki, M. Sasaki, M. Inoue, and H. Kadomatsu: J. Magn. Magn. Mater. **185** (1998) 85.
47) Y. Kuroiwa, M. Nishimura, R. Nakajima, H. Abe, and Y. Noda: J. Phys. Soc. Jpn. **63** (1994) 4278.
48) Y. Kuroiwa, M. Nishimura, Y. Noda, and Y. Morii: Physica B **213-214** (1995) 396; Y. Kuroiwa: Private communication for $x = 0.15$.
49) Y. Kuroiwa, H. Honda, and Y. Noda: Mol. Cryst. Liq. Cryst. **341** (2000) 15.
50) G.A. Scholz and R.F. Frindt: Mater. Res. Bull. **15** (1980) 1703.

51) M. Mori, K. Oshima, S.C. Moss, R.F. Frindt, M. Plischke, and J.C. Irwin: Solid State Commun. **43** (1982) 781.
52) R.M. Suter, M.W. Shafer, and P.M. Horn: Phys. Rev. B **26** (1982) 1495.
53) K. Oshima and S.C. Moss: Acta Cryst. A **39** (1983) 298.
54) K.K. Bardhan, G. Kirczenow, G. Jackle, and J.C. Irwin: Phys. Rev. B **33** (1985) 4149.
55) Y. Kuroiwa and K. Ohshima: Phys. Rev. B **42** (1990) 11591.
56) H. Fujimori, M. Oguni, K. Kitayama, T. Uchida, and M. Wakihara: J. Phys.: Condens. Matter **5** (1993) 6673.
57) H. Fujimori and M. Oguni: Phys. Rev. B **50** (1994) 18586.
58) Y. Kuroiwa, T. Tamura, and K. Ohshima: J. Appl. Cryst. **31** (1998) 91.
59) S.A. Safran: Solid State Physics **42** (1987) 183.
60) G. Kirczenow: Phys. Rev. Lett. **55** (1985) 2810.
61) R. Brec, P. Deniard, and J. Rouxel: *Chalcogenides: Electronic Properties* in *Progress in Intercalation Reserch*, eds. W. Muller-Warmuth and R. Schöllhorn, (Kluwer Academic Publ., Dortrecht, 1994), pp. 177-221.
62) N. Metropolis, A.W. Rosenbluth, M.N. Rosenbluth, A.H. Teller, and E. Teller: J. Chem. Phys. **21** (1953) 1087.
63) D.W. Heermann: *Computer Simulation Methods in Theoretical Physics*, 2nd ed., (Springer, Berlin, 1990).
64) W. Schweika: *Disordered Alloys -Diffuse Scattering and Monte Carlo Simulations-* (Springer, Berlin, 1998).
65) C.P. Robert and G. Casella: *Monte Carlo Statistical Methods* (Springer, New York, 1999).
66) A.P. Legrand and S. Flandrois: *Chemical Physics of Intercalation*, (Plenum, New York, 1987).
67) R. Zallen: *The Physics of Amorphous Solids*, (John Wiley, New York, 1983) Chapter 4.
68) R.D. Shannon: Acta Cryst. A**32** (1976) 751.
69) Z. Dai, Q. Xue, C.G. Slough, and R.V. Coleman: Phys. Rev. B**48** (1993) 14543.
70) H. Aizawa, M. Tsukada, N. Sato, and S. Hasegawa: Surface Science **429** (1999) L509.
71) H. Kamigaki: private communication.
72) O. Zhou, J.E. Fisher, and K.S. Liang: Phys. Rev. B**44** (1991) 7243.